Slope exchange processes in the Weddell and Amundsen Seas

A thesis submitted to the School of Environmental Sciences
of the University of East Anglia in partial fulfilment
of the requirements for the degree of Doctor of Philosophy

Marina do Valle Chagas Azaneu

January 2019

Supervisors
Karen J. Heywood
Bastien Y. Queste
Benjamin G. M. Webber
Andrew F. Thompson

Abstract

This thesis aims to investigate the dynamical processes of the along-slope currents in the Weddell and Amundsen Seas (Antarctica), their variability and the mechanisms that regulate the cross-slope exchange of properties.

Firstly, this thesis explores the short-term and spatial variability of the Antarctic Slope Front system at the northwestern Weddell Sea using data from three ocean gliders. Twenty-two sections along the eastern Antarctic Peninsula are grouped regionally and composited by isobaths. The along-slope transport of the Antarctic Slope Current (upper 1000 m) varies between 0.2 and 5.9 Sv. Higher eddy kinetic energy (0.003 $m^2 s^{-2}$) is observed on sections where dense water is present, possibly due to baroclinic instabilities in the deep layer. These results provide some of the first observational confirmation of the high frequency variability associated with an active eddy field that has been suggested by recent numerical simulations in this region.

Using a multidisciplinary dataset, the physical processes associated with phytoplankton biomass distribution and how these relate to frontal processes east of the Antarctic Peninsula are assessed. There is a distinction between upper-slope and off-shelf areas, which are likely disassociated from each other. Over the shelf, the relatively low stratification and the likely enhanced mixing and nutrient input from sediments would contribute to the relatively high primary production. Offshore, the stronger pycnocline and passive sinking of phytoplankton creates a deeper subsurface chlorophyll maximum.

Finally, observations from moorings and from ship-based hydrographic stations at eastern Amundsen Sea are analysed to investigate the variability of the slope undercurrent and the Circumpolar Deep Water layer within troughs at the continental shelf. The cumulative onshore temperature transport of CDW was 1.21 TW and 1.79 TW at the central and eastern trough, respectively. High-frequency variability of temperature transport estimates are different among shelf-break moorings; eddies and coastal-trapped waves are likely contributors.

ACKNOWLEDGEMENTS

These four years of PhD, despite the feeling of it passing by so quickly, represented an intense journey. Much was learned scientifically and emotionally, and I aim to keep these years vivid in my memory. There are many people that I came across during this journey that contributed to this learning process, and I will always have a hug to offer for those. There are, however, some people I would like to mention.

Firstly, I would like to sincerely thank Karen for having me as a student and for all her patience and guidance. I'm thankfull to have you as an inspiration and as a mentor; thank you for all the support you have provided me. I want to thank my other supervisors Bastien, Andy and Ben for being so lovely, for their time, patience and numerous draft-readings. Bastien also needs to be thanked for glider toolbox discussions, for chats during crisis moments and for the 27 Roxanne shots. Thanks to Gareth, Marcos, Rob and Gillian for sharing their glider knowledge and the fun moments of salsa dancing and swimming. I am also grateful to Adrian for allowing me to join the Bobble cruise - I learned a lot, met incredible people and, of course, had lots of fun (thanks for that Alej and Pumpkin!).

I am very lucky for meeting so many amazing people during these 4 years. Umberto, Richard, Tahmeena, Louise and Karin, thank you for being here even when you were not here anymore. Thanks to Chata, Pierre, Cris, Andre, Marta, Montsa and Jaume for their company, laughs and barbecues. Office 3.16, it was a pleasure to share the office with all of you. I'm quite sure you probably won't say the same, though - I'm sorry (not sorry) for the loud and overly emotional latin touch. Peter, Denis, Elise, Helen, Stuart and Michael, thanks for the "lively" conversations, for the (hilarious) saxophone lessons, for the memorable Flaunt nights, for accepting the mud challenge, and for pretending to follow the fitness dream with me. Michael and David, thank you for all the amusing conversations (or should I say monologues?) and for ruining permanently my accent. I also need to thank Gabi and Abel, who contributed to this journey in many different ways.

Finally, I would never have had the courage to be here without the support of my family. Father, mother, brothers, grandpas, aunt, in laws, your love from 9280 km away kept me going. Eu amo vocês. I also need to sincerely thank Adriano, who chose to go on this journey with me (and with our love Gurizinho). Your love, company, patience and kindness were essential for me to get this far.

Financially, I would like to thank CAPES-Brazil for the support given to this doctorate.

To Zilda do Valle Chagas, *in memoriam*

Contents

List of figures

List of tables

LISTS OF ACRONYMS

ASF Antarctic Slope Front

ASC Antarctic Slope Current

PV Potential vorticity

WF Weddell Front

WDW Warm Deep Water

WSDW Weddell Sea Deep Water

WSBW Weddell Sea Bottom Water

DAC dive-averaged current

AABW Antarctic Bottom Water

EKE Eddy kinetic energy

AASW Antarctic Surface Water

CDW Circumpolar Deep Water

WW Winter Water

mCDW Modified CDW

TTF total temperature transport

MTF mean temperature flux

ETF eddy temperature flux

PIG Pine Island Glacier

POC particulate organic carbon

1

INTRODUCTION

1.1 BACKGROUND AND MOTIVATION

Over the period of 1901 to 2010, global mean sea level rose by 0.19 (0.17–0.21 m), for which ocean thermal expansion and glacier melting have been the dominant contributors (Church et al., 2013). The rate of sea level rise since the mid-20th century (2.0 [1.7–2.3] mm yr^{-1} during 1971–2010) has been larger than the mean rate during the previous two millennia. It will continue to rise during the 21st century, very likely at a faster rate than observed from 1971 to 2010, under all IPCC scenarios (Church et al., 2013). For an unmitigated future rise in emissions of greenhouse gases (RCP8.5), it is estimated 0.45 to 0.82 m of global mean sea level rise by the end of this century. By then, about 70% of the coastlines worldwide are projected to experience a sea level change within ±20% of the global mean. The Antarctic ice sheet holds the majority of the Earth's fresh water and has the potential to raise global sea level by 58 m if rapidly discharged (Fretwell et al., 2013).

The average rate of the Antarctica contribution to sea level rise likely increased from 0.08 [-0.10 to 0.27] mm yr^{-1} for 1992–2001 to 0.40 [0.20 to 0.61] mm yr^{-1} for 2002–2011. Reductions in the thickness and extent of floating ice shelves have affected grounded ice, triggering retreat and acceleration of marine-terminating glaciers (Shepherd et al., 2018). While the Antarctic sea ice extent has shown modest decadal trends, the grounded ice sheet mass loss is estimated at 2720 ± 1390 Gt between 1992 and 2007 (Wingham et al., 2018) and its peripheral ice shelves are thinning in many Southern Ocean sectors. These changes do not occur uniformly around Antarctica (Fig. 1.1a). For example, increase in losses in the Amundsen Sector due to speed up of glacier flow has been reported (Sutterley et al., 2014). The retreat or thinning of the ice shelves is generally associated with the destabilisation of the grounded ice since the ice shelves provide mechanical support for the grounded ice sheet upstream (Shepherd et al., 2018). The volume of the Antarctic ice shelves has declined through net overall thinning (Paolo et al., 2015) and through progressive calving-front retreat of those at the Antarctic Peninsula. However, the highest ice shelf thinning rates have occurred in the Amundsen and Bellingshausen Seas in west Antarctica (Shepherd et al., 2004). Although the main retreat events at the Antarctic Peninsula have been attributed to surface melting and atmospheric warming (Rignot et al., 2004), in the Amundsen and Bellingshausen seas changes are associated with ocean-driven basal melting and the intrusion of the warm CDW into the cavities beneath the ice shelves (Thoma et al., 2008; Pritchard et al., 2012). The distinct behaviour between these two regions is a consequence of atmospheric forcing, ocean circulation and geological differences. Even though many processes responsible for regulating the amount of heat that reach the shelves have been identified, the relative importance of these processes needs to determined. This thesis explores two distinct datasets, at the northwestern Weddell Sea and at the eastern Amundsen Sea, to evaluate the shelf-break processes that modulate the transport of warm waters onto the shelf and their variability (Fig. 1.2).

The impact of the intrusion on ice sheet stability is not uniform around Antarctica, the West Antarctic ice shelves being more susceptible to it. These differences are due to, among other factors such as the grounding line and bedrock geometry, different degrees of CDW modification on its path onto the continental shelf (Fig. 1.1b). CDW is the warmest water mass in the Southern Ocean, being transported eastward around the continent in the Antarctic Circumpolar Current (ACC; Fig. 1.3a). In the Weddell Sea, the CDW is cooled within the clockwise gyre that separates the continental margin from the warm ACC waters (Fig. 1.1b). In this region, the Ekman transport driven by the easterly winds transports the Antarctic Surface Water (AASW; formed by cooling and freshening of upwelled CDW by atmospheric and ice interaction)

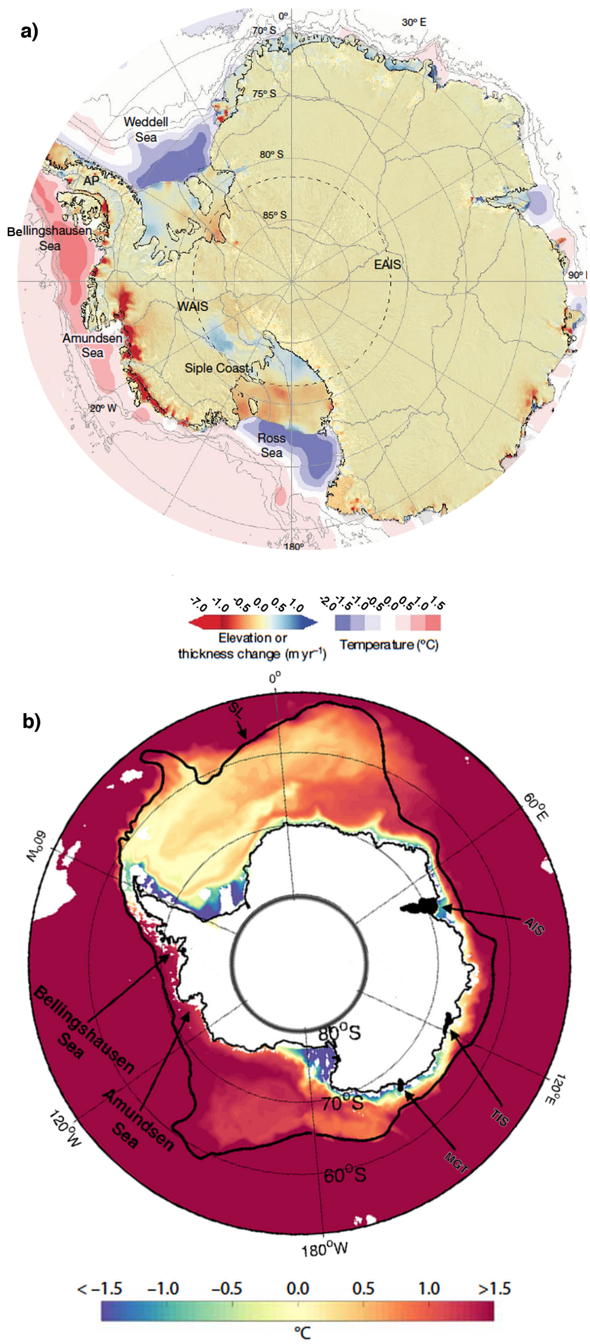

Figure 1.1: a) Average trend in the elevation and thickness of Antarctic grounded ice and ice shelves, respectively, determined between 1992 and 2017 north of 81.5 °S (dashed grey circle), and between 2010 and 2017 elsewhere. Also shown is the ocean temperature at the sea floor around the continent. Figure modified from (Shepherd et al., 2018). b) Average 2005-2010 ocean temperature at 438 m depth, nominal depth of the Circumpolar Deep Water core in the Antarctic Circumpolar Current, from the Southern Ocean State Estimate Mazloff et al. (2010). The heavy black line marks the southern boundary of the Antarctic Circumpolar Current. Figure modified from Silvano et al. (2016).

onto the continental shelf and generates coastal downwelling. The strong subsurface horizontal gradient between the fresher and colder on-shelf AASW and the warmer and saltier off-shelf CDW characterises the Antarctic Slope Front (ASF; Jacobs, 1991; Heywood et al., 2004), which restricts the on-shelf intrusion of the CDW even in areas where the Shelf Water (SW; when AASW salinity is enhanced by brine rejection during sea ice production) is absent. Associated with the ASF, the zonal circulation in the shelf-break area is dominated by the westward Antarctic Slope Current (ASC; Fig. 1.3a). In West Antarctica, the southern limit of the ACC current is closer to the coast; at the western Antarctic Peninsula for example, the AAC reaches the shelf break and allows warm and relatively salty CDW to reach the continental shelf (Fig. 1.1b). In West Antarctica, the coastal downwelling is too weak to deepen the layer of AASW to the seabed and the surface buoyancy forcing is generally too weak to produce SW (when AASW salinity is enhanced by brine rejection during sea ice production) (Jenkins et al., 2016). Further to the west, in the Amundsen Sea, the easterly winds over the shelf become progressively more important, and there is the development of a relatively weak ASF and the westward current associated with it (ASC; Walker et al., 2013). The weak stratification in the Antarctic region and the strong easterly winds do not allow the adjustment that limits the depth of the wind-driven circulation in lower latitudes; as a consequence, the current extends to great depth and the flow is strongly influenced by topography. Thus, the slope area is a key region for understanding the processes that influence the heat transport toward ice shelves. The characteristics of the ASF, and therefore its capacity to modulate the cross-slope exchange vary among regions. The study of the continental slope processes in these two different regions will possibly contribute to the understanding the relative importance of processes affecting the onshore heat transport.

The production of dense shelf waters is another process that contributes to the importance of the Antarctic region to global climate. The localised production of the dense waters around the Antarctic continental shelf and the export of the Antarctic Bottom Water (AABW) to the world ocean are important contributors to the variability of the global overturning circulation deep cell (Talley, 2013), which transports mass, heat, salt, carbon and nutrients, and thus plays an important role in regulating global climate (Rahmstorf, 2003; Lumpkin and Speer, 2007). The Weddell Sea is one of the main contributors to the global AABW export (Rintoul, 1998; Orsi et al., 1999).

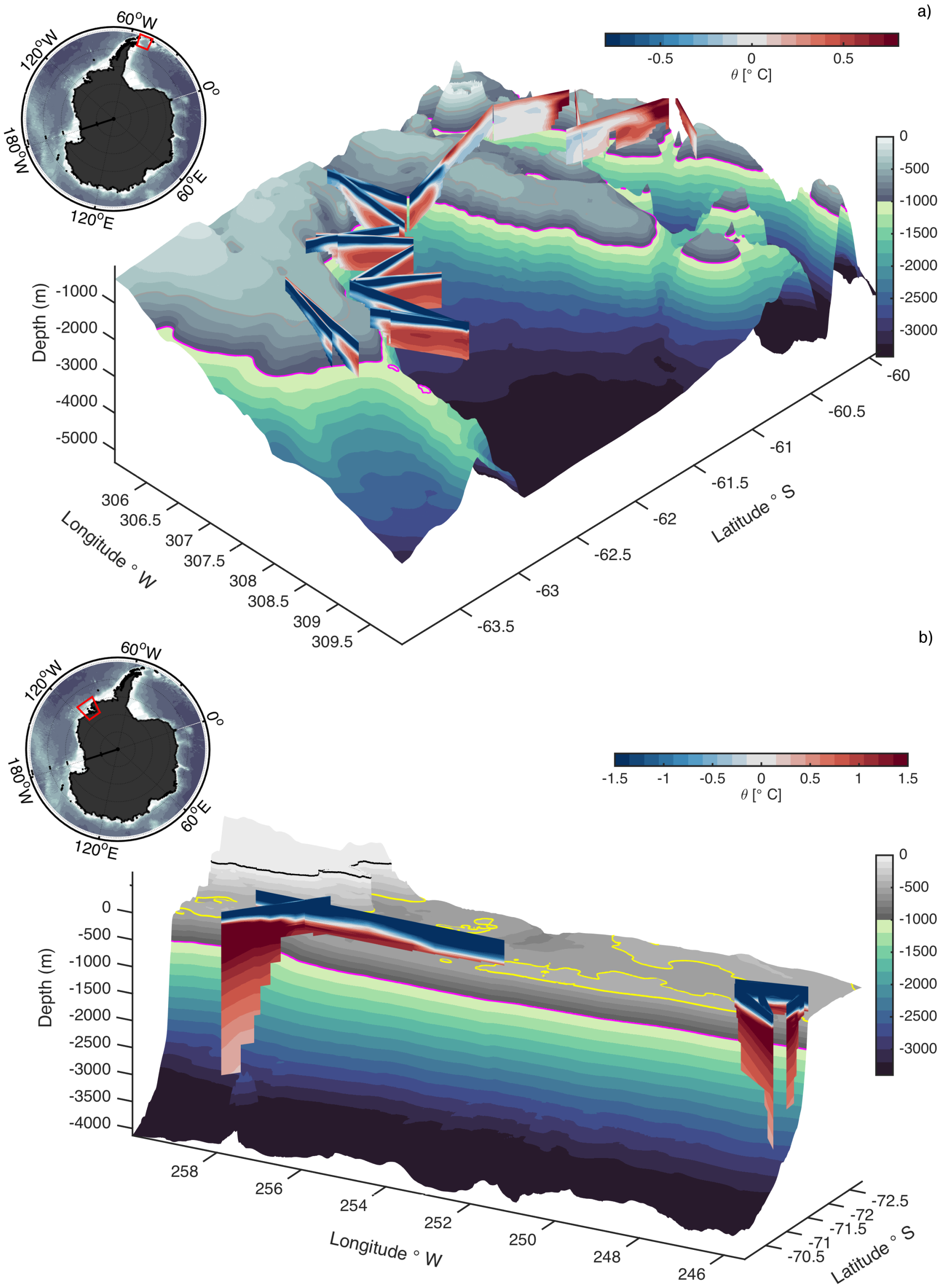

Figure 1.2: Map of the (a) northwestern Weddell Sea and (b) eastern Amundsen Sea study areas. Sections are interpolated from (a) glider and (b) CTD data and show the potential temperature (θ°C) measured by these instruments. Black, yellow and pink lines indicate the 0, 500 and 1000 m isobaths. Inserted panels show the Antarctic map and the location of the study regions. Bathymetric data (m) is from Gebco global 30 arc-second interval grid and is coloured in gray and green.

The formation of dense shelf waters involves modification of shelf waters by sea ice and atmospheric interaction and further mixing with regional CDW as it flows down the slope (forming AABW). Because the formation and export of these dense water masses require the interaction between onshore and offshore waters, the ASF can modulate the ventilation of the abyssal ocean by constraining the cross-slope exchange of properties. The regional properties of the AABW are thus influenced by local water mass properties and by coupled physical processes associated with sea ice formation, opening of coastal polynyas (areas of open water in otherwise sea ice-covered regions), basal ice shelf melting and mixing with ambient water masses. Changes in the properties of the source waters, in the atmospheric forcing or in the dynamical processes that lead to the export of waters from the shelf can affect the final properties of AABW. It is likely that the dense flow also has effect on the dynamics of the ASF, however this interaction is still to be investigated.

The shelf-slope processes and the strength of the overturning circulation also have broad implications for biogeochemical cycles and atmospheric carbon dioxide levels. As the dense waters sink and ventilate the ocean interior by carrying oxygen-rich waters, they also contribute to the downward flux of carbon through the sinking of organic matter. This downward flow is balanced by the upwelling limb of the overturning cell, which brings nutrients from the ocean interior to the surface ocean and give support to global marine primary production (Rintoul, 2018). The net exchange of carbon between the atmosphere and the Southern Ocean depends on the outgassing of carbon driven by upwelling of natural carbon-rich deep water, and the uptake and storage of anthropogenic carbon, both of which depend on the strength of the overturning circulation. Despite the nutrient input, the primary productivity in the Southern Ocean is largely limited by the low concentration of iron (Fe) (Martin et al., 1990; de Baar et al., 1995; Holm-Hansen et al., 2004). The most significant source of iron in the Southern Ocean is likely to be from sediments on the continental shelf and shallow plateaus and islands around the continent. The Antarctic continental shelf is not only a source of iron, but also is responsible for the most of the primary productivity in the Southern Ocean (Fig. 1.3b Arrigo et al., 2008b), supporting high biomass of higher trophic levels. It is likely that the fertilisation of the open ocean by the continental shelf may be affected by the cross-slope processes and the dynamics of the ASF; the physical processes at the slope region that may regulate the export of

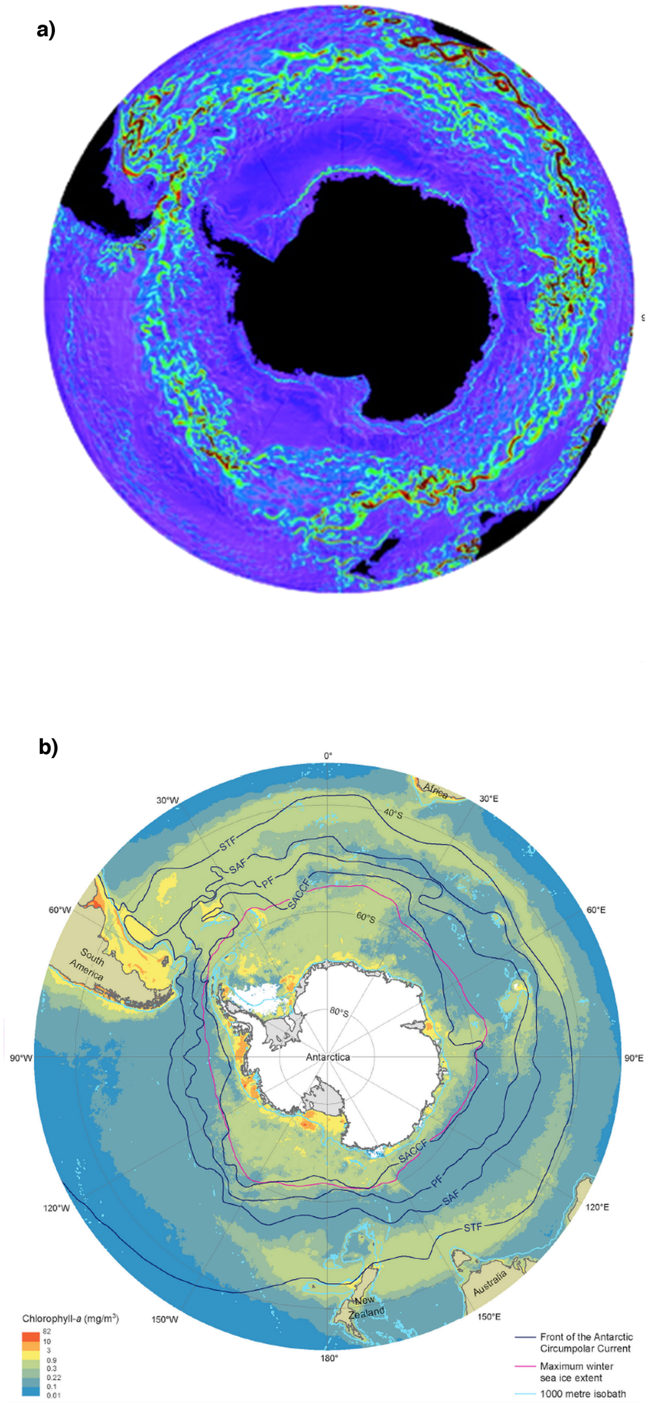

Figure 1.3: a) Surface current speed from the OCCAM1 ocean model (Lee and Coward, 2003), where the ACC jest and the ASC can be observed. Reproduced from (Thompson, 2008); b) Summer near-surface Chlorophyll *a* concentration (austral summer season between 2002/03 and 2015/16), frontal locations (black lines; Orsi et al., 1995) and sea ice extent (1979-2008) in the Southern Ocean (red line). STF, Sub-Tropical Front; SAF, Sub-Antarctic Front; PF Polar Front; SACCF, Southern Antarctic Circumpolar Current Front. Reproduced from Deppeler and Davidson (2017).

the primary production to off-shore regions remain to be investigated.

Recent progress in the dynamical understanding of the Southern Ocean has highlighted the importance of both transient and stationary eddies in many different aspects of its dynamics. They are involved in setting the structure of the ACC and of the overturning circulation, which is closely related to the eddy field associated with the ACC unstable flow (Marshall and Radko, 2003). A strengthening or weakening of the overturning circulation under changes in wind forcing (Thompson et al., 2011) will likely be associated with the sensitivity of this eddy field, which is still under debate (Farneti et al., 2010; Dufour et al., 2012). Elevated eddy kinetic energy in the ACC occurs in "hot spots", generally defined by topography. Eddy vorticity fluxes provide torque that shift jets and affect the strength of the mean flow (Williams et al., 2007). When encountering a major topographic feature, advection and stirring by eddies facilitate the cross-front exchange by deep barotropic eddies (Naveira Garabato, 2012). Eddies are also responsible for stirring of tracers along isopycnals away of the main ACC jets (Ferrari and Nikurashin, 2010). At the shelf break, regional modelling studies show that eddy flux is important for transporting warm waters onto the shelf (Fig. 1.4; Stewart and Thompson, 2015). Theoretical studies also identify coastal-trapped waves (St-Laurent et al., 2013) and the interaction of bounded flow with deep troughs (Assmann et al., 2013) at the continental shelf as factors affecting the on-shore heat transport. The position and strength of the ASF is likely to affect the properties that will be available to get onshore. However, many of these processes, particularly at the shelf break, still require to be quantified and model results to be assessed by in situ data. This is necessary to assess the processes that regulate the ocean heat transport available to reach the sub-ice-shelf cavities and the possible vulnerability of the Antarctic Ice Sheet.

Several changes in the Southern Ocean have been reported, such as the warming of the bottom shelf waters in the Amundsen and Bellingshausen sea (Schmidtko et al., 2014), and the freshening, warming and contraction of the AABW layer in the past decades (Purkey and Johnson, 2013; Azaneu et al., 2013). A reduction in the overturning circulation in the last decade has been suggested as the cause of changes in chloroflurocarbons between 1990s and early 2000s (DeVries et al., 2017). Warming, reduction of salinity, acidification and migration of the ocean fronts are some of the changes that are expected to alter the structure and function of the

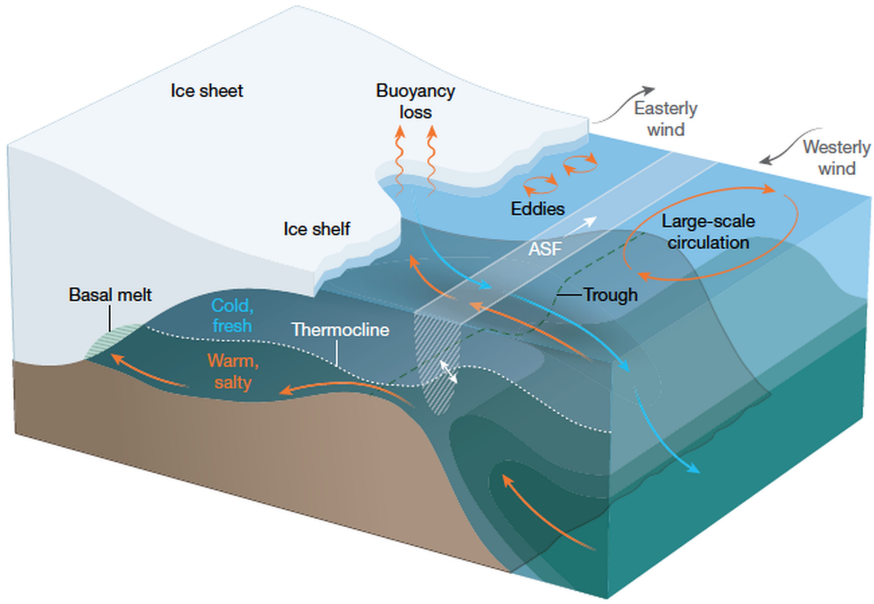

Figure 1.4: The schematic illustrates physical processes that can influence the transport of warm water from the open ocean to the base of the floating ice shelves. Reproduced from Rintoul (2018).

phytoplankton communities in the Southern Ocean which, in turn, will affect carbon export and nutrition for higher trophic levels (Deppeler and Davidson, 2017). Much has been debated on what these recent changes represent in terms of sensitivity of the Southern Ocean to changes in forcing. These discussions, however, remain mainly speculative despite the progress made in recent years in understanding the dynamics and global influence of the Southern Ocean. This happens mostly because the global effects of the Southern Ocean are dictated largely by processes of local and regional scales, of which theoretical understanding is still very limited (Rintoul, 2018). The continental shelf and slope are key regions for understanding these changes as the dynamical processes in these regions not only affect the amount of heat that reaches the ice shelves, but also influence how the signal from changes in the ocean-sea-atmosphere interaction is transmitted to the deep ocean (Fig. 1.4). Despite the importance of the continental shelf and slope regions, they are poorly sampled, particularly during austral winter, and many of the local processes discussed here are poorly constrained. This occurs in part due to extensive ice cover and the remote nature of the region. More importantly, the length scale of oceanographic feature such as eddies, fronts, jets and meanders are particularly small due to the local Rossby radius of deformation. This imposes challenges not only on sampling but also on modelling of these processes. Many climate models and reanalyses, for example, are unable to simulate the formation and export of dense waters from the shelf, producing temperature and/or salinity biases in the modelled ocean abyss (Azaneu et al., 2014; Heywood et al., 2014). As a consequence, many uncertainties remain in the heat transport across the continental slope, as well as ice shelf stability and fresh water input, which compromises quantitative predictions of future changes. Notwithstanding, observational records of longer length and coverage and recent technological advances, such as the dataset used in this study, can contribute to a better understanding of the nature and drivers of variability of the Southern Ocean and progress its physical understanding. This will likely give a better indication of how this region may respond to future changes.

1.2 Questions addressed in this study

This thesis aimed to investigate the dynamical processes associated with the frontal system at the Weddell and Amundsen Sea continental slopes. The thesis has three results chapters, which intend to answer the following questions:

- Is the hydrographic signature of the Antarctic Slope Front and its associated current consistent along the eastern Antarctic Peninsula continental slope?
- What is the relationship, if any, between the dense water overflow and the frontal current?
- Does the slope front contribute to enhancing local primary productivity?
- In the Amundsen Sea, is the slope undercurrent a persistent feature?
- Is the strength of the undercurrent associated with the onshore flow of warm waters, as expected by theoretical studies?
- What other processes can affect the variability of onshore heat transport?

1.3 Thesis outline

In chapter 2 (published as Azaneu et al., 2017), data from the GENTOO (Gliders: Excellent New Tools for Observing the Ocean) project in the northwestern Weddell

Sea are used to explore the short-term and spatial variability of the Antarctic Slope Front system and the mechanisms that regulate cross-slope exchange. Data include highly temporally- and spatially-resolved measurements from three ocean gliders deployed in early 2012. Among the several goals of the project, this work contributes to the objective of assessing the impact of changing dense overflows on the locations and strengths of the frontal currents and jets. By calculating composite views of the cross-slope sections, it was possible to identify the average behaviour of the front, as well as the differences that arise due to the presence of the dense flow.

In addition to gliders, the GENTOO project included a hydrographic survey undertaken together with nets and underway biological, chemical and physical measurements. We take advantage of this multiplatform dataset and, in chapter 3, we assess the key areas of primary productivity in study region by characterising the phytoplankton distributions. We also discuss the physical processes associated with plankton spatial variability and how these relate to the slope frontal processes.

Chapter 4 is dedicated to investigate the variability of the warm layer at the shelf-break and inside the troughs in the eastern Amundsen Sea. The data used in this chapter are part of the Ocean2ice project, a consortium led by UEA under the NERC Ice Sheet Stability programme (iSTAR). The project is dedicated to address processes at the continental shelf break and on the continental shelf that affect the heat delivered to the ice shelf front, together with the subsequent fate of the ice shelf meltwater. This work mainly contributes to the assessment of shelf break processes influencing the onshore heat flow. The temperature transport along-slope and along-trough is quantified from six hydrographic sections. These estimates are put into perspective by analysing the variability of the temperature transport per unit area time series calculated for each of the 5 moorings available. A statistical technique is used to assess the short-term variability of these transport time series and help shed light to oceanographic features that might contribute to the observed patterns of variability. The results of Chapters 2 to 4 are synthesised in Chapter 5 (Synthesis and final considerations), and the findings from these two distinct regions (Weddell and Amundsen Seas) are compared.

2

Variability of the Antarctic slope current system in the northwestern Weddell Sea

This chapter has been published in the Journal of Physical Oceanography with the same title (Azaneu et al., 2017). The text in the chapter is included as published. M. V. C. Azaneu was responsible for the work, under supervision of Karen J. Heywood, Bastien Y. Queste and Andrew F. Thompson, who provided scientific input and helped revise the text for publication. The comments from anonymous reviewers also helped to improve the manuscript.

2.1 Introduction

One of the most important aspects of Southern Ocean hydrography is the formation of dense waters on the Antarctic continental shelf, influenced by ocean-atmosphere interaction, addition of ice shelf meltwater, sea ice formation and melting (Foldvik et al., 1985; Nicholls et al., 2009). The production and export of Antarctic Bottom Water (AABW) to the world oceans contributes to the variability of the global overturning circulation deep cell (Talley, 2013), which transports mass, heat, salt, carbon and nutrients, and thus plays an important role in regulating global climate

(Rahmstorf, 2003; Lumpkin and Speer, 2007).

The properties of exported AABW are determined locally around the Antarctic margin through mixing of Circumpolar Deep Water with dense near-freezing shelf waters (Carmack and Foster, 1975; Foldvik et al., 1985). The key element of dense water formation is modification of shelf waters by atmospheric interaction (a cooling and a salinity increase due to brine rejection during sea ice formation, i.e. forming High Salinity Shelf Water - HSSW) or cooling through contact with the base of floating ice shelves (i.e. Ice Shelf Water - ISW). Dense water then leaves the continental shelf and flows down slope, mixing with adjacent water to form AABW. In the Weddell Sea, the dense layer mixes with ambient Warm Deep Water (WDW), which is the Weddell Sea variant of Circumpolar Deep Water, as it flows downslope. As well as producing the densest AABW variety, the Weddell Sea is the main contributor to AABW globally (Rintoul, 1998; Orsi et al., 1999). Huhn et al. (2008) determined that 1.1±0.5 Sv of Weddell Sea Bottom Water (WSBW) was produced in the western Weddell Sea. However, historical estimates of AABW production and export from the Weddell Sea are variable, as a consequence of different methods, water mass definitions and temporal variability (Jullion et al., 2014). Technical limitations on data sampling in continental shelf areas areas also contribute to the low precision of these estimates.

A prominent feature of the circulation on the Antarctic continental shelf and slope is the almost circumpolar westward Antarctic Slope Current (ASC) associated with the Antarctic Slope Front (ASF). The ASC, together with the Antarctic Coastal Current on the shelf close to the coast, constitute the major westward currents of the Antarctic margins (Jacobs, 1991; Heywood et al., 2004). Due to the weak stratification in the region, the ASF is tied to topography (i.e. constant f/H contours), and is generally found close to the shelf break following the 1000 m isobath (Gill, 1973; Whitworth et al., 1998; Heywood et al., 1998, 2004). Previous studies documented changes in the structure and physical processes influencing the ASF and the ASC along its westward path. For example, in the eastern Weddell Sea (17 °W), the ASC is characterized by a surface intensified flow over the shelf break, a separate baroclinic jet over the 1000 m isobath and a predominantly barotropic jet over the 3000 m isobath (Heywood et al., 1998). Further west, at the eastern Antarctic Peninsula continental shelf (between 65 °S and 70 °S, 55 °W), dense waters flow over the slope, and the frontal velocity field is bottom intensified, presenting two cores with strong baroclinic components (Muench and Gordon, 1995). At Joinville Ridge, the flow is also bottom intensified, with two northward-flowing cores, one mainly barotropic at the 1000 m isobath, and another 20 km offshore with an strong baroclinic component (Thompson and Heywood, 2008). Heywood et al. (2004) follow the ASF to the northern flank of the Hesperides Trough and argue that, here, the ASC mixes with waters characteristic of the Weddell-Scotia Confluence, becoming unidentifiable. Recent studies suggest that, rather than becoming completely mixed, part of the ASC crosses the South Scotia Ridge through troughs deeper than 1000 m (Palmer et al., 2012; Meijers et al., 2016).

The continental slope may host multiple fronts, with those further offshore, such as the Weddell Front (WF) (offshore of 2500 m), associated with the deeper outflow of dense waters (Muench and Gordon, 1995; Thompson and Heywood, 2008; Thompson et al., 2009). The WF has been observed from Joinville Ridge, west of the South Orkney Islands, to as far east as 22°E (Orsi et al., 1993; Heywood et al., 2004). Tracks of surface drifters suggest that the current associated with the Weddell front flows cyclonically within the Powell Basin, and along the South Orkney Island plateau, following deep isobaths (Thompson et al., 2009; Thompson and Youngs, 2013). However, there are no recent studies that characterize the properties of the front along its cyclonic pathway, and thus its circulation within the Powell Basin remains speculative.

Because of its topographic steering as well as persistent horizontal gradients of hydrographic properties, the ASF can act as a barrier to cross-slope transport (Thompson and Heywood, 2008). Since the production of dense waters requires property exchange between dense shelf waters and WDW, the formation and export of dense outflow is partially controlled by the strength and position of the ASF (Thompson and Heywood, 2008; Baines, 2009; Gordon et al., 2010; Stewart and Thompson, 2016). In turn, the position and strength of the ASF is sensitive to wind stress forcing on seasonal and inter-annual time scales (Su et al., 2014; Youngs et al., 2015; Meijers et al., 2016). Fluxes across the slope are regulated not only by surface wind forcing, but also by eddy processes. The balance between these two components is argued to lead to the typical V-shape of the isopycnals at the shelf break found in dense water export areas (Gill, 1973; Stewart and Thompson, 2013). Recent studies have discussed the role of mesoscale eddies in cross-slope mass and property fluxes (Nøst et al., 2011; Stewart and Thompson, 2015; St-Laurent et al., 2013), and have shown that wind-driven and eddy-driven transport make comparable contributions to the Antarctic overturning circulation. The combination of these processes regulates the exchange of properties between shelf and oceanic regions (Thompson et al., 2014).

Ocean sampling can be logistically challenging under the rough conditions found in the Southern Ocean. Additionally, the Rossby radius of deformation ranges between 5-12 km over the Antarctic shelf and slope, which complicates observation of oceanographic features such as jets and eddies. New sampling technologies, such as autonomous underwater vehicles, allow data acquisition under rough conditions and with higher spatial resolution (Schofield et al., 2013). The data analyzed in this study were acquired in early 2012 under the multidisciplinary GENTOO project (Gliders: Excellent New Tools for Observing the Ocean). Three Seagliders were deployed in the northwest Weddell Sea, providing data coverage that allowed the identification of dense water spilling off the continental shelf as well as the investigation of the variability of ASF strength and structure at unprecedented temporal and spatial scales.

Section 2.2 describes the dataset, data processing steps and calculations. Results and discussions are presented in sections 2.3 and 2.4 for observations sampled on the eastern Antarctic Peninsula continental slope and western South Orkney Islands, respectively. In section 2.3.1, the properties and transport of the dense water layer sampled by the gliders around Joinville Ridge are presented. Differences and similarities of the ASF hydrography, velocity and transport between sections in the northwestern Weddell Sea are evaluated and discussed in section 2.3.2. In section 2.3.3, composite Potential vorticity (PV) sections are presented for scenarios where dense water is either present or absent. In section 2.4 we present and discuss the properties of the WF on the western South Orkney Island continental slope. Finally, section 2.5 summarises our findings and makes final remarks on the variability of the slope current system flowing around the Powell Basin.

2.2 METHODOLOGY

As part of the GENTOO project, three Seagliders (SG522, SG539 and SG546; Eriksen et al., 2001) were deployed in the northwestern Weddell Sea on the 23rd and 31st of

January 2012; they sampled continuously for 19, 49 and 28 days, respectively. Mission lengths were constrained by both ship availability and the increasing presence of sea ice as summer ended. Gliders SG522 and SG539 were deployed simultaneously over Joinville Ridge, on the eastern Antarctic Peninsula continental shelf, while SG546 sampled the waters on the western South Orkney Island (Fig. 2.1).

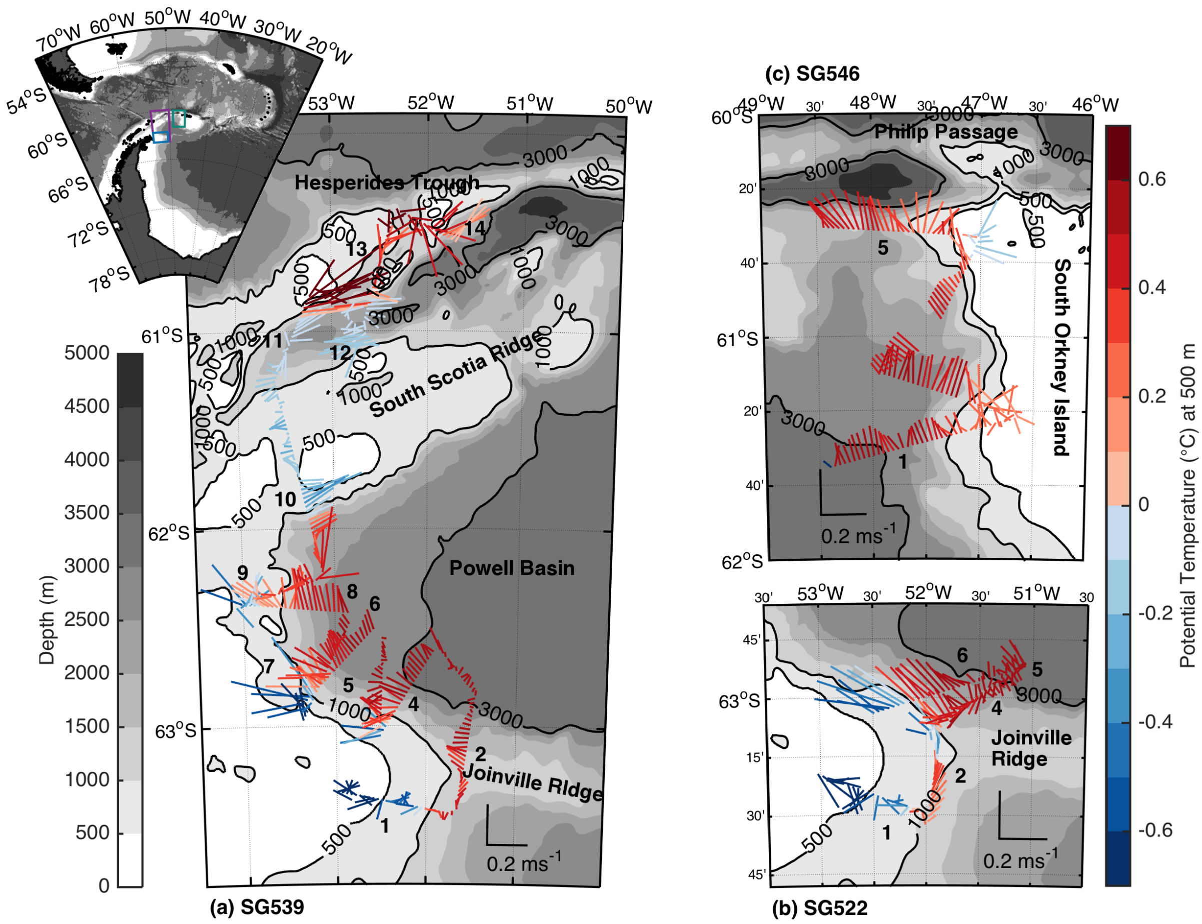

Figure 2.1: Map of the study area showing the Dive Averaged Current (in the top 1000 m) with tidal currents removed, for trajectories for gliders (a) SG539, (b) SG522 and (c) SG546. Gliders were deployed at the southernmost point of their trajectories on the 23rd (SG522 and SG539) and 31st (SG546) of January, respectively, and traveled north while occupying the cross-slope sections. Colors indicate potential temperature at 500 m depth, or the bottom temperature in shallower areas. Note that the 0°C isotherm is the threshold between red-blue colors to denote the position of the ASF. The magenta, blue and green boxes in the inset map of the Antarctic Peninsula highlight the position of panels (a), (b) and (c), respectively.

All gliders were equipped with a Seabird free-flushing CT sail, while glider SG522 also had an Aanderaa oxygen optode. Dissolved oxygen is calculated using the sensor manufacturer's calibration; it is not calibrated against in situ measurements. Temperature and salinity measurements are calibrated between gliders and against CTD profiles, which were calibrated with in situ water samples. The gliders also determined the dive-averaged current (DAC) in the upper 1000 m (Eriksen et al., 2001). In total 790 dives are used in this study, with 1-5 km horizontal and approximately 1 m vertical resolution, resulting in 1580 oceanographic profiles. The gliders typically sampled within 20 m of the sea floor when on the shelf and slope, or to a maximum depth of 1000 m when offshore. Glider data were processed using the UEA Seaglider toolbox (bitbucket.org/bastienqueste/uea-seaglider-toolbox, 29/02/2016) as described by Queste (2013). The glider hydrodynamic model was optimized by minimizing the output of cost functions which prescribe the assumed state of water vertical motion, as described by Frajka-Williams et al. (2011), to obtain improved velocity estimations.

The hydrographic measurements, initially with roughly 1 m vertical resolution, were binned into 5 m means. The profiles were split into 25 horizontal sections and their positions projected onto straight sections. When the glider performed a loop along its trajectory, the data from dives within the loop were excluded. The data were objectively interpolated onto a grid of 5 m vertical and 2.5 km horizontal resolution (using a Gaussian weighting function with vertical and horizontal length scales of 20 m and 20 km, respectively). The speed of the gliders necessarily convolves temporal and spatial variability. Interpolating with a larger horizontal length scale, i.e. 30 km, would help to minimise contamination, or aliasing, by short timescale variability, e.g. tides (Rudnick and Cole, 2011). However, the results were largely insensitive to the choice of 20 or 30 km horizontal smoothing scale and thus we opted for using the former value as it is more in accordance with the front width. Hydrographic values objectively interpolated below the deepest level were excluded to avoid extrapolation over the slope.

The mapped sections were used to compute geostrophic shear. A typical cross-slope section was occupied over a period of 3 days. With an along-slope velocity of approximately 20 km day^{-1} and a typical eddy size of 15–20 km these sections are not true snapshots of the velocity field. Nevertheless, the along-slope current that occurs primarily within the fronts, which are considerably narrower than the entire section, is both nearly synoptic and in geostrophic balance (Heywood et al., 2004; Stewart and Thompson, 2013). Furthermore, our approach of constructing composite sections, described below, addresses this limitation of the glider sections and throughout we emphasize the statistical nature of the variability of the front system over the continental slope. The sampling strategy applied during the campaign sought to fly the gliders in a cross-front orientation, so the cross-section geostrophic velocities captures the primary flow associated with the fronts. We rotate the coordinate system with respect to the section, such that there is a cross-slope and an along-slope component. The absolute alongstream geostrophic velocities were then calculated by referencing geostrophic shear to the component of DAC perpendicular to the section after tides have been removed. Tidal velocities have been removed from DAC using the Oregon State University (ESR/OSU AntPen) (2 km high-resolution Antarctic Peninsula domain) high-latitude barotropic tide model (Padman et al., 2002). Absolute geostrophic velocities are positive downstream, equivalent to cyclonic flow within the Powell Basin and Hesperides Trough.

For each section, cumulative cross-section transport between the sea surface and 1000 m was calculated from absolute geostrophic velocity. In the western Weddell Sea, where the near-bottom velocity is not negligible, flow in the bottom triangle between two adjacent stations can be significant. Thus, for transport estimates, the velocity in the bottom triangle is extrapolated following Thompson and Heywood (2008), in which the geopotential anomaly profile at the shallower station from the pair is extrapolated linearly to the depth of the deepest station. A new geopotential anomaly is then created by a weighted average of the extrapolated values and the values from the deep station.

Hydrographic sections that are not aligned perpendicular to the slope fronts, e.g. Section 2 (SG522 and SG539) and section 3 from all three gliders (Fig. 2.1), were not included in the front analysis. We refer to sections 1-6 (SG522) and 1-10 (SG539) as Powell Basin sections, and 11-14 (SG539) as Hesperides Trough sections (Fig. 2.1 and table 2.1). In cases where the front is crossed twice by a section (i.e. Section 2 SG522 and Section 12 SG539), only the portion enclosing the main flow is included in transport estimates. Section 12 (SG539), for example, crosses the slope on both flanks of the Hesperides Trough, with the associated current flowing in opposite directions (Fig. 2.1). Only the westernmost portion of the section is considered for analysis since the eastern end does not cross the front entirely.

Glider	Sections	Region
SG522	**1**, **2***, 3*, **4**,**5**,**6**	Powell Basin (PB)
SG539	**1**, **2***, 3*, 4, 5, 6, 7, 8, 9, 10	
SG539	11, 12, 13, 14	Hesperides Trough (HT)
SG546	1, 2, 3*, 4, 5	South Orkney Island

Table 2.1: Classification of the different glider sections crossing the slope front system, as seen in Figure 2.1. * indicates sections that do not cross any front and are thus not used in composite sections. Bold numbers indicate stations where dense waters are sampled. These sections are used for dense layer composite sections. The remaining sections within Powell Basin region are used for non-dense layer composite sections.

PV is largely a materially-conserved property in the ocean interior and can be used to identify the susceptibility of the flow to instabilities (Haine and Marshall, 1998). The Ertel PV (Müller, 1995) can be written as:

$$Q = (f\hat{k} + \nabla \times \mathbf{u}) \cdot \nabla b; \tag{2.1}$$

where $\nabla \times \mathbf{u}$ is relative vorticity and $b = -g(\frac{\rho-\rho_0}{\rho_0})$ is the buoyancy. In this study, the geostrophic calculations provide only the cross-section (along slope) velocity component, and therefore it is necessary to simplify PV. The observational PV is then calculated by:

$$PV = -\frac{\partial v}{\partial z} \cdot \frac{\partial b}{\partial x} + \frac{\partial v}{\partial x} \cdot \frac{\partial b}{\partial z} + f \cdot \frac{\partial b}{\partial z} \tag{2.2}$$

The first and second terms on the right hand side of Equation 2.2 are associated with the horizontal and vertical components of relative vorticity, respectively. The third term is the stretching term, which is proportional to the vertical stratification. This simplification assumes that along-stream buoyancy gradients are much weaker than cross-stream gradients, which is verified from adjacent glider sections. We also consider PV along isopycnal surfaces. Geostrophic velocity fields used for PV calculations were filtered using a boxcar (50 m vertical and 7.5 km horizontal scale) averaging filter.

Since the flow associated with the ASF is steered by topography, hydrographic properties interpolated across section were also gridded against local bathymetry. Information from the glider altimeter was used primarily to determine the bathymetry along the sections over the slope. In more offshore areas, where the bottom was deeper than 990 m, the GEBCO (30 arc-second interval grid) dataset was used. The most recent GEBCO dataset includes a large amount of multibeam data (Weatherall et al., 2015), however over the upper slope it is on average shallower than the altimeter data by 36±138 m. The profiles were linearly interpolated to a 50 m resolution isobath grid. The maximum isobath of the grid is 2500 m, which encompasses most of the ASF system. The main steps of the gridding method are exemplified in Figure 2.2. Composite sections with averaged fields were created by averaging the properties on isobaths. Composite mean sections and their respective variances were calculated for regions in which the dense water flow is identified (i.e. Sections 1, 4, 5 and 6 SG522 and 1 SG539), and for the remaining sections within the Powell Basin region (sections 4-10 SG539; Fig. 2.1 and table 2.1). Different sections may cross the front at different angles, and may also have different lengths. Furthermore, the slope varies along the path of the ASF, which complicates the comparison of different sections or the calculation of an average section in distance space (Fig. 2.2d). The composite section performed in isobath space is the natural coordinate system for analysis of a topographically-steered current system.

2.3 GLIDER OBSERVATIONS IN THE NORTHWEST POWELL BASIN

2.3.1 DENSE WATER FLOW

Neutral density at the deepest depth measured by the glider from each dive is presented in Figure 2.3a. The interface between WDW and Weddell Sea Deep Water (WSDW) is generally identified by the 28.27 kg m^{-3} neutral density (γ^n) surface (Fahrbach et al., 2011). Waters denser than this threshold, which will be referred to as the dense water layer, are found over the shelf and slope of Joinville Ridge, south of 63 °S.

In the glider observations, there is no signature of WSBW ($\gamma^n \geq 28.4$ kg m^{-3}, Naveira Garabato et al., 2002). The glider only profiles to 1000 m and, in this area, the WSBW is expected to flow along deeper isobaths (Thompson and Heywood, 2008). Over the upper slope, onshore of the 800 m isobath, Upper WSDW (28.27 kg m^{-3} $\leq \gamma^n \leq$ 28.31 kg m^{-3}; Naveira Garabato et al., 2002) fills the bottom layer at Joinville Ridge.

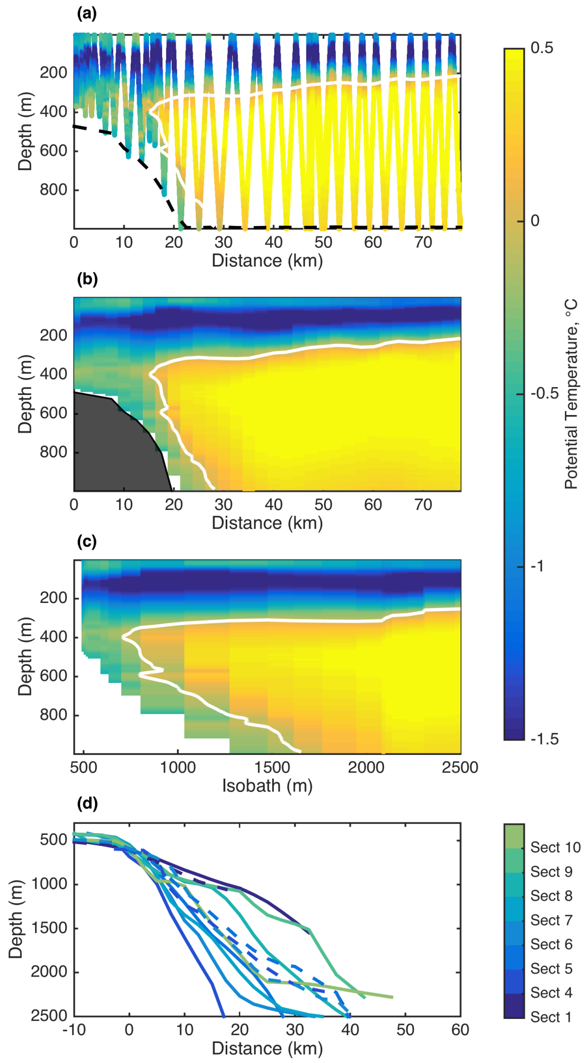

Figure 2.2: Potential temperature (°C) for section 6 SG522 (a) measured along glider dives showing the sampling pattern schematically, (b) interpolated into a straight section and (c) gridded along isobaths. 0 °C isotherm is indicated by the white line. Panel (d) shows the bathymetry along each section used for composite calculations, with distance calculated from the 600 m isobath at each section. Dashed lines indicate sections sampled by glider SG522 (see Figure 1).

Over the slope, offshore of the 800 m isobath, Lower WSDW (28.31 $\mathrm{kg\,m^{-3}} \leq \gamma^n \leq$ 28.4 $\mathrm{kg\,m^{-3}}$) is found at the sea bed. A denser and more oxygenated Lower WSDW is identified south of the main zonal axis of the Ridge (Fig. 2.3b), indicating that it was recently ventilated by shelf waters. Dense waters around the 850 m isobath on the southern flank of Joinville Ridge result from the mixture of WDW, dense shelf waters from Larsen A and B ice shelf regions, and WSBW from greater depths (Caspel et al.,

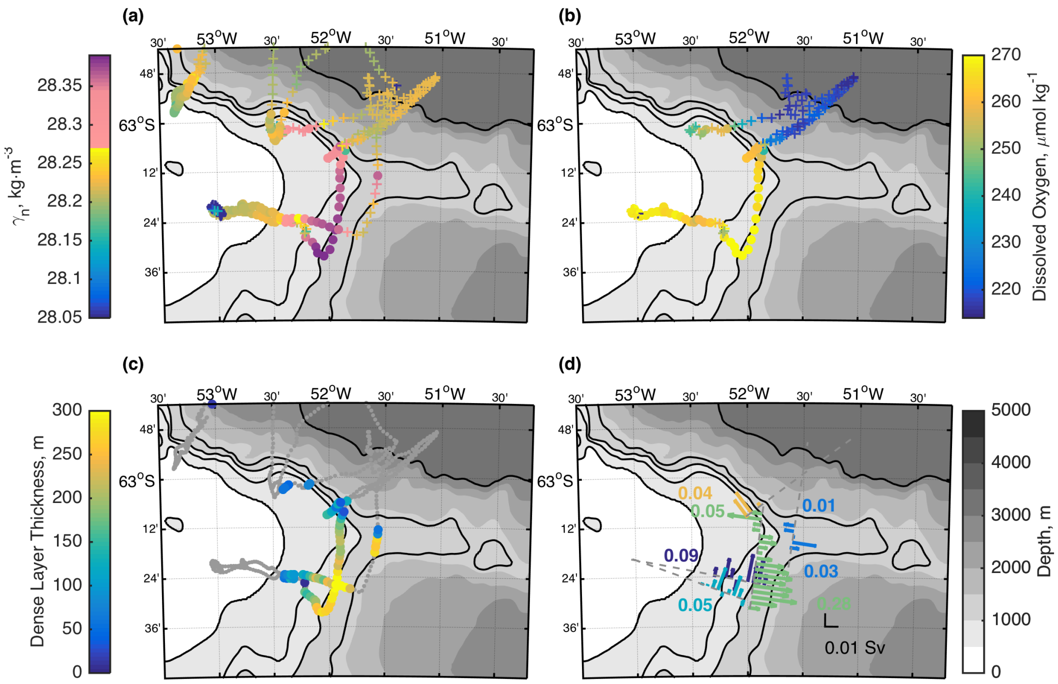

Figure 2.3: Properties at the deepest point of each dive. (a) Neutral density (γ^n, kg m^{-3}); (b) dissolved oxygen (μmol kg^{-1}). Cross symbols indicate dives without altimeter information, or farther than 100 m from the sea bed. (c) Dense layer ($\gamma^n \geq 28.27$ kg m^{-3}) thickness (m). (d) Arrows show the vertically integrated transport of the dense layer, with numbers indicating the cumulative transport (Sv) along each section. Black lines correspond to 500, 800, 1000, 1300 and 3000 m isobaths.

2015). This explains oxygenated Lower WSDW on the southern flank of the ridge, in contrast with the northern slope.

Dense layer thickness was calculated from the shallowest appearance of dense water (Lower and Upper WSDW) to the ocean bottom as indicated by the glider altimeter (Fig. 2.3c). This layer thickness increases by approximately 150 m between the upper slope (800m isobath) and the 1000 m isobath. The layer is thicker (250-300 m) on the southern portion of Joinville Ridge, where denser and more oxygenated Lower WSDW is present (Fig. 2.3b).

The dense layer appears in sections 1-2, 4-6 (SG522) and 1-2 (SG539; Figs. 2.1 and 2.3d, table 2.1). The main circulation pattern of the dense layer along the slope, flowing northeastward and then northwestward around the ridge, is shown by the cross-section transport of the dense flow (Fig. 2.3d). The largest dense water transport among these sections occurs at meridional section 2 (SG522; Fig. 2.1), which presents a dense water flow across the 1000 m isobath, from the shelf to deeper waters, of about

0.3 Sv on southern Joinville Ridge (Fig. 2.3d). In the same area, the dense water flow along the slope is approximately 0.1 Sv.

2.3.2 FRONTAL STRUCTURE

POWELL BASIN HYDROGRAPHY

Section 6 (SG522), which extends 65 km eastward from the 600 m isobath at 63 °3' S, is presented as an example of water mass distribution in the region of Joinville Ridge (Figs. 2.1, 2.4 and 2.5a). At the surface, slightly warmer and fresher water overlies Winter Water over the shelf and slope. Deeper in the water column, the dense water layer is present on the continental shelf and over the slope.

Section 6 (SG522) presents the typical characterization of the ASF as the boundary, below the surface layer, between cold and relatively fresh shelf waters and warmer and more saline waters offshore (Jacobs, 1991; Heywood et al., 2004). The most shoreward extent of the 0 °C isotherm (below the Winter Water) is located within the core of this strong-gradient region, which is a classical identifier for the ASF location (Jacobs, 1991; Whitworth et al., 1998). This position coincides with the V-shape of the isohalines, isotherms and isopycnals which, in this section, is located above the slope, approximately at the 700 m isobath. The position of the front can also be identified by the large change in water mass properties seen in the temperature-salinity diagrams (Fig. 2.4). The distinct temperature and salinity maxima, indicative of the WDW core, change from approximately 0.44 °C and 34.67 east of the 1000 m isobath to a colder and fresher WDW core (approximately -0.23 °C and 34.61) at the 550 m isobath. Located further north of section 6 (SG522), section 8 (SG539) (62 °24' S) does not exhibit dense water flow (Figs. 2.1 and 2.6a). Here the warm core of WDW extends up to the 500 m isobath.

The observations confirm that the position of the 0 °C isotherm is consistent between sections within the Powell Basin. The front location on section 6 (SG522) is similar to that for the composite of all sections that sampled the dense water layer (Fig. 2.5a-c). Fluctuations of the front between the 650 and 800 m isobaths is indicated by the higher temperature variance there (average variance of 0.08±0.04 °C^2 in the area below 250 m; Fig. 2.5e). The higher variance on the slope (average of 0.09±0.05 °C^2) is due to variations in the dense layer thickness (as discussed in

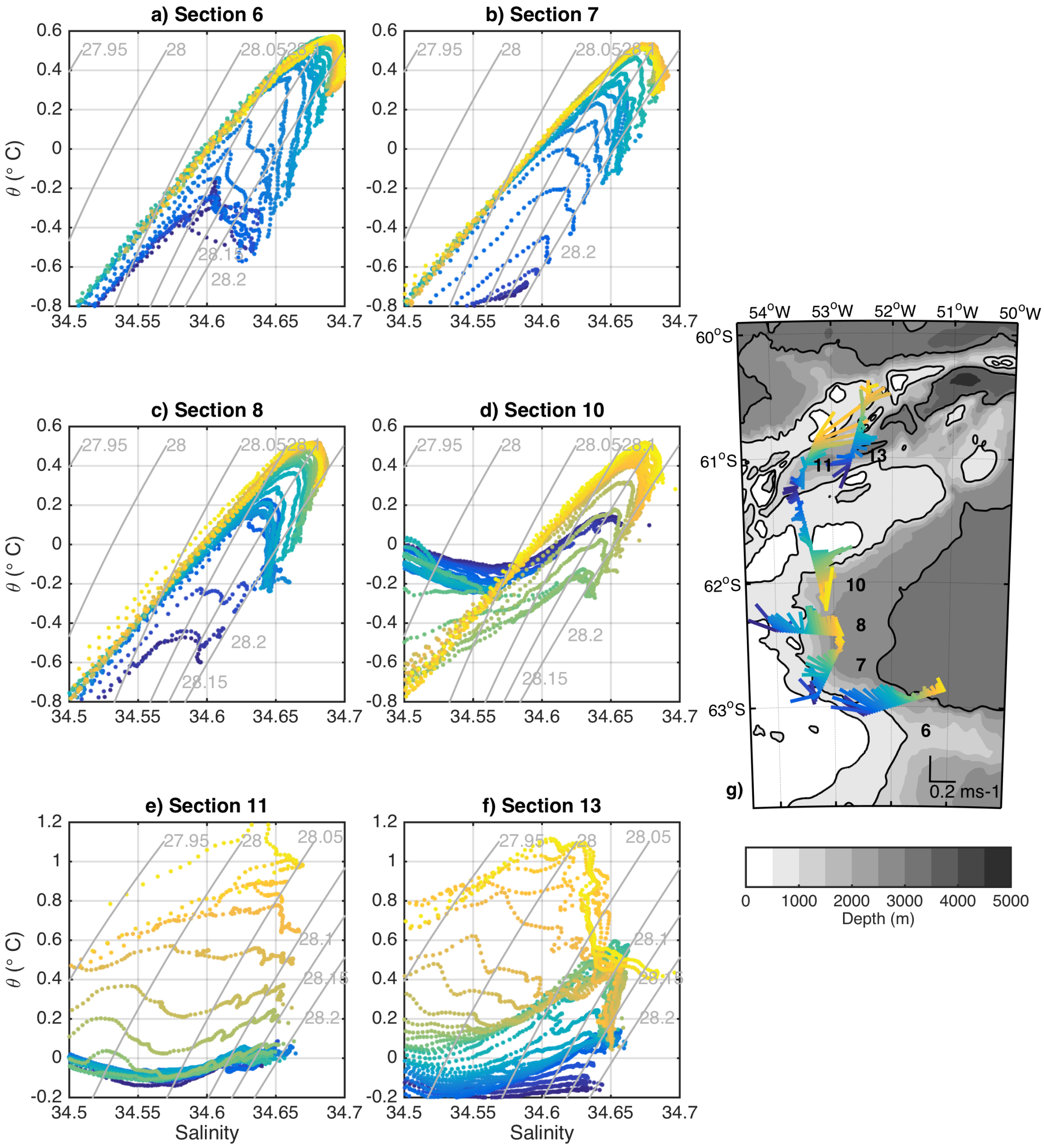

Figure 2.4: Potential temperature-Salinity diagrams (below 200 m) for sections (a) 6 from SG522, (b)7, (c) 8, (d) 10, (e) 11 and (f) 13 from SG539. Neutral density (γ^n) contours are in gray. (g) Map showing DAC of sections presented on panels a-f. Colours indicate different dives along each section, corresponding to colors in panels a-f.

section 3.2.3.1). The average ASF position for sections that do not present dense water flow (Fig. 2.6c) is located further onshore; despite the lower variance (average of 0.03±0.02 °C^2 below 250 m), the ASF positions vary over a broader area (500 m to 1300 m isobaths, Fig. 2.6e) than the sections with dense water. Indeed, Sections 8 and 7 (SG539) represent the most shoreward incursion of the 0 °C isotherm onto the shelf for all sections, while section 10 depicts the most seaward position of the front in the

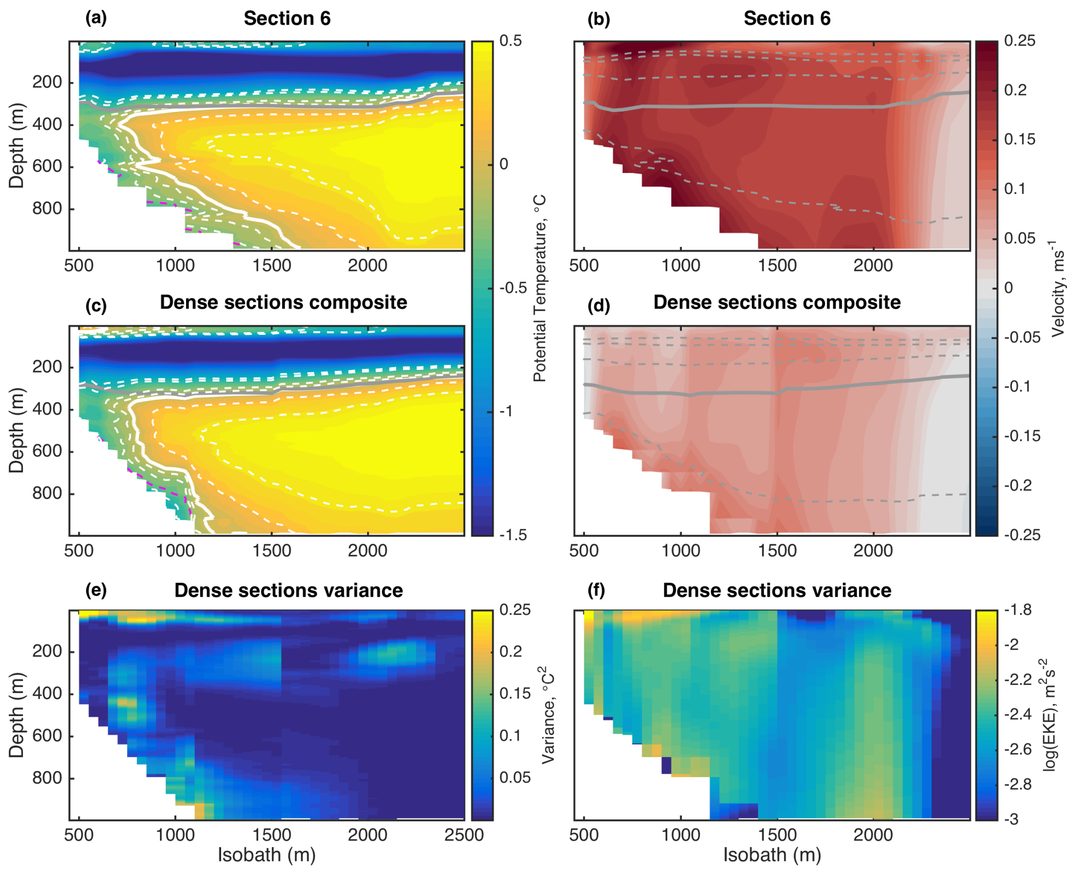

Figure 2.5: (a) Potential temperature (°C) and (b) absolute velocity (V, $\mathrm{m\,s^{-1}}$) for Section 6 (SG522). The composite and variance sections of these properties for all sections that present dense water flow (see table 1) are shown in panels c-d and e-f, respectively. (f) Eddy kinetic energy (EKE, $\mathrm{m^2\,s^{-2}}$) is presented in logarithmic scale. Pink line over the slope indicates dense water layer. Thick white (gray) line indicates 0 °C isotherm (28.1 $\mathrm{kg\,m^3}$ isopycnal). Dashed white (gray) lines show -0.6,-0.5,-0.2,-0.1,0.2,0.4,0.6 isotherms (isopycnals from 27.8 to 28.2 every 0.1 $\mathrm{kg\,m^{-3}}$).

Powell Basin region (at the 1000 m isobath).

Another difference observed between sections 6 (SG522) and 8 (SG539) is that the front is broader in the latter (in geographic space; Fig. 2.1). The maximum horizontal temperature gradient calculated at 500 m decreases from 0.17 $\mathrm{°C\,km^{-1}}$ at section 6 (SG522) to 0.09 $\mathrm{°C\,km^{-1}}$ at section 8 (SG539). Sections 8-10 (SG539) are located in an area where the upper slope is less steep than the southern sections (Fig. 2.1). Here the horizontal temperature gradient is less than 0.1 $\mathrm{°C\,km^{-1}}$; the average for the remaining sections is about 0.17 $\mathrm{°C\,km^{-1}}$. Depending on the slope steepness, the bottom slope may either stabilize the ASC due to the topographic β effect, or

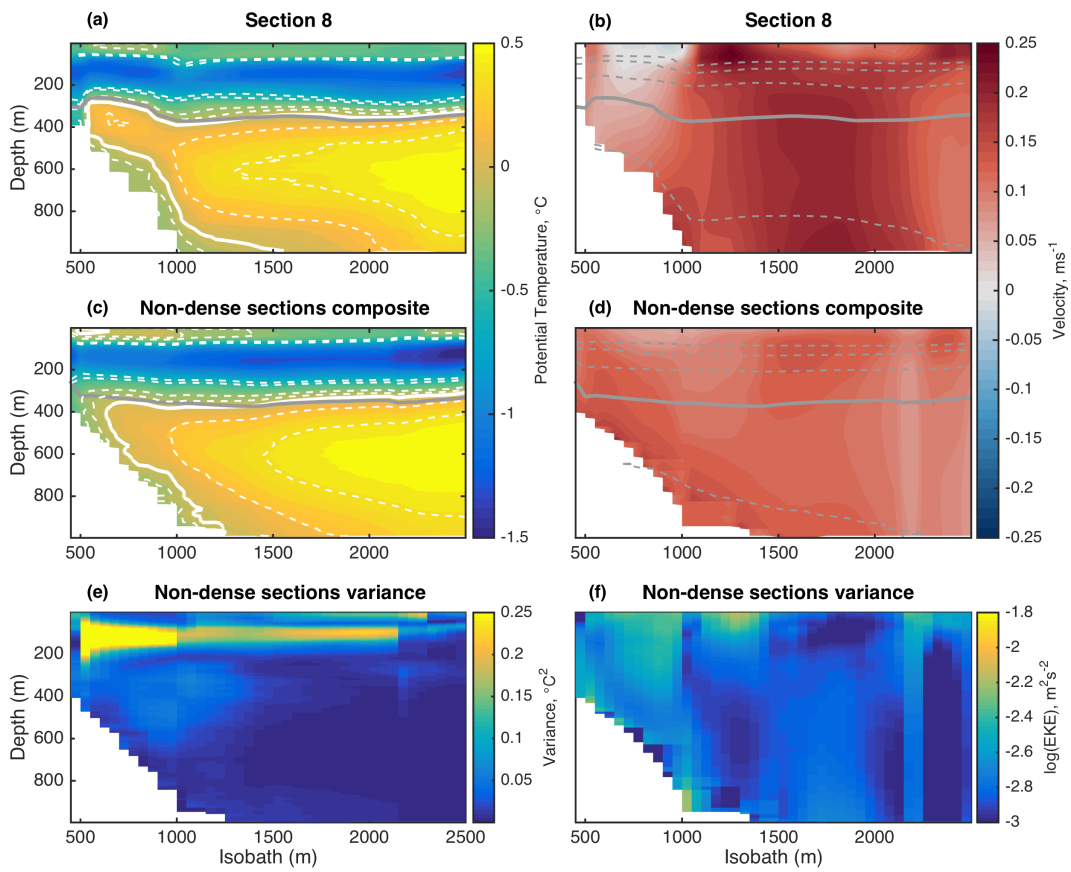

Figure 2.6: (a) Potential temperature (°C) and (b) absolute geostrophic velocity ($\mathrm{m\,s^{-1}}$) for Section 8 (SG539, upper panels). The composite and variance sections of these properties for all sections within the Powell Basin without dense waters (see table 1) are shown in panels c-d and e-f, respectively. (f) Eddy kinetic energy (EKE, $\mathrm{m^2\,s^{-2}}$) is presented in logarithmic scale. Thick white (gray) line indicates 0 °C isotherm (28.1 $\mathrm{kg\,m^{-3}}$ isopycnal). Dashed white (gray) lines show -0.6, -0.5, -0.2, -0.1, 0.2, 0.4, 0.6 isotherms (isopycnals from 27.8 to 28.2 every 0.1 $\mathrm{kg\,m^{-3}}$).

destabilize it due to increase in available potential energy, which can lead to the growth of unstable waves (Tanaka and Akitomo, 2001). Over the Antarctic continental slope (steep slope case), baroclinic instabilities are suppressed, and the destabilizing effect is dominant only on the upper slope. The reduction of the temperature gradient over the region with a more gentle slope, section 8-10 (SG539), is consistent with the argument of Stewart and Thompson (2013).

The velocity composite sections are bottom intensified both where the dense layer is present and for the remaining Powell Basin sections (Figs. 2.5 and 2.6). The average velocity of approximately 0.15 $\mathrm{m\,s^{-1}}$ just above the slope is consistent with studies in which the geostrophic shear is referenced to LADCP measurements (Thompson and

Heywood, 2008).

The Powell Basin along-slope velocity sections show 2-3 main cores, which generally occupy the entire water column, but vary in intensity (from 0.1 to 0.25 $\mathrm{m\,s^{-1}}$) and in position (Figs. 2.5b-d and 2.6b-d). A strong velocity core between the 500 and 1000 m isobaths, coincident with the local shallowest extent of the 0°isotherm, is apparent in all sections. Eddy kinetic energy (EKE) was calculated using the variance of the velocity field composite sections. It is high both in the dense water composite section and in the remaining Powell Basin composite section onshore of the 1000 m isobath, reflecting the variability of the main flow position in the shelf/slope area (Figs. 2.5f and 2.6f). On the composite of variance and EKE sections (Fig. 2.5d-e-f) for sections with dense water, the discontinuities present at the 1000 m and 1500 m isobaths are an effect of the different length of the sections used on the calculation. However, the other visible structures are not artifacts. Sensitivity tests performed using only sections with similar length showed that the multiple velocity cores, as well as the high EKE and its banded pattern, are consistent and robust results. Convergence or divergence of isobaths could also be factors contributing to EKE values. Nevertheless, in the case of the ASC, we believe that changes in the distance between isobaths, between sections (Fig. 2.2d), is not important because almost all the flow is concentrated in narrow frontal jets (Muench and Gordon, 1995; Graham et al., 2013; Stewart and Thompson, 2016).

The velocity cores offshore of the shelf break are found more frequently at the 1000 m and 1500 m isobaths on the composite section with dense water (Fig. 2.5d), whereas they are shifted to 1500 m and 2000 m in the composite section for the remaining Powell Basin sections (Fig. 2.6d). Indeed, the velocity cores are found more frequently at deeper isobaths in the northern sections. However, there is no clear trend in the core positions from one region to another. Even between similar sections (e.g. sections where the dense water is present), there is a variation in the strength (0.1-0.25 $\mathrm{m\,s^{-1}}$) and position of these cores (Figs. 2.5d-f and 2.6d-f). Recent studies have argued that the ASC system is associated with multiple along-slope jets about 30 km wide at the top of the slope (Stern et al., 2015; Stewart and Thompson, 2016). These jets extend throughout the water column and continuously drift across the slope, which could explain the variability observed in the velocity along the ASF pathway. As proposed by Stewart and Thompson (2016), the formation of the multiple along-slope jets could be related to the growth of baroclinic instabilities. These may occur in a turbulent geostrophic flow in the presence of topographic potential vorticity gradient (Vallis and Maltrud 1993) and consumes the potential energy associated with the dense outflow over the continental slope. Our observations, e.g. jet spacing and jet strength, are consistent with Stewart and Thompson (2016) numerical study. Moreover, in sections with a dense layer, EKE peaks within the WDW layer, and the EKE of these sections (average of 0.003±0.002 $m^2 s^{-2}$ below 250 m) is twice as large as those without the dense layer, suggesting a more active eddy field. The banded pattern observed in the EKE composite section (Figs. 2.5f) is similar to that shown by Stewart and Thompson (2016), who associate high EKE values with Circumpolar Deep Water jets and enhanced eddy momentum fluxes.

HESPERIDES TROUGH HYDROGRAPHY

For sections in the Hesperides Trough (i.e. Sections 11 to 13 SG539; Figs. 2.1 and 2.7), the hydrographic conditions change considerably from those in the Powell Basin. The waters at approximately 500 m depth do not exhibit the warm and salty core seen in the Powell Basin sections. Instead, at this depth are found the coldest waters in the water column above 1000 m. This temperature minimum at 500 m is in agreement with Figure 2 of Palmer et al. (2012), which shows that in the center of Hesperides Trough (station 78), the warm WDW core is found at depths (below approximately 800 m) greater than at the eastern Antarctic Peninsula continental slope. Despite this, there remains an intense property gradient present at mid depths (i.e. between 200 and 800 m) that is considered here as associated with the ASF.

In Hesperides Trough, as in Powell Basin, the ASC is associated with the 0 °C isotherm (Fig. 2.7), but the flow is stronger (approximately 0.3 $m s^{-1}$). Section 13 is the northernmost section where it is still possible to track the ASC (Figs. 2.1 and 2.7). In this section the flow separates into two branches following a bathymetric divergence. The bifurcation of the flow observed in section 13 (SG539) is in agreement with the estimated ~1.4 Sv of waters within the 28.1-28.27 $kg m^{-3}$ density range exiting the Hesperides Trough at gaps at 52.5 °W (Palmer et al., 2012). Further downstream (Sections 14 and 15, not shown) the 0 °C isotherm is still present, but at shallower depths and in an area of complex bathymetry, which obfuscates the identification of the front. Because of the ASF's transitional character exhibited at sections within the

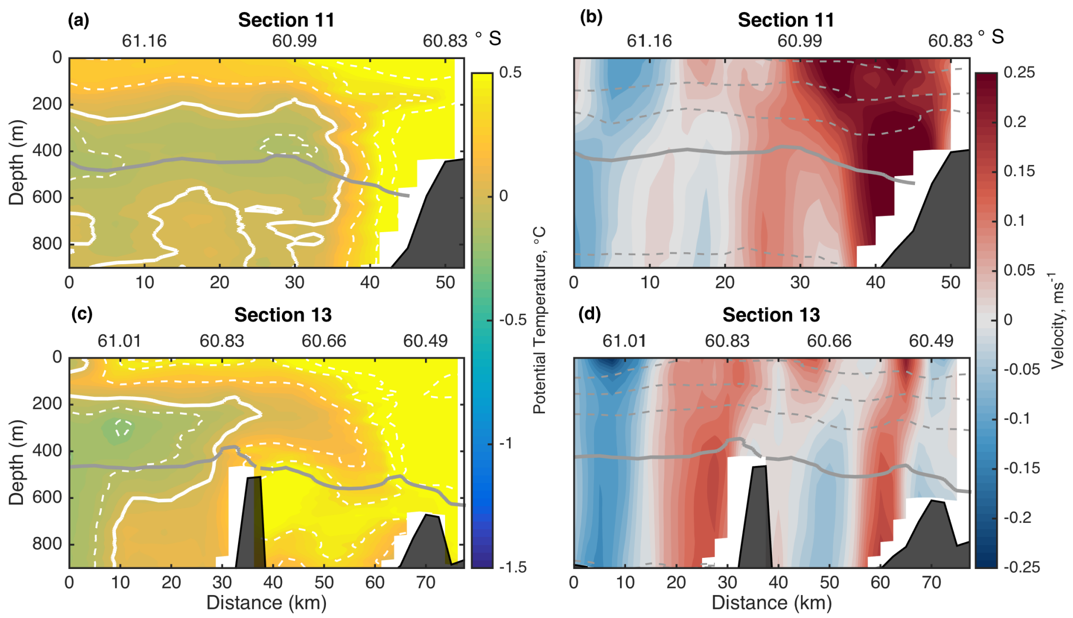

Figure 2.7: (a-c) Potential temperature (°C) and (b-d) absolute geostrophic velocity ($m\,s^{-1}$) gridded against distance along section for sections 11 and 13 (SG539; top and bottom panels, respectively). These are meridional sections, as indicated by the latitude axis at the top of the panel. Positive velocities indicate flow downstream with the slope current (i.e., northeastward at these sections). Thick white (gray) line indicates 0 °C isotherm (28.1 $kg\,m^{-3}$ isopycnal). Dashed white (gray) lines show -0.6,-0.5,-0.2,-0.1,0.2,0.4,0.6 isotherms (isopycnals from 27.8 to 28.2 every 0.1 $kg\,m^{-3}$).

Hesperides Trough region, in conjunction with the local bathymetric complexity, we average only the sections in the Powell Basin area to produce the composite sections.

Whitworth et al. (1998) question the use of the shoreward extent of the 0 °C isotherm to identify the ASF at the northern tip of the Antarctic Peninsula. Our results show that, even though the water masses constituting the ASF are strongly modified along its pathway from the Joinville Ridge to the northeastern Hesperides Trough, there is still a clear horizontal gradient of the hydrographic properties between 200 and 800 m, centered on the 0 °C isobath, that is associated with a strong flow steered by the topography. In this region, flows originating from the Bransfield Strait, shallow South Scotia Ridge and ACC contribute to form the observed property gradient.

The bottom intensification of the ASC is an important aspect identified in the Powell Basin sections, which is also observed in the Hesperides Trough region (Fig. 2.7). This feature is consistent between the majority of sections crossing the front, regardless of the presence of dense water or the latitudinal position (Figs. 2.5 and

2.6). The ratio between the mean velocity in the 50 m above the deepest common level between adjacent stations, to the velocity averaged in the entire water column, averaged for all sections, is greater than 1 shoreward of 1000 m, reaching its maximum (1.5 ± 0.7) at the 800 m isobath (Fig. 2.8b). This value rises to 1.7 ± 0.3 if only Powell Basin sections are considered. Bottom intensification has been associated with the presence of a dense layer, which would tilt isopycnals generating a baroclinic shear that increases with depth (Stewart and Thompson, 2013). Our results show that the bottom intensification occurs both in places where there is dense waters over the slope and in areas where it is not present any more, although it decreases in intensity as the ASC enters the Hesperides Trough. The persistence of this bottom intensification at the ASC in areas downstream of the dense layer region may indicate that the front needs time to adjust to the new conditions without the dense layer.

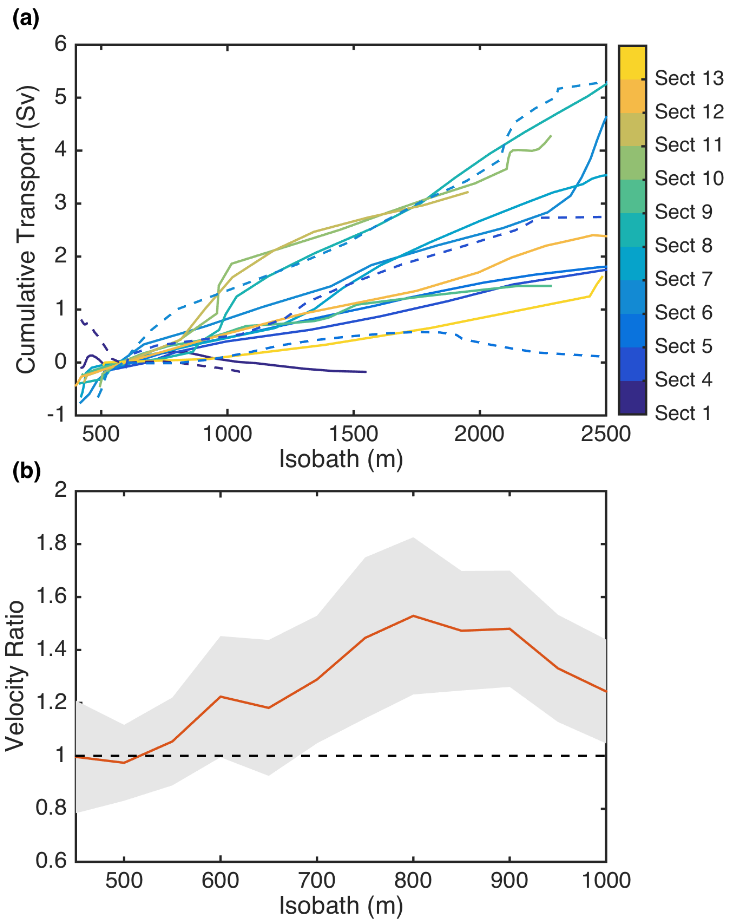

Figure 2.8: (a) Cumulative transport (Sv) above 1000 m, gridded along isobaths and referenced to the 600 m isobath. Colors identify each section from SG522 (dashed lines) and SG539 (solid lines). (b) Average for all sections of the ratio of velocity averaged in the 50 m above the deepest common level between adjacent stations, to the velocity averaged in the upper 1000 m.

TRANSPORT AND VARIABILITY OF THE ANTARCTIC SLOPE CURRENT

The transport estimates reflect variability in the velocity field associated with the ASF (Fig. 2.8a). The ASC cumulative transport between the 450 m and 2500 m isobaths for each of the sections is variable, ranging from 0.2 to 5.9 Sv for sections that reach the 2500 isobath (Fig. 2.8a). At the northwestern SR4 section (approximately collocated with Section 1 from gliders SG522/SG539), Thompson and Heywood (2008) estimated that 3.9±0.3 Sv was due to the ASF contribution, which is within the range of values estimated in our study. The transport estimates along each of the sections do not show a regular pattern or trend. For example, Section 6 (SG522) has the highest transport of all sections. In contrast, the adjacent Section 5 (SG522) has the lowest transport (0.23 Sv). This is quite different from the 2.9 Sv measured 3 days before, in Section 4 (SG522) (an occupation of the same area), suggesting temporal as well as spatial variability.

Modeling and observational work agree on a lag of 4-5 months between a change in wind stress curl and a response of the ASC in the Weddell Sea (Su et al., 2014; Youngs et al., 2015; Meijers et al., 2016). In our results higher frequency variability is apparent, likely controlled by different physical processes, with significant changes between sections sampled about 4 days apart. The differences in the DAC between sections exemplify how the 1000 m-averaged flow can vary substantially over a short temporal and spatial scale (Fig. 2.1). Part of this variability may be associated with data sampling limitations. The sections are not all perpendicular to the frontal jet. This can affect the frontal gradients, geostrophic velocity and cumulative transport estimates. Also, the sections do not all encompass the entirety of the ASF and WF system. With careful analysis, it is possible to successfully estimate cross-frontal gradients from oblique transects (e.g. Todd et al., 2016). The gridding onto isobaths rather than along-track distance somewhat reduces the influence of this bias. However, sampling differences are not expected to be the major cause of the observed variability.

The comparison of sections 4 and 5 (SG522; Fig. 2.9) demonstrates that mesoscale processes are the dominant cause of the observed variability. Sections 4 and 5 are examples of a reoccupation of the same area (i.e. measurements start roughly at the same point and mostly overlay), starting 3 days apart, and therefore sampling differences have minimal impact on the comparison. The sections show different velocities, with total transport estimates differing by 2.7 Sv. In section 5, the absolute geostrophic velocity along most of the section is southward. The flow is only northward in the core of the front. The two sections were sampled over 6 days. Considering an average frontal velocity of 0.1 $m\,s^{-1}$ and deformation radius of 5 km, advection of an eddy-like feature through the section in such a time frame is plausible. Sections 1 (SG522) and 1 and 9 (SG539) may have also sampled an eddy-like feature, associated with a reversal in flow direction at least in part of the section, and with a reduction in transport compared with neighboring sections (Figs. 2.1 and 2.8). Thus, the presence of eddies may have a significant impact on the transport associated with the front and its observed variability.

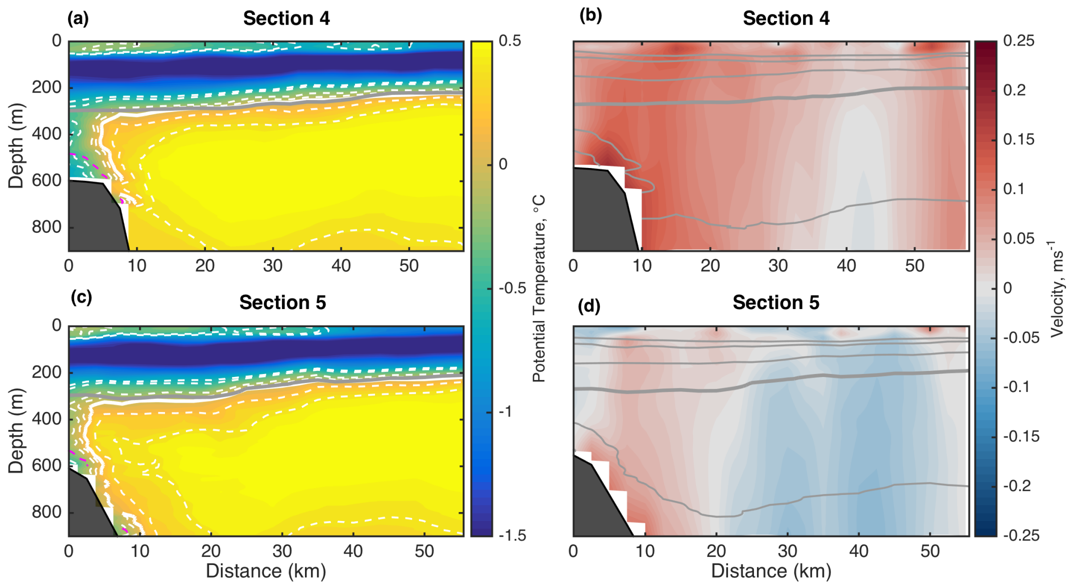

Figure 2.9: (a-c) Potential temperature (°C) and (b-d) absolute geostrophic velocity ($m\,s^{-1}$) for sections 4 and 5 (SG522; top and bottom panels, respectively). Pink line over the slope indicates dense water layer. Thick white (gray) line indicates 0 °C isotherm (28.1 $kg\,m^{-3}$ isopycnal). Dashed white (gray) lines show -0.6,-0.5,-0.2,-0.1,0.2,0.4,0.6 isotherms (isopycnals from 27.8 to 28.2 every 0.1 $kg\,m^{-3}$).

The Antarctic continental shelf and slope are areas of high EKE, where mesoscale eddies are responsible for the transport of water at intermediate depths and heat to the shelf (St-Laurent et al., 2013; Stewart and Thompson, 2016). In the modeling work of Stewart and Thompson (2016), the flow over the continental slope is dominated by eddies with length scale of O(30 km), in agreement with the spatial scale of the reverse flow seen in Figure 2.9. The presence of the eddy-like feature and the weaker temperature gradient seen in section 5 (SG522) in comparison with section 4 (SG522) agrees with the model results of Stewart and Thompson (2016), which show that eddy stirring may contribute to the shoreward heat transport over the upper continental slope.

2.3.3 POTENTIAL VORTICITY

The PV distribution in the composite section that includes the dense water layer is similar to the composite field for the remaining sections within Powell Basin (Fig. 2.10). In both cases the magnitude of PV decreases from the top 100 m towards the ocean interior, reaching values of order 10^{-10} s^{-3} for waters below 500 m (neutral density between 28.15 and 28.2 $kg\,m^{-3}$).

The increase in the magnitude of PV towards the shelf is present in all sections in the western Powell Basin. The greatest horizontal PV gradients are coincident with potential temperature gradients, i.e., with the general position of the front (Fig. 2.10). For waters denser than 28.1 $kg\,m^{-3}$, the PV in neutral density coordinates shows the shoreward enhancement in the magnitude of PV along isopycnals as it gets more negative. Above this dense layer, PV is mostly uniform along isopycnals for most sections. These cross-slope PV gradients indicate a shoreward WDW eddy flux (Thompson et al., 2014). The presence of a topographic PV gradient in a turbulent geostrophic flow could stimulate the formation of the along-slope jets discussed in section 3.b.2.3.2 (Vallis and Maltrud, 1993). In the Hesperides Trough, however, a cross-slope PV gradient is not evident (not shown), suggesting that in this region shelf and slope waters may have already mixed. The steeper slope in the Hesperides Trough (Fig. 2.1) may also suppress eddy generation and consequently cross-front exchange (Isachsen, 2011; Stewart and Thompson, 2016).

Sections with dense water show an increase in the magnitude of PV near the bottom over the slope. All sections in which the dense layer is absent show the minimum magnitude of PV at the densest sampled level (i.e. WDW 28.1-28.2 $kg\,m^{-3}$), characterized by weak vertical stratification. For sections in which dense water is present, however, there is an increase in the magnitude of PV for the bottom layer denser than 28.2 $kg\,m^{-3}$, below the PV minimum. The stretching term is the dominant component of PV in all Powell Basin sections (Fig. 2.10), and its increase in the dense layer is consistent with the increase in stratification there.

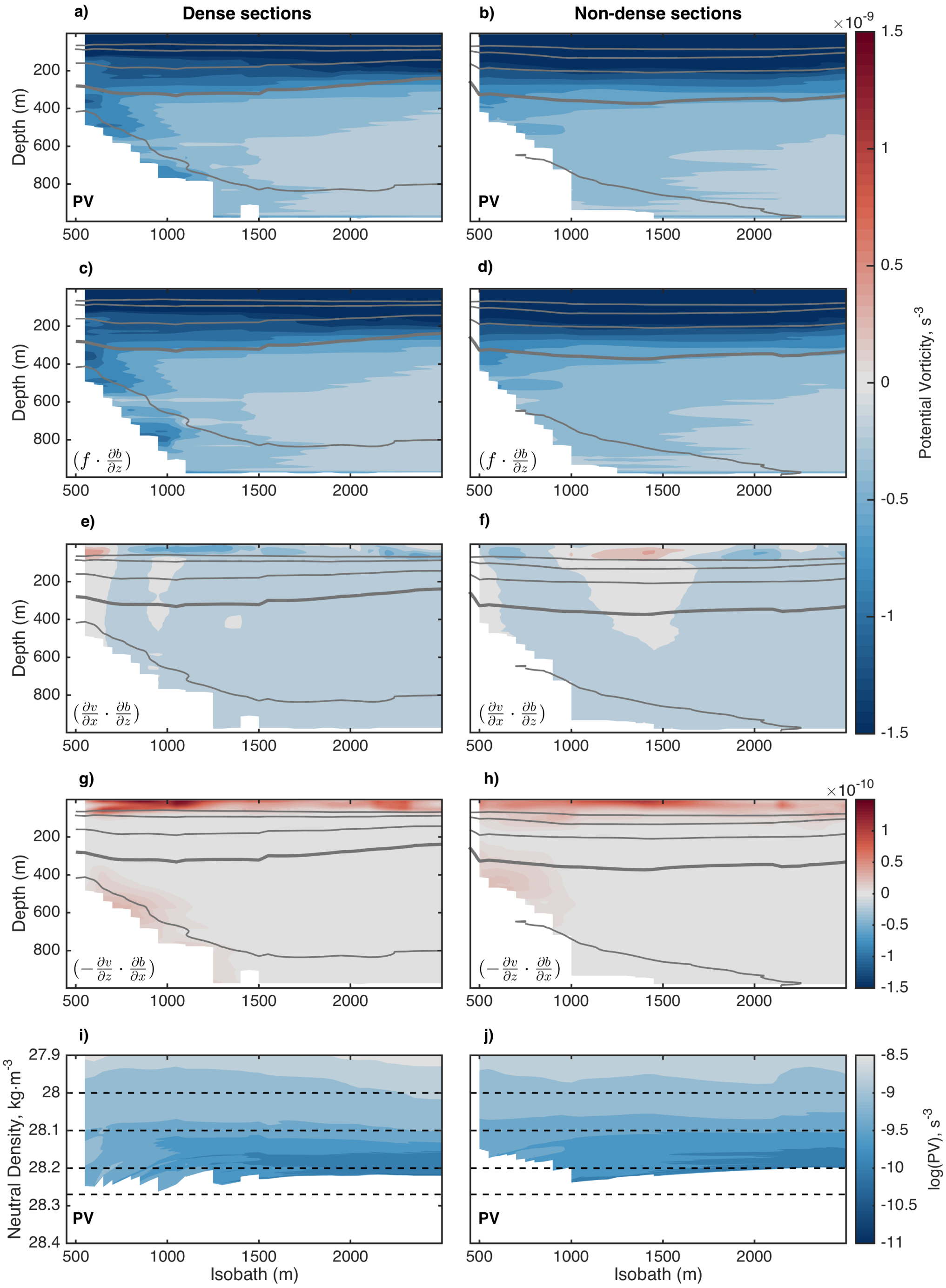

Figure 2.10: (a-b) Composite of potential vorticity (PV, s^{-3}), (c-d) stretching term, (e-f) vertical component of relative vorticity, (g-h) horizontal component of relative vorticity, and (i-j) PV against neutral density surfaces (logarithmic scale), gridded on isobaths. Left panels are composite of sections with dense layer and right panels are composites of the remaining sections within the Powell Basin (see table 1). Thick (dashed) gray lines indicate 28.1 $kg\,m^{-3}$ isopycnal (isopycnals from 27.8 to 28.2 every 0.1 $kg\,m^{-3}$).

The Rossby number ($Ro = \zeta / f \approx (dv/dx)/f$), calculated here as the ratio between the vertical component of the observed relative vorticity ζ and the Coriolis frequency f, is smaller over the upper slope, and greater over the lower slope. The Rossby number is greater when the dense layer is present. The horizontal component of relative vorticity is typically two orders of magnitude smaller than the stretching term and, therefore, has no significant impact on the total PV. Excluding the maximum values in the upper 100 m, the horizontal component of relative vorticity is highest over the lower slope, possibly associated with the bottom intensification of velocity identified in most Powell Basin sections. PV is negative along all Powell Basin and Hesperides Trough sections. Thus, there is no clear indication of susceptibility of the flow to instabilities linked to PV taking the opposite sign of f (Thomas et al., 2013; Ruan and Thompson, 2016). We cannot, however, rule out the possible existence of symmetric instability processes acting on the flow, because these types of instabilities would occur on time scales too short to resolve with glider observations. However, once convection along sloping paths is set up, the symmetric instability can rapidly produce a scenario that allows the development of baroclinic instability (Haine and Marshall, 1998).

The vertical change in the sign of the cross-stream PV gradient can provide an indication of susceptibility of the flow to development of baroclinic instabilities (Pedlosky, 1964; Johns, 1988). The PV gradient of the basic state (roughly, the mean state, considered here as the composite sections) will define the ability of the fluctuations to extract potential energy from the mean flow. The PV gradients for the two sections used as examples in Figures 2.5 and 2.6 (i.e. Section 6 SG522 and 8 SG539) and for the composite sections are presented in Figure 2.11. Below the 28.1 kg m^{-3} neutral density isopycnal, i.e. within the WDW layer, changes in the sign of the cross-stream PV are evident above the slope in sections with dense flow (Figs. 2.11a-c). In sections where the dense flow is absent (Figs. 2.11b-d), these changes in sign are restricted to very shallow areas. This scenario is consistent between sections, i.e., in all cases where the dense water is present, and also on the composite section, there is indication of possible development of baroclinic instabilities on the interface between the dense layer and the WDW above the slope. In the remaining sections this process is constrained to the shelf area. These results are in agreement with the higher EKE observed in the composite section with dense water (Figs. 2.5 and 2.6), which supports the assumption of active baroclinic instabilities at the deep layer.

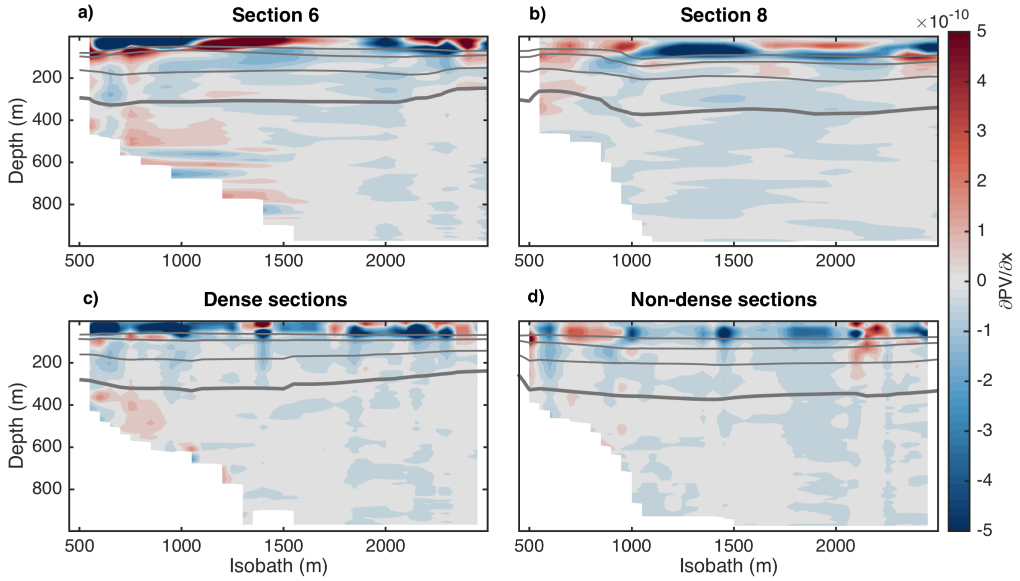

Figure 2.11: Top panels show the cross-stream gradient of potential vorticity (PV) for sections (a) 6 (SG522) and (b) 8 (SG539). Bottom panels show the cross-stream gradient of PV composite section for (c) composite of all dense water sections and for (d) composite of all remaining sections within the Powell Basin.

Stewart and Thompson (2016) suggest that baroclinic instabilities at the pycnocline and at the WDW/AABW interface releases potential energy into EKE, providing energy to the eddy field and mechanical forcing to drive the WDW onto the shelf. Evidence to support their model results is provided by our results showing enhanced variability and greater potential for development of baroclinic instabilities at the bottom boundary when dense layers are present.

2.4 GLIDER OBSERVATIONS IN THE EAST POWELL BASIN

To the west of the South Orkney Island, the main frontal system observed is the WF, which represents the boundary between well-stratified water from the Weddell Sea interior, and weakly-stratified Weddell-Scotia Confluence waters. The current associated with the WF is expected to flow cyclonically around the Powell Basin and to the south around the South Orkney Island, following isobaths (2500-3000 m) deeper than the ASF (Gordon et al., 1977; Heywood et al., 2004; Thompson et al., 2009). Although at the eastern Antarctic Peninsula continental slope the WF is part of the frontal system, to the west of South Orkney Island its properties differ from the ASF and therefore it will be discussed in this separate section.

2.4.1 HYDROGRAPHY

The position of the WF can be identified by a jump in the temperature of WDW (Figs. 2.12 and 2.13), in which water on the Weddell Sea side of the front is warmer and slightly saltier (Heywood et al., 2004). The crossing of the WF can be seen (Fig. 2.13) by the shift from a warm and salty WDW characteristic of the inner Weddell Sea (approximately 0.55 °C and 34.68) to colder and fresher water (approximately 0.4 °C and 34.66). This gradient is associated with the 2000 m isobath. Water with an even colder temperature maximum (approximately 0.22-0.3 °C) is present at a shallower isobath (1000 m).

In Section 5 (SG546), the jump in properties of the WDW warm core to a colder and fresher variant is more evident. From south to north, waters above 200 m become warmer and less stratified. This demonstrates a more direct influence on Weddell Sea WDW of waters from the Weddell-Scotia Confluence possibly through Philip Passage. This is consistent with the circulation pattern simulated by the OSCAR model, which showed a convergence of northward and southward flow in the vicinity of Philip Passage (Youngs et al., 2015).

Both sections 1 and 5 (SG546) show a positive (northward) velocity core shoreward of the 1000 m isobath and another core at approximately the 2000 m isobath (Fig. 2.12). The most striking difference between these two sections is the flow intensity. The northward jets intensify from approximately 0.1 $m\,s^{-1}$ in section 1 to 0.15 $m\,s^{-1}$ in section 5, mostly due to a stronger barotropic component (Fig. 2.1), associated with the WF. These velocities are comparable to the composite velocity of the ASF. The cumulative transport at Section 5 (4 Sv) is double the transport at Section 1.

The observed northward current associated with the WF differs from the pattern previously assumed in this region (e.g. Thompson et al., 2009). A summary of the surface circulation in the study area based on our results and on previous studies is presented in Figure 2.14. Youngs et al. (2015) showed that surface drifters released around Joinville Ridge flow cyclonically within the Powell Basin and then split at the southwest edge of the South Orkney Island, with some flowing south and others

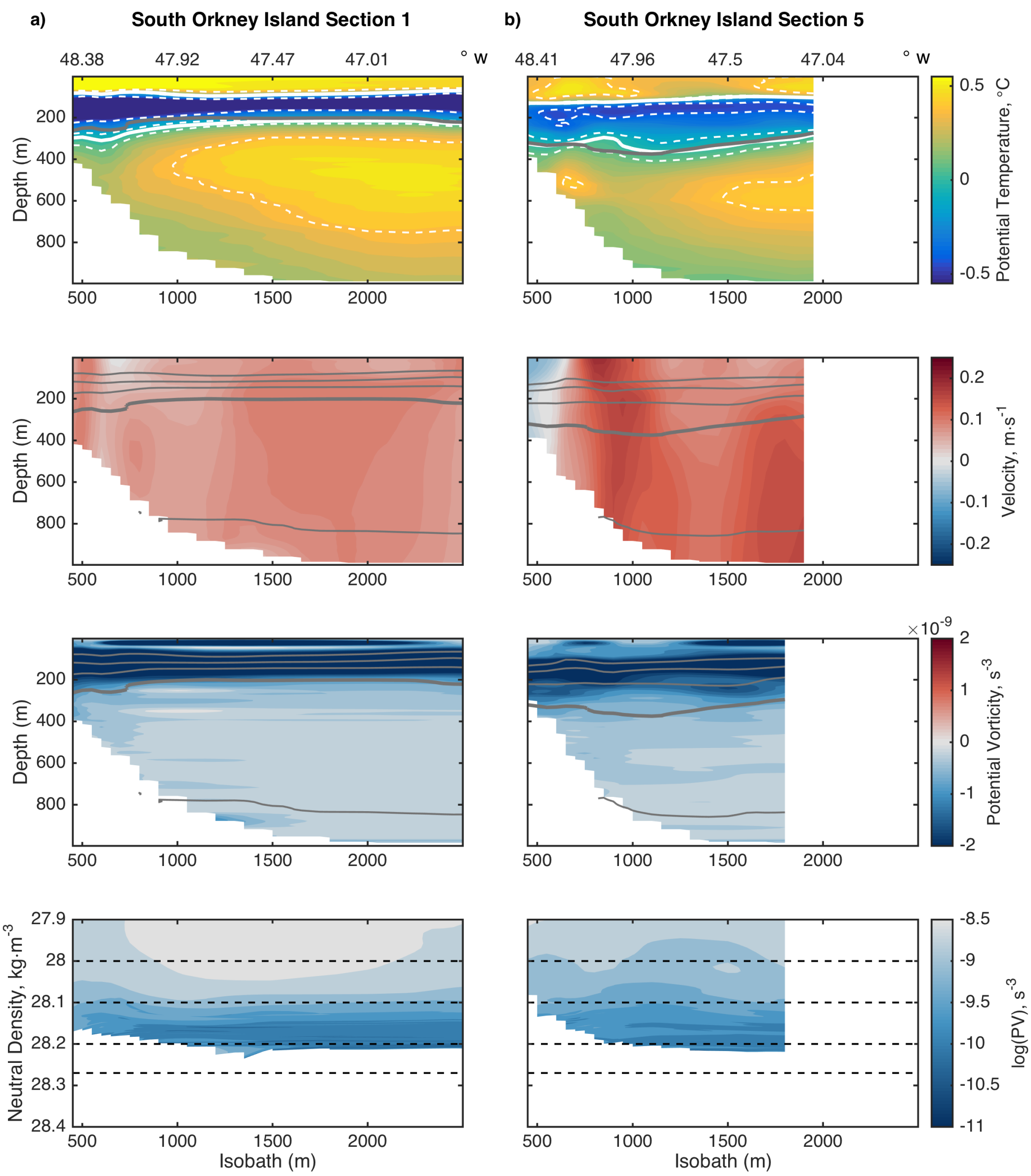

Figure 2.12: Potential temperature (°C), absolute geostrophic velocity ($\mathrm{m\,s^{-1}}$), potential vorticity ($\mathrm{s^{-3}}$) against depth and potential vorticity against neutral density surfaces ($\mathrm{s^{-3}}$, logarithmic scale) on the western flank of the South Orkney Island, gridded against isobaths, for (a) section 1 and (b) section 5 from SG546. These are zonal sections in which the continental shelf is at the eastern end (see Fig. 2.1) as indicated by the longitude axis at the top of the panel. Positive velocities indicate northward flow. Observations from Section 5 are presented only up to the 2000 m isobath.

northward. In the west Powell Basin, at Joinville Ridge, the flow associated with the WF is tied to a range of deep isobaths (Thompson et al., 2009). Thus, it is possible that the more offshore part of the flow associated with the WF follows the deeper isobaths around the basin and south of the South Orkney Island. Meanwhile the more inshore portion of the flow follows shallower isobaths, making a northern

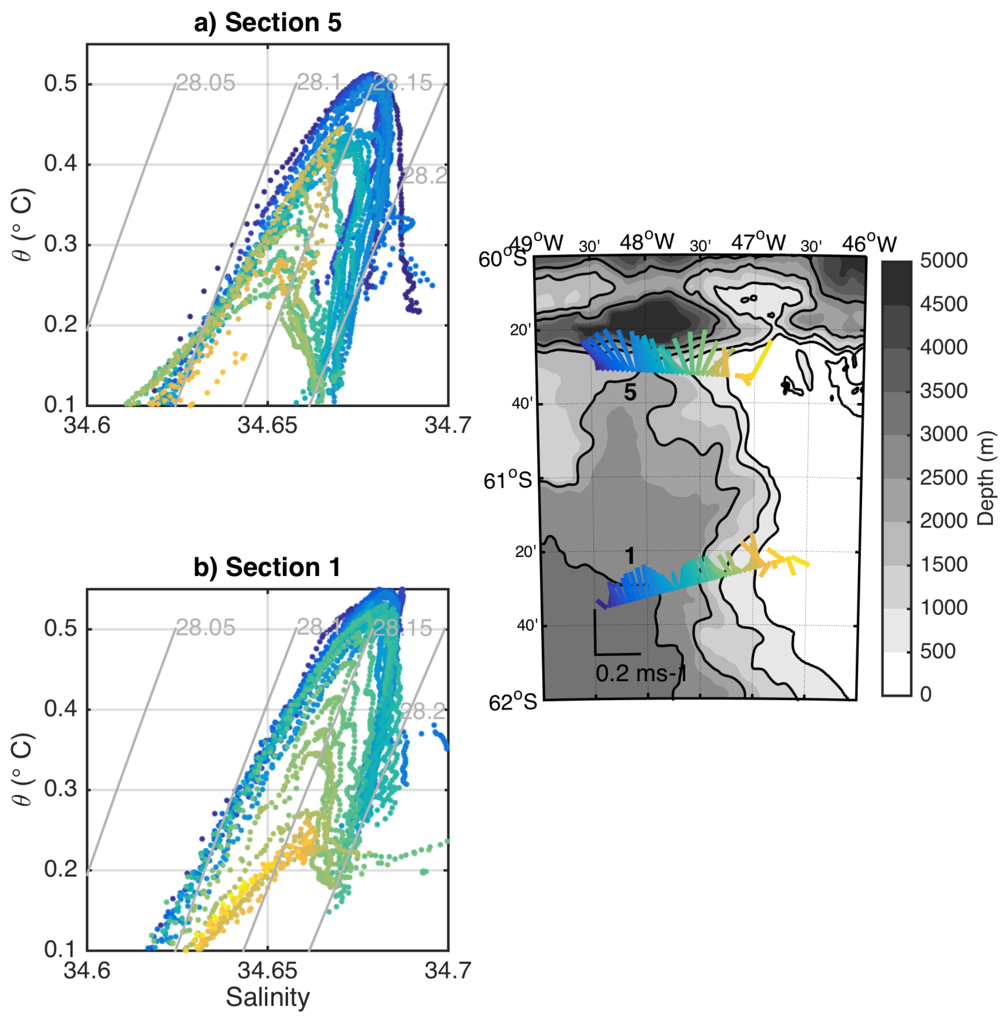

Figure 2.13: Potential temperature-Salinity diagrams (below 200 m) for sections (a) 5 and (b) 1 (SG546). Neutral density (γ^n) contours are in gray. Map shows DAC of sections presented on panels a-b. Colors indicate different dives along each section, corresponding to panels a-b. Black lines indicate the 500, 1000, 2000 and 3000 m isobaths.

incursion around the basin boundaries, and flows towards Philip Passage through the meridional channel west of the South Orkney Island. The bifurcation of the WF pathway proposed in Figure 2.14 agrees with the surface circulation produced by the OSCAR model simulation (Youngs et al., 2015), with modelled tracer trajectories (Meijers et al., 2016) and with the WDW-inferred path within the Weddell Sea (Palmer et al., 2012).

The maximum magnitude of PV seen in the eastern Powell Basin sections (Fig. 2.12) is located below the surface, between 100 m and 200 m, presenting values of

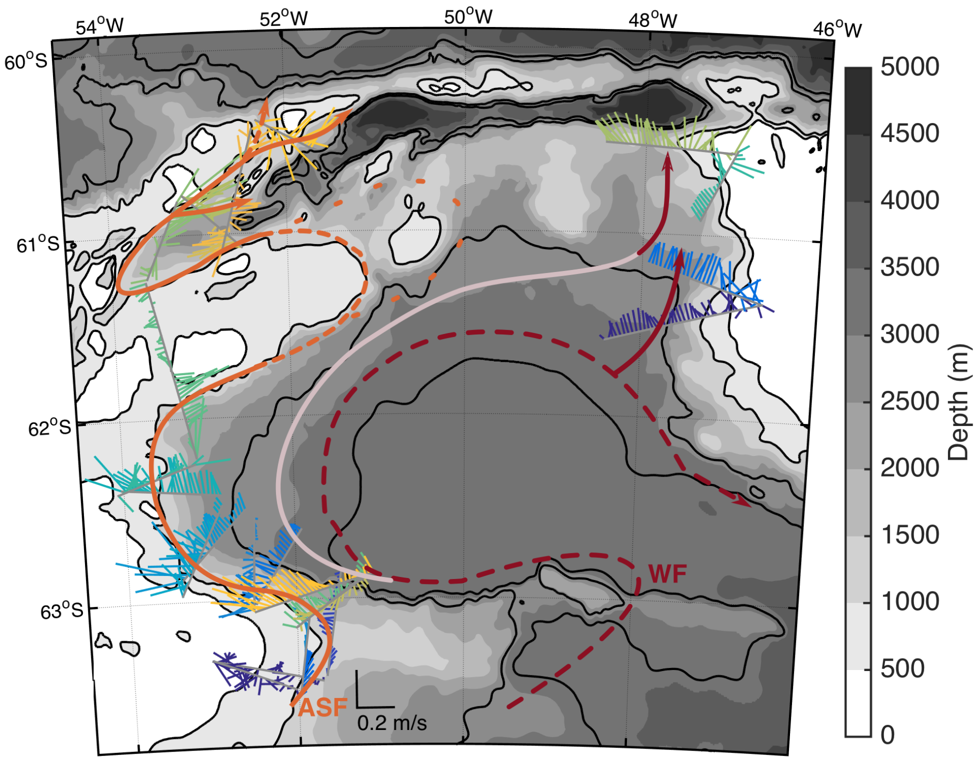

Figure 2.14: Map of the study area with summary schematic of updated circulation of the top 1000 m. Different glider sections are shown in different colors along with the dive averaged currents. Orange line corresponds to the path of the Antarctic Slope Front (ASF) and burgundy line to Weddell Front (WF). Filled lines showing the circulation indicated by the glider data. Dashed and dotted lines are the contributions from Thompson et al. (2009) and Heywood et al. (2004), respectively. Pink line indicates the possible multiple pathways followed by the WF along isobaths, as suggested by the glider data.

$O(10^{-9}s^{-3})$, lower than in the western Powell Basin sections. Sections in the eastern Powell Basin show an increase in the magnitude of PV towards the shelf, although the gradient is generally weaker than for the western Powell Basin. The PV gradient is constrained to a narrower density range (28.15-28.19 $kg\,m^{-3}$) than in the western Powell Basin. As seen for the ASF, the stretching term is the leading component of PV.

2.5 SUMMARY

In our study the Antarctic continental slope region of the northwestern Weddell Sea was sampled with an unprecedented spatiotemporal resolution, providing unique information on both the dense layer and the variability of the ASF system. Offshore of the 800 m isobath, dense waters fill the 300 m thick layer above the sea bed. These waters are richer in oxygen on the southern flank of the Joinville Ridge than on the northern flank. A dense layer transport off the shelf of approximately 0.3 Sv is estimated across the 1000 m isobath, at the southern flank of the Joinville Ridge.

The gliders provided a novel dataset, which allowed a quasi-synoptic view of the ASF. This allowed the first evaluation of the short-term variability associated with the flow. The ASF is a consistent feature with a clear hydrographic signature, but it is also variable and its properties and structure change along its pathway along the Antarctic slope. The high-resolution sampling has tracked the evolution of the ASF around the Hesperides Trough, showing a modification of the frontal structure that is likely to impact shelf-slope exchange. The observations show that the position of the 0 °C isotherm can be used to identify the position of the ASF along its entire pathway from Joinville Ridge to the interior of the Hesperides Trough. The Hesperides Trough region, however, is influenced by Weddell-Scotia Confluence waters, and therefore the ASF hydrographic properties are modified. The results confirm that the front position within the Powell Basin varies between the 500 m and 800 m isobaths. The average temperature variance at the front is $0.08 \pm 0.04\,°C^2$ for sections with a dense water layer.

PV anomalies suggests that, where the dense layer is present, there is a greater potential for development of baroclinic instabilities at the boundary between WDW and AABW, supported by the higher eddy variability observed in these sections. Sections with dense water show greater temperature variance within the dense layer over the slope (average of $0.09 \pm 0.05\,°C^2$ at the dense water layer interface) and higher EKE (average of $0.003 \pm 0.002\,m^2\,s^{-2}$ below 250 m) in comparison with the remaining sections, which supports previous modelling work (Stewart and Thompson, 2016).

The variability of the ASF is observed to be at a higher frequency than previous studies, showing significant changes between sections sampled about 3 days apart. The observed variation in the position of velocity cores between sections is possibly related to the formation and drift of multiple along-slope jets. The variability in the intensity of the flow associated with the ASC does not present a clear temporal or geographical pattern. The effects of changes in slope steepness and the passage of eddies through the region were identified as factors contributing to the observed variability. Sections that sampled eddy-like features show a reversal in flow direction and reduced transport compared with neighboring sections. The combined effect of these two factors can have a significant impact on the transport associated with the front, its observed variability and the cross-slope transport of mass and properties. These results also have implications for the representativeness of previous transport estimates that were composed of a single snapshot (e.g. Jullion et al., 2014; Thompson and Heywood, 2008). Likewise, our estimates are restricted to austral summer and may not be representative of the current at other times of year; there may be variability of the ASF properties and ASC transport on seasonal and interannual time scales. During autumn, for example, shelf waters may undergo freshening coincident with strong along-shore wind and strong negative wind stress curl, leading to a stronger ASF and ASC transport (Graham et al., 2013; Renner et al., 2012; Gordon et al., 2010). Interannual fluctuations of the front properties and strength of the boundary current system are influenced by the Southern Annular Mode and respond to changes in the wind stress curl over the Weddell Sea with a lag of 4-5 months, with stronger cyclonic wind stress leading to a stronger ASC (Renner et al., 2012; Su et al., 2014; Youngs et al., 2015; Meijers et al., 2016). However, the structure of the narrow jets over the slope is unlikely to change. Thus, even though the dataset provides a comprehensive picture of the ASF, during austral summer and early autumn, further monitoring of the frontal system is required to establish the seasonal cycle and detect interannual change (Gordon et al., 2010).

A cross-slope and along-isopycnal PV gradient is a consistent feature of the Powell Basin region (Thompson et al., 2014). This feature is also present west of the South Orkney Island, although the gradients are weaker. In the Hesperides Trough, however, a PV gradient is not evident and the mean flow is stronger than in the Powell Basin sections.

Despite the spatial variability of the ASC, intensification (up to 60%) of the flow velocity at the sea bed is a feature common to the majority of sections. This bottom intensification has been previously associated with the presence of the dense layer (Stewart and Thompson, 2013). The persistence of this intensification in areas where dense waters are absent is a surprising feature, and suggests an adjustment period of the flow, or the existence of other processes that may enhance near-bottom velocities.

The WF exports dense waters from the Weddell Sea (Muench and Gordon, 1995; Thompson and Heywood, 2008; Thompson et al., 2009). The data presented here contribute to a new and more accurate picture of the structure of the flow associated with the WF and its circulation west of the South Orkney Island (Fig. 2.14). Our results show significant differences in hydrographic properties and stratification along the WF, associated with a strong influence of Weddell-Scotia Confluence waters in the northern part of the region, possibly facilitated by Philip Passage. The observed northward current associated with the WF clarifies the pattern previously assumed in this region, agreeing with surface circulation produced by model simulations and surface drifters (Youngs et al., 2015; Meijers et al., 2016).

The glider data evaluated in this study provide one of the most comprehensive data sets to assess the characteristics of the ASF in the western Weddell Sea, both in terms of spatial coverage and horizontal resolution. The results provide an important observational contribution to a growing body of largely numerical evidence that ASF variability is strongly influenced by mesoscale processes. It will be important to understand how the interaction between atmospheric forcing, the mean circulation and ocean eddies at the Antarctic margins responds to a changing climate.

3

A MULTIDISCIPLINARY STUDY OF THE CONTINENTAL SHELF AND SLOPE SYSTEM IN THE NORTHWEST WEDDELL SEA

This chapter is presented as a draft paper.
Azaneu, M., Queste, B. Y., Heywood, K. J., Smith, W. O. Jr, Thompson, A. F., Fielding, S., in prep.
M. V. C. Azaneu carried out the research and prepared the paper. BYQ provided advice on the processing of the glider data. KJH and BYQ provided feedback on earlier drafts.

3.1 INTRODUCTION

The Southern Ocean can be classified as high nutrient-low chlorophyll (HNLC), with primary productivity thought to be limited by low iron (Fe) concentrations (Martin et al., 1990; de Baar et al., 1995; Holm-Hansen et al., 2004; Boyd, 2002; Boyd et al., 2007). The mean annual primary production of the Antarctic continental shelves between 1997 and 2006 (109 $\mathrm{g\,C\,m^{-2}\,a^{-1}}$) represents approximately twice that of the pelagic zone, accounting for area differences (Arrigo et al., 2008b). They are disproportionately important with regard to carbon dioxide (CO_2) sequestration, as they exhibit low surface levels of CO_2 during summer, are sites of active gas exchange, and contribute via advection and deep water formation to the export of anthropogenic carbon (Arrigo et al., 2008a). Antarctic continental shelves support high biomass of higher trophic levels, in particular penguins, seals and whales (e.g., Smith et al., 2014). Continental shelves around Antarctica can be deep, with shelf breaks generally occurring at depths greater than 500 m, and are influenced by subsurface flows onto and off the shelf. These flows provide nutrients that resupply the summer consumption during phytoplankton growth, and heat which at selected locations drives ice shelf melt (e.g., Dinniman et al., 2011). The outflow, at sites of deep water formation, drives the global thermohaline circulation (Rintoul, 1998; Whitworth et al., 1998).

Primary production is dependent on a balance of sufficient light for photosynthesis, the necessary macro and micro nutrients input to produce organic matter and grazing by zooplankton. In the Southern Ocean, mixing and ice cover are the dominant processes governing light availability within the surface mixed layer, while advection, vertical mixing and ice melt regulate macro- and micronutrient supply (Pollard et al., 2002). Modelling studies show that, near the Antarctic Peninsula, primary production is primarily regulated by sediment-derived iron sources, while icebergs, sea ice and atmospheric dust play secondary roles (Wadley et al., 2014). The iron supply can occur by benthic iron diffusion, by enhanced upwelling along the shelf and continental slope, and from sediment resuspension in areas of rugged bottom topography, e.g. the Scotia Ridge (Westerlund and Öhman, 1991; De Jong et al., 2012; Smetacek and Nicol, 2005). The upwelling of macro- and micronutrients can be driven not only by upwelling and topographic interactions but also by eddy motions, which drive localised upwelling/downwelling (Sokolov and Rintoul, 2007). The passage of icebergs calved from ice shelves around the continent has also been reported reported to promote primary production locally (Smith, 2007; Schwarz and Schodlok, 2009; Biddle et al., 2015). The iron enriched shelf waters are likely to contribute to a region of high spring chlorophyll *a* concentrations and phytoplankton biomass which can stretch from the north east of the Peninsula to towards South Georgia (Smetacek and Nicol, 2005; Moore and Abbott, 2000; Holm-Hansen et al., 2004; Thorpe et al., 2004; Abelmann et al., 2006). In the Ross Sea, benthic (brought to euphotic zone by winter convective mixing) and melting sea ice are the largest sources of dissolved iron, while intrusion of Circumpolar Deep Water (CDW; a relatively old and rich water mass, characterised by a local temperature maximum and oxygen minimum) is a secondary but also significant source (McGillicuddy et al., 2015; Kustka et al., 2015). The importance of CDW mixing in supplying dissolved iron at the eastern Antarctic Peninsula is not clear.

Physical and biological processes occurring near the tip of the Peninsula and in the Weddell Sea are influenced by many factors, including the formation of sea ice (Foster et al., 1987), melting of ice shelves (Foldvik et al., 1985) and the complex underlying bathymetry (Orsi et al., 1993; Thompson et al., 2009). The Powell Basin and South Scotia Ridge are particularly dynamic sites where strong along-slope currents, associated with the Antarctic Slope Front (ASF), follow bathymetric contours and may represent a barrier for cross-slope exchange of properties (Thompson and Heywood, 2008). Thus, slope processes associated with the front can potentially influence biochemical exchanges between shelf and open ocean area and affect local primary productivity at the continental shelf and slope. In the pelagic Southern Ocean, Sokolov and Rintoul (2007) show that rather than an area of enhanced production, the fronts associated with the Antarctic Circumpolar Current coincide with boundaries of regions of similar chlorophyll concentrations. At the continental slope area, the role of the ASF in the local primary productivity is still uncertain, partially because of extensive ice and cloud cover, preventing in situ and remote observations. In addition, the continental shelf is characterised by variability at a small spatial and temporal scales due to the shallow depths, weak stratification and small Rossby radius of deformation (typically below 10 km).

The GENTOO project (Gliders: Excellent New Tools for Observing the Ocean) aimed to assess the importance and location of the subsurface slope front in regulating cross-slope exchange in the Weddell Sea using highly temporally- and spatially-resolved measurements from three ocean gliders. In this study, we use a multiplatform dataset to characterise phytoplankton and krill biomass distribution, and assess how the pattern of plankton spatial variability relate to frontal processes east of the Antarctic Peninsula. Specifically, we show that the slope front does not necessarily promote enhanced productivity. We evaluate the differences along the continental shelf between Powell Basin and Weddell-Scotia confluence areas, as well as between on shelf and offshore.

3.2 OBSERVATIONS, METHODOLOGY AND DATA CALIBRATION

The GENTOO campaign consisted of a ship-based survey (23 January–3 February 2012), during which 41 CTD stations were completed (Fig. 3.1). In addition, three Seaglider deployments (SG522: 23 Jan.–14 Feb.; SG539: 23 Jan.–12 Mar.; SG546: 31 Jan.–28 Feb.) were conducted along the western Powell Basin Shelf Break and along the South Scotia Ridge (3.1 and 3.2).

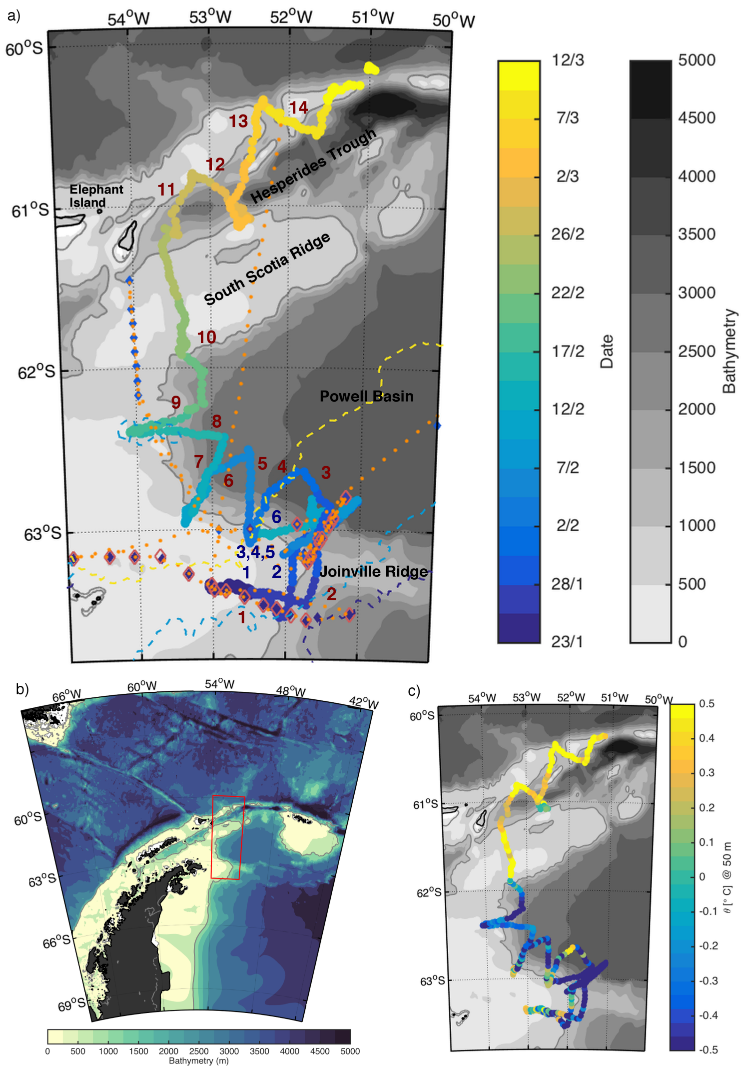

Figure 3.1: (a) Map of study region showing the dataset used. Ship travel, along which krill density was obtained, is shown by orange dots. Filled circles and diamonds indicate glider profiles and CTD stations, respectively, coloured by date of sampling. CTD stations in which water samples were taken are highlighted by pink diamonds. Numbers indicate sections from gliders SG522 (blue) and SG539 (red). Date-coloured dashed lines represent sea ice border on the 24th January, 8th February and 09th March. (b) Map of the Antarctica Peninsula and Drake Passage with the study region highlighted. (c) Potential temperature (θ; °C) from gliders at 50 m.

The ship's sensors were calibrated against in situ samples collected with the rosette and analysed on board and in the laboratory. A total of 120 salinity samples were analysed using a Guildine Autosal and a resulting offset calculated for the ship's CTD conductivity sensor. Salinity is estimated to be accurate to 0.001 and temperature to 0.001 °C. Samples for chlorophyll *a* and particulate organic carbon (POC) were collected in the upper 200 m from the CTD-rosette deployments. Samples (from 270-540 mL) were filtered through Whatman GF/F filters under low vacuum and analyzed by fluorometry using the acid-addition method on a Turner Designs 10-AU fluorometer (JGOFS, 1996). The fluorometer was calibrated using a commercially prepared chlorophyll standard (Sigma), the concentration of which was checked by spectrophotometer and high pressure liquid chromotography (Fig. 3.3a). Particulate matter concentrations were determined by filtering known volumes of seawater (1 L) through combusted GFF filters, drying at 60° C, and pyrolysis on an elemental analyzer to obtain POC concentrations (Gardner et al., 2000). Acetanilide was used as a standard. Along-track Antarctic krill biomass (wet weight, $g\,m^{-2}$) was calculated following Fielding et al. (2016) using multi-frequency acoustic data, and knowledge of krill length-frequency distribution derived from net samples. Three-frequency volume backscattering strength (S_v, dB re 1 m^{-1}) data were collected using a hull-mounted Simrad EK60 echo-sounder (38, 120 and 200 kHz). Krill were sampled to provide parameters required in the target strength model for krill biomass estimation. Krill were sampled using a rectangular mid-water trawl with a rectangular 8 m^2 mouth opening (RMT8). A total of 7 trawls were targeted on acoustic marks identified in the glider-deployment regions from the ship's real-time EK60 data display. Each trawl was comprised solely of Antarctic krill and ca. 100 krill from each measured for length. The mass-to-length relationship calculated for the Scotia Sea in 2000 (Hewitt et al., 2004) was used to convert krill abundance to krill density, which was integrated along-track per 500 m travelled. The krill density was not uniformly distributed along hours of the day, showing a more diurnal pattern. Based on the hourly distribution of the krill density, estimates made between 7h and 19h presented the highest values and were then selected for the analysis.

Gliders SG522 and SG539 were capable of sampling to 1000 m and were equipped with a Seabird conductivity - temperature package and a WetLabs triplet ECO puck measuring chlorophyll *a* fluorescence, coloured dissolved organic matter

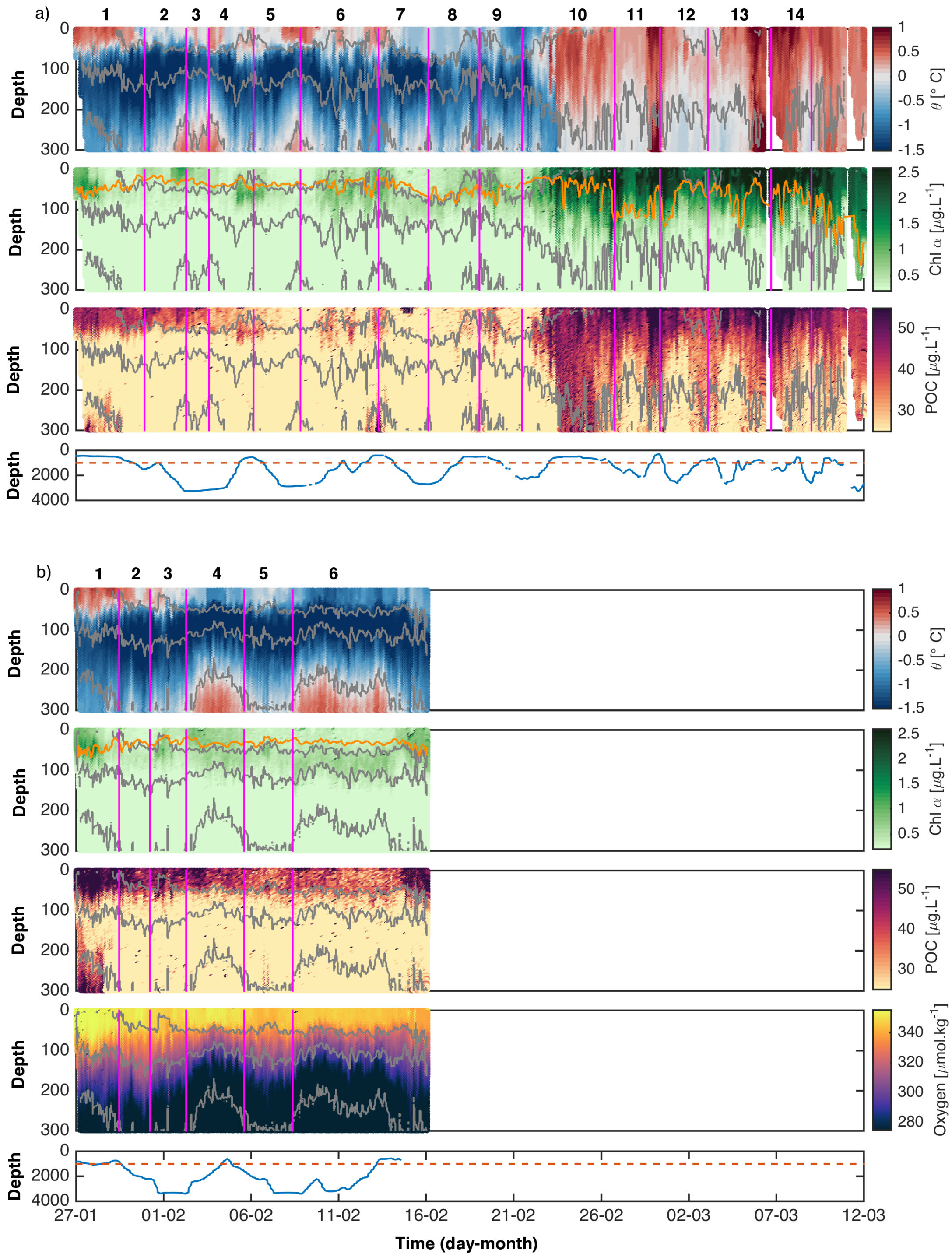

Figure 3.2: a) Time series of potential temperature (θ; °C), chlorophyll a (Chl α; μg L^{-1}) and particulate organic carbon (POC; μg L^{-1}) concentration for gliders SG539 (a) and SG522 (b). Pink lines indicate beginning of each transect (see Fig.3.1), as indicated by the numbers. Grey lines are isopycnals 27.65, 27.95 and 28.1 kg m^{-3}. Orange line indicates the MLD. Bottom panels in (a) and (b) indicate local bathymetry. Orange dotted line marks 1000 m depth.

fluorescence and optical backscatter (SG522 at 532 nm; SG539 at 650nm). SG522 was also equipped with an Aanderaa 4330 optode with a fast response foil. Glider temperature and salinity are estimated to be accurate to 0.005°C and 0.01, respectively. Temperature and salinity data from the gliders were calibrated against available ship CTD data along sections 1 and 2 by matching profile peaks in potential temperature and salinity space. Glider chlorophyll *a* concentrations were estimated by regressing glider observed fluorescence against CTD casts performed alongside the glider dive. Optical backscatter values obtained from the glider optical sensor were converted to POC concentrations (Kaufman et al., 2014). Total volume scattering, β (124°, 532 nm for SG532 and 650 nm for SG539) was calculated from raw scattering using a factory-calibrated scale factor. Particulate optical backscattering (bbp; wavelengths 532 nm for SG532 and 650 nm for SG539), was estimated from total volume scattering by subtracting the volume scattering of seawater, β_w (Morel, 1974), and applying a factor of $2\pi\chi$, where $\chi = 1.01$ (following Boss and Pegau, 2001). The backscatter-based POC estimates were then calibrated against ship POC samples (Figs. 3.1 and 3.3). The closest profile within a 10 km radius from each station was used in the regression. Dissolved oxygen is calculated using the sensor manufacturer's calibration; it is not calibrated against in situ measurements.

Both gliders traveled northwards while repeating transects along the Powell Basin continental slope (Fig. 3.1). SG522 covered section 1 and 2, repeated section 3 three times (sections 3–5), and then sampled section 6. SG539 performed each section (sections 1-14) sequentially before heading into the Weddell–Scotia Confluence (WSC) where it surveyed the SSR (Fig. 3.1). In total, glider SG539 sampled 15 sections. The sections were sampled in a cross-front orientation, in which the upper slope and off-shore regions were sampled. Sections 1 from SG522 and SG539 are the most on-shore sections, sampling the on-shelf upper slope areas. Glider data were gridded into 4 m vertical bins taking median values, and any gaps were filled with linear interpolation. Derived properties, such as geostrophic velocity, were calculated after objectively interpolating the data horizontally onto a 2.5 km horizontal resolution grid (using a Gaussian weighting function with vertical and horizontal length scales of 20m and 20 km, respectively). Absolute velocities were obtained by referencing geostrophic velocities to de-tided DAC (dive-averaged currents; Eriksen et al., 2001). Tidal currents were estimated using a barotropic tide

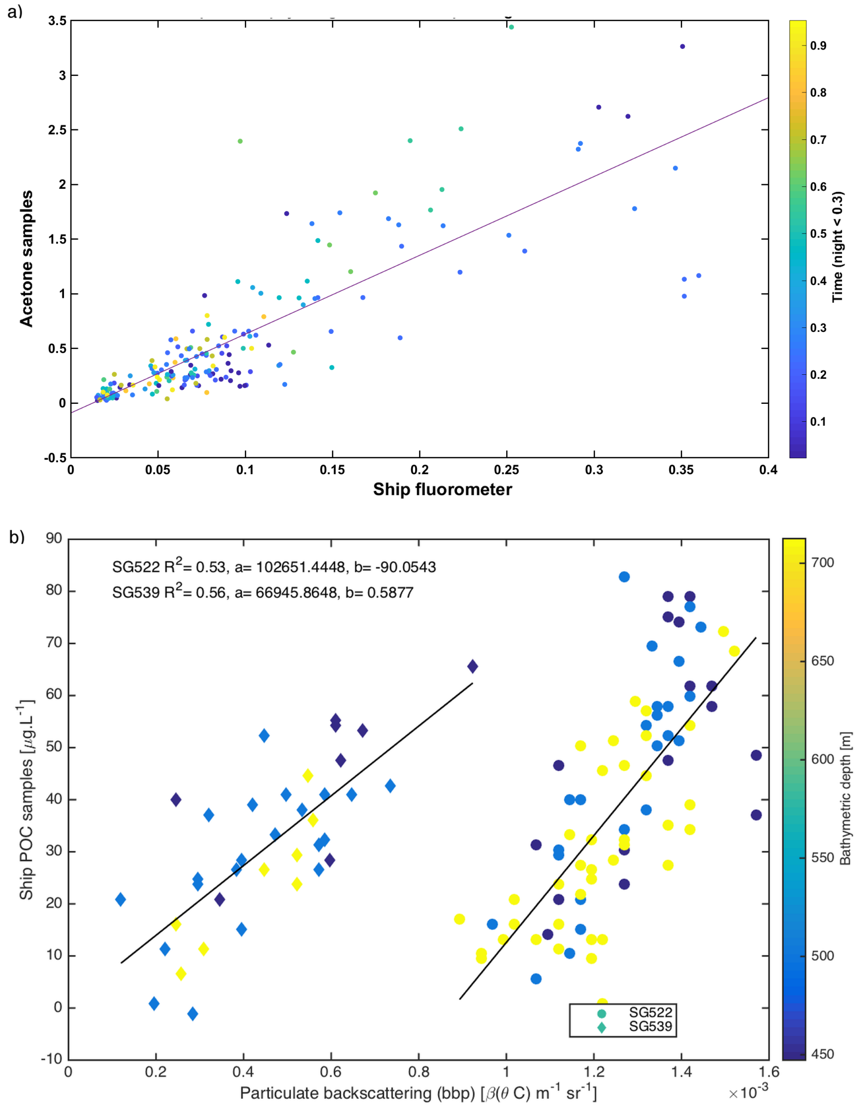

Figure 3.3: a) Ship chlorohyll *a* against samples (only those collected during night time or below 50 m), coloured by time. b) Linear regression between particulate backscattering (bbp) from Seagliders SG522 and SG539 and the ship particulate organic carbom samples, coloured by bathymetric depth.

model (Padman et al., 2002). Other properties derived from the glider hydrographic sections were the observational Ertel Potential Vorticity (PV; Müller, 1995) and the Turner Angle (Ruddick, 1983). PV is a largely conservative quantity on isopycnals if diabatic processes are small. More details on the PV calculation using the glider data are provided by Azaneu et al. (2017). The Turner angle expresses the relative contribution of the vertical gradients of potential temperature and salinity to the vertical stability (N^2). The Turner angle differentiates between "diffusive" regime (angles between -90°and -45°), salt-fingering regime (angles between 45°and 90°), and a statically unstable water column ($N^2 < 0$; angles ≥ 90°or ≤ -90°). A turner angle between -45°and 45°represent regions where the stratification is stably stratified in both temperature and salinity. The mixed layer depth (MLD) is defined as the depth at which the potential density differs by a threshold value of 0.03 kg/m^3 from the potential density at 10 m depth (Dong et al., 2008).

3.3 HYDROGRAPHIC CONTEXT

The main water masses present at the Powell Basin shelf break and slope area are Antarctic Surface Water (AASW), Warm Deep Water (WDW; regional variety of the Circumpolar Deep Water) and Antarctic Bottom Water (AABW; Fig. 3.4). AASW properties are variable spatially and temporally due to interaction with sea ice and atmosphere. During summer, AASW comprises a relatively warm and fresh surface layer above the subsurface near-freezing temperature minimum of Winter Water (WW), which is the remnant of the winter mixed layer (Whitworth et al., 1998; Palmer et al., 2012). This temperature minimum is present all year in the open ocean because of the presence of warmer WDW ($\gamma^n \geq 28.01$ kg m^{-3}) beneath it. WDW is characterised by a temperature maximum, and a salty and low oxygen core, derived from Circumpolar Deep Water (Heywood and King, 2002). The permanent pycnocline between WW and WDW in the open ocean regime defines the lower limit of AASW (at approximately 300m). Over the shelf, the AASW layer may overlie a layer of waters as dense (called modified WDW) or denser than the WDW, which is the case for sections 1, 2, 4, 5, and 6 (SG522) and 1 and 2 (SG539; Figs. 3.1 and 3.2; Azaneu et al., 2017). Waters denser than WDW are defined as AABW ($\gamma^n \geq 28.27$ kg m^{-3}) and, if denser than 28.27 kg m^{-3} and colder than -1.7°C, as Shelf Water (Whitworth et al., 1998). There is possibly not a barrier for the communication of surface waters from the oceanic and the shelf regime, however, the properties of these waters can be influenced by processes that are particular to the two different regimes. The horizontal subsurface gradient between the thickened layer of relatively cold and fresh AASW with the warmer and saltier modified WDW is known as the Antarctic Slope Front (ASF; Jacobs, 1991; Whitworth et al., 1998; Heywood et al., 1998). The temperature and salinity horizontal gradients defining the front also represent a horizontal gradient in density, and thus there is a steepening of the slope of the isopycnals where the WDW reaches the continental slope (Heywood et al., 1998). In regions where the shelf dense waters are present, the AASW shoals again, leading to a “V-shape" in isopycnals (for example for sections over Joinville Ridge). If the dense shelf water is absent, there is just the off-shore side of the “V". North of the South Scotia Ridge, in the Hesperides Trough region, the complex topography helps promote the confluence of different open-sea and shelf water masses. The ASF properties are modified by the contribution of waters originating from the Bransfield Strait, shallow South Scotia Ridge, and ACC. In the centre of Hesperides Trough, the warm WDW core is found deeper in the water column than in the Powell Basin region (Palmer et al., 2012; Azaneu et al., 2017). The classical identifier of the ASF location is defined by the most shoreward extent of the 0°C isotherm (Jacobs, 1991; Whitworth et al., 1998). The ASF is generally found close to the shelf break (Gill, 1973; Whitworth et al., 1998; Heywood et al., 1998, 2004), mostly between the 500-800m isobaths (Azaneu et al., 2017). Because of the persistent horizontal gradient of properties, the ASF act as a barrier for cross-slope exchange for waters within the WDW density range. However, its role in the cross-slope exchange at surface waters is not certain (Thompson and Heywood, 2008).

The westward geostrophic current associated with the slope front is the Antarctic Slope Current (ASC), which is topographically steered (Thompson et al., 2009; Azaneu et al., 2017). The ASC flows cyclonically around the Powell Basin; as it encounters the South Scotia Ridge, the majority of the flow follows the slope along the southern edge of the ridge and enters the Hesperides Trough region. Part of the flow turns west and enters the Bransfield Strait, while part of it merges into a large standing eddy over the South Scotia Ridge (centered at 62°S and 54°W; Thompson et al., 2009). This anticyclonic eddy is a permanent feature of the circulation and has a diameter of approximately 40 km. Drifters released in the region remained trapped in this recirculation for up to a month (Thompson et al., 2009). During the research cruise, CTD stations were occupied and krill density was estimated across the standing eddy (Fig. 3.1).

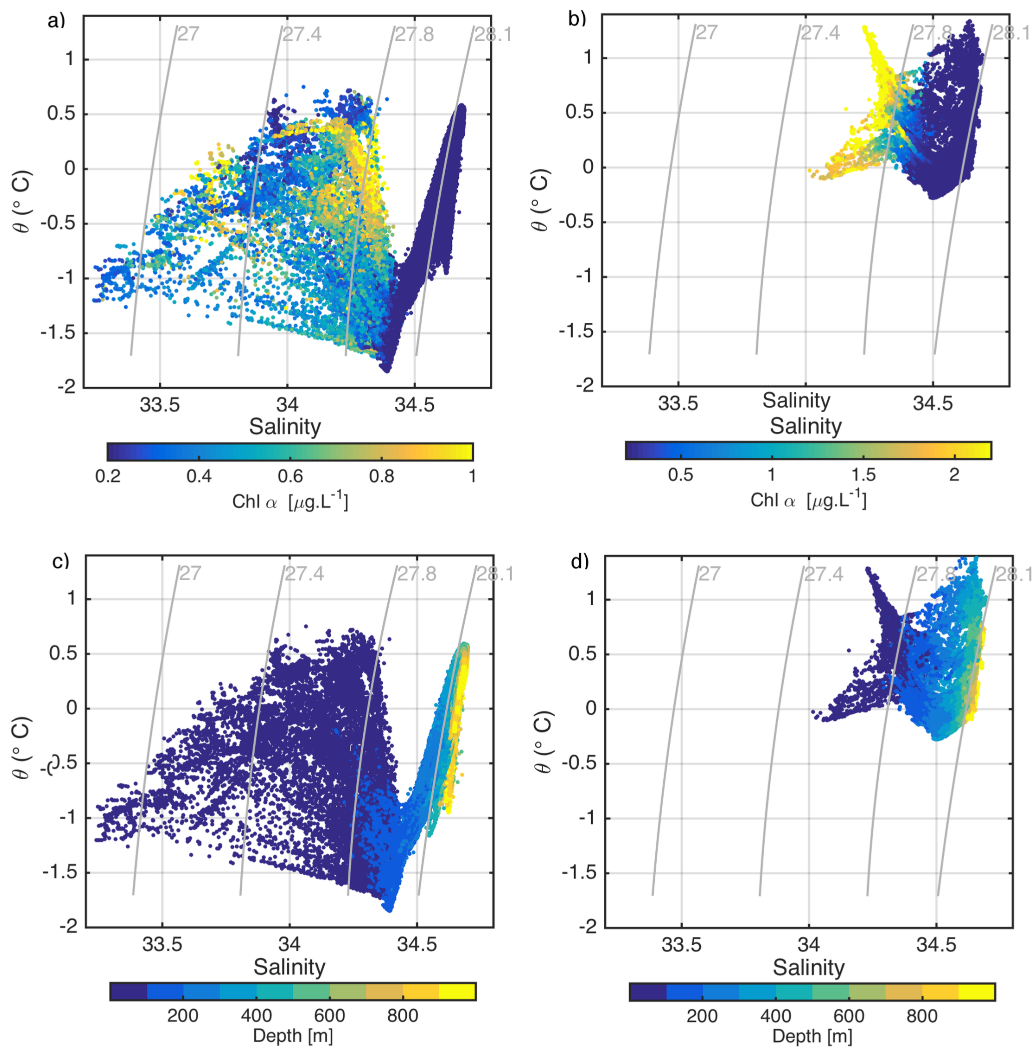

Figure 3.4: Potential temperature-Salinity diagrams for (a) all glider dives at the western Powell Basin and (b) in the Hesperides Trough coloured by chlorophyll (Chl α; μg L^{-1}). Panels (c) and (d) show the same data as (a) and (b), respectively, coloured by water depth (m).

3.4 Biological Distribution and the influence of physical processes

Chlorophyll *a* concentrations varied substantially through the field campaign (Fig. 3.2). The survey can be split into four different regions with respect to chlorophyll *a* distributions. We generally observe greater chlorophyll concentrations on-shelf than the regions directly off-shelf within the Powell Basin; we also observe systematically higher chlorophyll *a* concentrations over and north of the South Scotia Ridge, in the Hesperides Trough (glider sections 10-14 SG539), compared with the generally low chlorophyll *a* levels further south in the Powell Basin (glider sections 1-6 SG522 and 1-9 SG539; (Figs. 3.1 and 3.5). Regardless of the geographical area (i.e. Powell Basin or Hesperides Trough), chlorophyll values higher than 0.3 $\mu g L^{-1}$ are mostly found above the WW temperature minimum (27.95 $kg m^{-3}$ isopycnal), which is approximately at 120 m in the Powell Basin and deepens to approximately 220 m in the Hesperides Trough (Fig. 3.2). Based on this vertical distribution of chlorophyll *a*, we choose to use 200 m as the depth of vertical integration of chlorophyll *a* and POC concentrations (Fig. 3.5) to include the biological signatures from both regions.

In the western Powell Basin, chlorophyll *a* concentrations ranged from near 0 to 1 $\mu g L^{-1}$ (Fig. 3.2). Off-shelf, a diffuse deep chlorophyll maximum is mostly located in the Winter Water layer, contained within the 27.75 and 27.95 $kg m^{-3}$ isopycnals (between 70 and 130 m; Figs. 3.2 and 3.6). In contrast, in the upper slope region, where we see elevated chlorophyll *a* values, chlorophyll *a* is more evenly distributed within the surface mixed layer (0–100 m).

The on-shelf–off-shelf difference in chlorophyll *a* vertical distribution is not necessarily coincident with the classical definition of the ASF position (i.e. on-shore extent of 0°C isotherm). However, the cross-slope change in chlorophyll *a* distribution is generally coincident with a change in the stratification pattern of the surface waters. The change in the surface waters stratification is, ultimately, associated with the front and the on-shore downwelling of the shallow isopycnals (Fig. 3.6). The intensity of the buoyancy frequency (N^2) peak generally increases and is more pronounced off-shore, in agreement with the presence of CDW and a more pronounced Winter Water temperature minimum. This transition is mostly coincident with the subsurface frontal gradient of properties. The layer of highest stratification generally matches the 27.75 $kg m^{-3}$ isopycnal; the subsurface chlorophyll maximum then sits generally below the pycnocline in offshore areas. On the upper slope, higher chlorophyll *a* patches coincide with areas of relatively weaker stable stratification as indicated by the Turner angle (values between -45°and 45°; Fig. 3.6). Since potential vorticity (PV) in the region is largely controlled by the vertical buoyancy gradient, we observe an increase in PV towards offshore along the surface isopycnals due to convergence of the isopycnals, which may represent a dynamical barrier between these regions.

These observations represent late-summer conditions and thus the observed

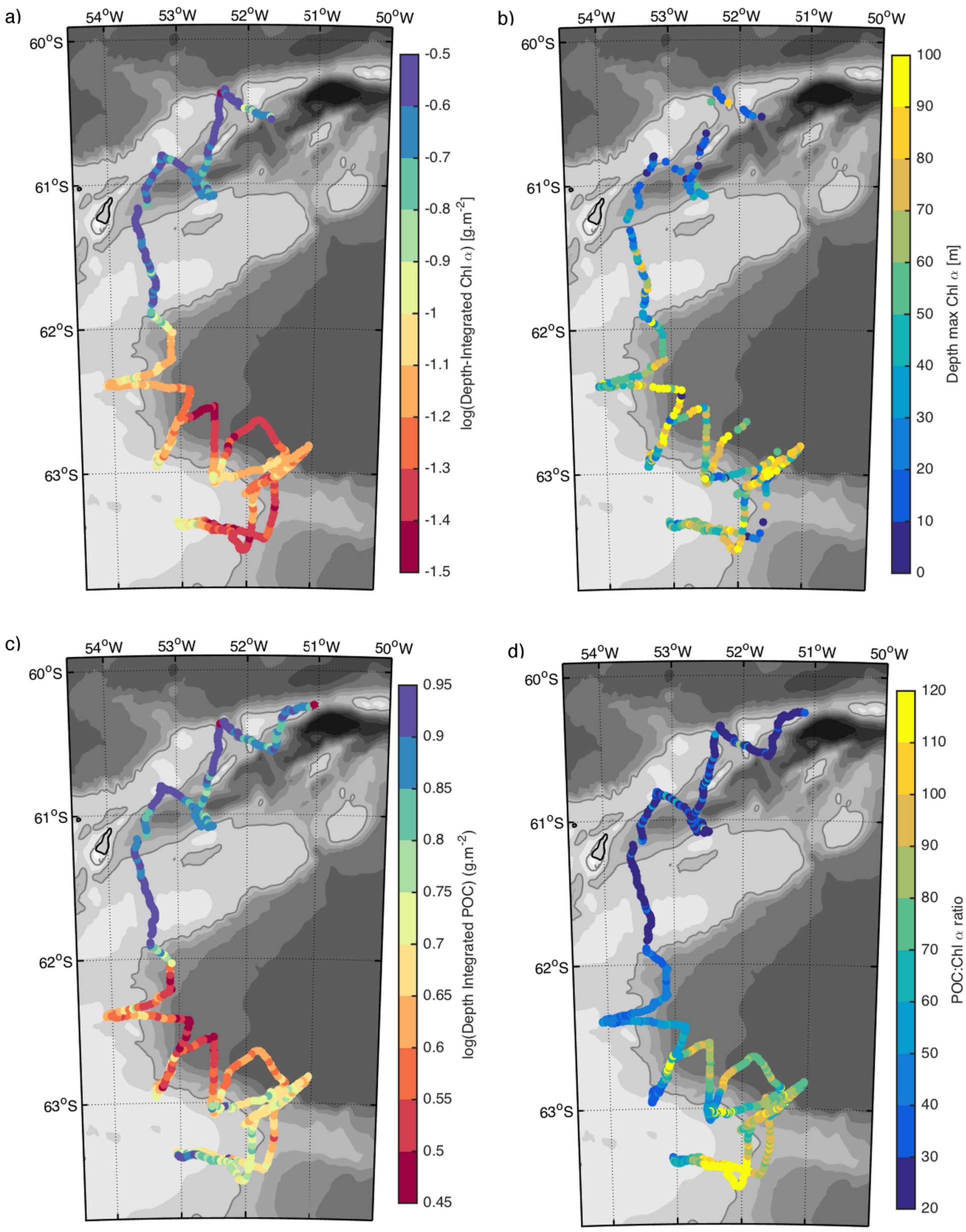

Figure 3.5: Maps of (a) depth-integrated chlorophyll *a* (0 – 200 m) (logarithmic scale, g m^{-2}), (b) depth of chlorophyll *a* maximum (m), (c) depth-integrated POC (0 – 200 m) (logarithmic scale, g m^{-2}), (d) average POC:chlorophyll ratio(0 – 100 m) from gliders. Grey line indicates 1000 m isobath.

deep chlorophyll maximum off-shelf is likely representative of post-bloom conditions with depleted surface nutrients and a deep chlorophyll maximum sustained by background mixing of nutrients at the nutricline, just below the pycnocline. Most of these observations are based on sections that cover the upper slope–off-shelf areas. In the southern and most shoreward sections (Sect. 1 from SG522 and

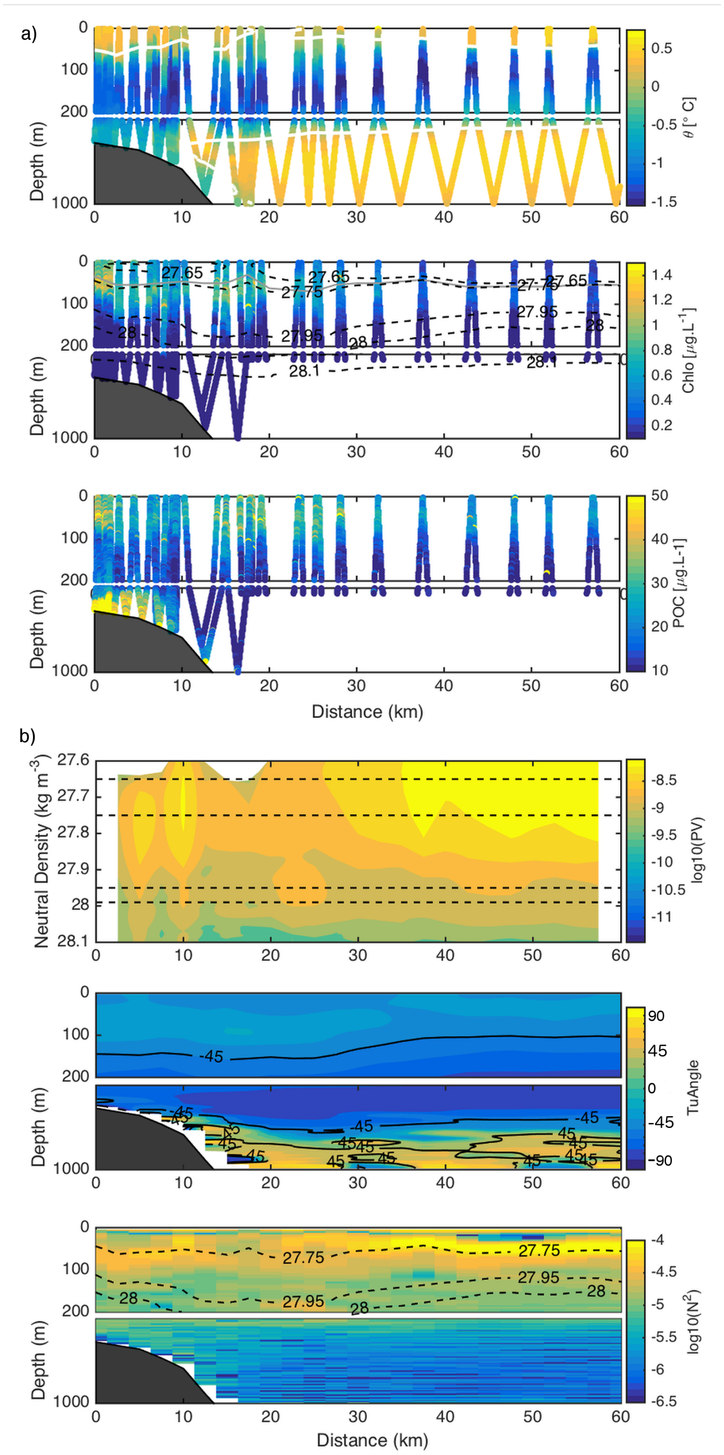

Figure 3.6: Section 6 from glider SG539 biological. (a) Potential temperature (θ; °C), chlorophyll a (Chl α; μgL^{-1}) and particulate organic carbon (POC; μgL^{-1}), (b) Potential vorticity (logarithmic scale) in neutral density coordinates (log10(PV); s^{-3}), Turner Angle (TuAngle) and vertical buoyancy gradient ($N^2; s^{-2}$). In panel (a), the white line indicates the 0°C isotherm. Dashed black lines indicate neutral density isopycnals. Grey line in panels indicate mixed layer depth.

SG539), the isopycnal that outcrops at the surface (27.65 $kg\,m^{-3}$), in an area of high productivity, deepens offshore, bounding the chlorophyll maximum (Fig. 3.2 and 3.6). This, together with the PV gradient (towards offshore) observed at this density layer, suggest that advective processes associated with eddy fluxes may play a role in setting the subsurface maximum off-shore by subduction of chlorophyll *a* and biomass along isopycnals, a process described by Erickson et al. (2016) at the western Antarctica Peninsula. However, there is not enough evidence to confirm or dismiss the contribution of this process for the remaining study area.

Even though in section 6 from SG539 (Fig. 3.6) there is a decrease in POC from on-shelf to off-shelf, this feature is not strongly consistent among all sections (Fig. 3.5). Maximum POC values are in the top few meters everywhere, not showing the subsurface maximum observed in chlorophyll in off-shelf areas (Fig. 3.5). Thus, there is no clear relationship between integrated POC and the front position.

Deeper in the water column, a strong POC signal below 300 m is observed over the bottom shelf and upper slope for most of the study region, particularly so in the SSR region (Figs. 3.2, 3.6 and 3.7). The thickness of this layer varies between 200-300 m and, in some locations, it presents POC values of 70 $\mu g\,L^{-1}$, higher than those is observed at the surface. This thick nepheloid layer may indicate that there is strong sediment resuspension in the area, which could potentially bring iron to the water column. This is in agreement with studies that show that, in the Atlantic sector of the Southern Ocean, the main source of dissolved iron is likely to be rich sediments from continental shelf, shallow plateau and islands (Ardelan et al., 2010; De Jong et al., 2012; Wadley et al., 2014). Multiple mechanisms can drive the upwelling of micro (specially iron) and macronutrients (eg. phosphate and nitrate), such as Ekman divergence, eddy motion and topographic interactions, which may work simultaneously: e.g. iron transported vertically to shallower depths by topographic upwelling can be supplied to the mixed layer by Ekman divergence (Sokolov and Rintoul, 2007). The particularly high POC values observed below 300 m over the west Powell Basin continental shelf and the shallow South Scotia Ridge seem to be bottom intensified and may be a consequence of stronger mixing near the seabed (average value of 84 ± 22 $\mu g\,L^{-1}$; Figs. 3.6 and 3.7). Enhanced mixing due to the interaction of the bottom intensified currents (Azaneu et al., 2017) with the rough and shallow bathymetry (Naveira Garabato et al., 2004) may contribute to resuspend sediments, bringing dissolved and particulate Fe in the water column. Tidal currents and internal wave propagation can also contribute to sediment resuspension (De Jong et al., 2012; Hosegood et al., 2004). The possible development of baroclinic instabilities at the boundary between the bottom dense layer and the layer above could facilitate the transfer of iron to shallower layers (Azaneu et al., 2017). Once in the water column, the organic material could be advected by the main flow along slope and possibly contribute to primary production in other regions. Moreover, the bottom boundary layer dynamics can potentially contribute to resuspend sediment by bottom stress and lead to a cross-slope downward transport of organic material (Simpson and McCandliss, 2013). In a study in the Celtic Sea shelf-break, (Porter et al., 2016) relate the inversion in the direction and strength of the along slope current with the onset of upwelling of deep nutrient rich waters, which would contribute to the spring bloom. Similarly, the Antarctic Slope Current (ASC) strength is variable in the western Antarctic Peninsula, with events of reverse in the direction of the along slope flow (Azaneu et al., 2017), which could also lead to periods of cross-slope upwelling flow at the bottom boundary layer.

In summary, shelf waters enriched by sediment-derived Fe (Ardelan et al., 2010), mixing and turbulence generated by the bottom intensified currents (Azaneu et al., 2017) may be factors contributing to the maintenance of high chlorophyll *a* concentration over the upper slope. This leads to higher depth-integrated chlorophyll values over the upper slope in comparison with offshore areas (Fig. 3.5), where a deeper and less pronounced subsurface chlorophyll *a* maximum sits below the stronger pycnocline.

In the western Powell Basin, in addition to relatively high chlorophyll *a* concentrations over the shelf associated with nutrient-rich shelf waters, enhanced local production also occurs due to the iceberg input of iron (Biddle et al., 2015; Duprat et al., 2016). In most sections, depth-integrated chlorophyll in off-shelf areas is mostly below 0.062 $\mathrm{g\,m^{-2}}$, while in sections 4-6 SG522 it is on average 0.078 $\mathrm{g\,m^{-2}}$ (Fig. 3.5). Surface waters in these sections are colder (θ between -1.2 – 0°C; Fig. 3.2), fresher (salinity between 33.3 – 33.8), more stratified and possibly richer in iron than in the neighbouring sections (θ between -0.2 – 0.5°C and salinity between 33.8 – 34) due to the influence of the sea ice melting. As well as chlorophyll *a*, POC is also enhanced in these sections, although it is not possible to associate it directly with the

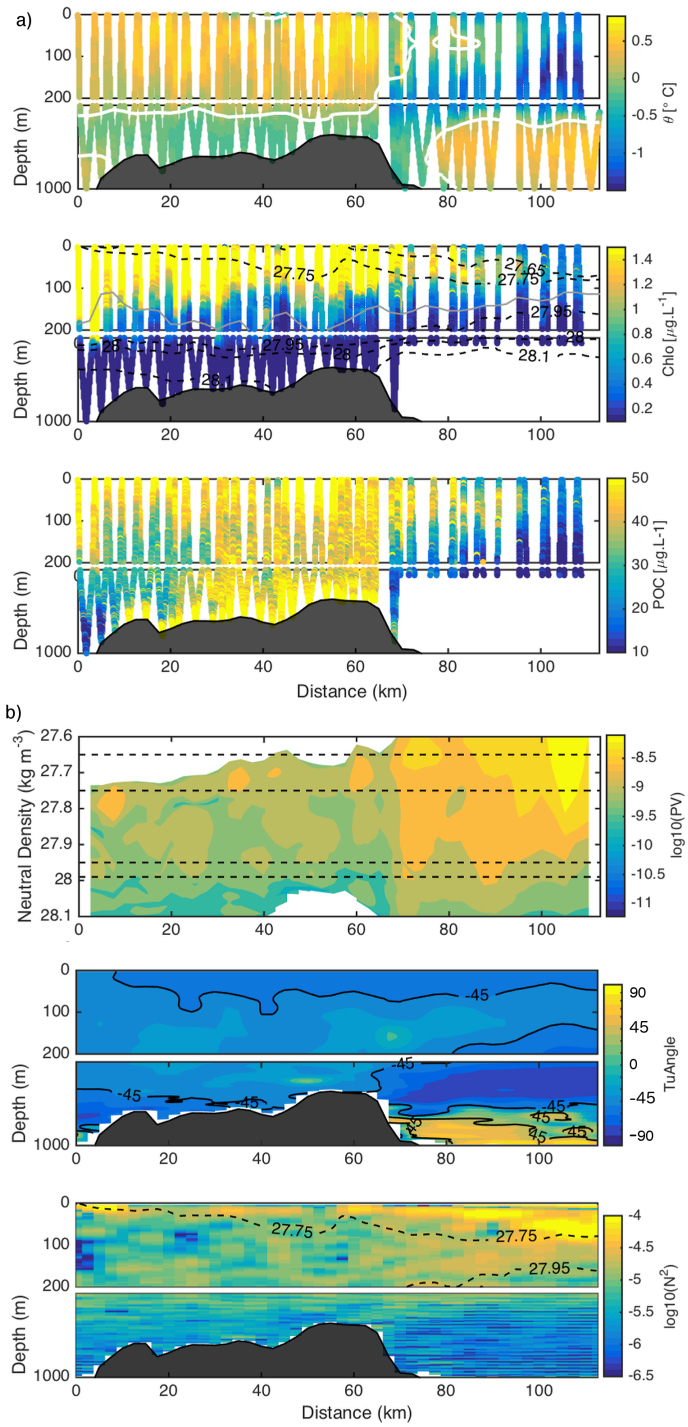

Figure 3.7: Section 10 from glider SG539 biological and physical properties. (a) Potential temperature (θ; °C), chlorophyll a (Chl α; μgL^{-1}) and particulate organic carbon (POC; μgL^{-1}), (b) Potential vorticity (logarithmic scale) in neutral density coordinates (log10(PV); s^{-3}), Turner Angle (TuAngle) and vertical buoyancy gradient ($N^2; s^{-2}$). In panel (a), the white line indicates the 0°C isotherm. Dashed black lines indicate neutral density isopycnals. Gray line in panels indicate mixed layer depth.

iceberg presence since all sections over the Joinville Ridge present higher POC values than the remaining sections within the Powell Basin. Biddle et al. (2015) showed that the local biological production at these sections were affected by the passage of a large iceberg, possibly through local micronutrient injection.

In addition to the cross-slope differences in the chlorophyll *a* concentration and distribution in the water column, we observe a clear difference between sections over and north of the South Scotia Ridge, in the Hesperides Trough (glider sections 10 – 14 SG539), and sections further south in the Powell Basin (glider sections 1 – 6 SG522 and 1 – 9 SG539; Figs. 3.1 and 3.5). Section 10 (Fig. 3.7) partially captures the transition between the two distinct oceanographic conditions. In Hesperides Trough, there are significantly higher chlorophyll *a* concentrations ($> 2\ \mu g\,L^{-1}$) and, unlike the Powell Basin, the chlorophyll *a* signal is not constrained to a relatively shallow surface mixed layer or a deep chlorophyll maximum. Rather, it is present from the surface to approximately 150 m, with greater concentrations within the top ~ 130 m (Figs. 3.2 and 3.4). In Hesperides Trough, higher chlorophyll concentrations ($> 2.2\ \mu g\,L^{-1}$) are found over the shelf, associated with warmer surface waters (> 0.5 °C), while within the trough, surface waters present chlorophyll values mostly between 1.5 and 2.2 $\mu g\,L^{-1}$ and temperatures below 0.5 °C (Figs. 3.2 and 3.4). POC follows a similar pattern of increased concentration and thickness of high POC layer at Hesperides Trough, where maximum POC concentrations at the surface are coincident with maximum chlorophyll values. Unlike the chlorophyll distribution, the depth of maximum POC concentration is not very variable, being mostly at the surface in both regions. The difference in the biological distribution between Powell Basin and Hesperides Trough is easily observed in the depth-integrated chlorophyll and POC maps (Figs. 3.5). The average depth-integrated chlorophyll *a* and POC concentrations is 0.25 $g\,m^{-2}$ and 7.79 $g\,m^{-2}$ in Hesperides Trough, in comparison with 0.06 $g\,m^{-2}$ and 5.21 0.06$g\,m^{-2}$ found in Powell Basin. This difference is greater than one should expect due to temporal fluctuations of production, and is markedly coincident with the glider transition to the shallower South Scotia Ridge.

In the Hesperides Trough region, elevated chlorophyll concentrations are concurrent with warmer waters (Figs. 3.4 and 3.2); however warm water is present down to depths greater than 300 m (for example at the ends of sections 11 and 13) while the biological signatures are constrained to the surface ~ 130 m, indicating that the elevated chlorophyll *a* signal visible between the surface mixed layer and 130 m is not a result of downward mixing of a surface chlorophyll bloom but rather that production occurs down to 130 m. Along section 10, which crosses from Powell Basin to Hesperides Trough over South Scotia Ridge, POC values as high as 45 $\mu g\,L^{-1}$ are observed from the surface down to below 300 m. Elevated values observed in POC below 200 m, which are not concurrent with elevated chlorophyll *a*, likely originate from suspended sediment in this shallow region (shallower than 500 m), rather than a continuation of the surface POC.

The Powell Basin and Hesperides Trough present very different hydrographic characteristics which explain the markedly different chlorophyll *a* and POC regimes. The relatively low chlorophyll values in the western Powell Basin area are coincident with a more strongly stratified water column and the presence of Winter Water (Figs. 3.2 and 3.5); while in Hesperides Trough the high chlorophyll concentrations are coincident with the low surface stratification characteristic of Weddell-Scotia Confluence waters (Whitworth et al., 1994). The more homogeneous subsurface waters within the trough are a result of the erosion of relatively cold and fresh WW core by mixing with WDW (Palmer et al., 2012). In the proximity of Elephant Island and South Shetland Islands, it is believed that the main driver of the high chlorophyll *a* concentrations is the horizontal mixing between nutrient-rich Weddell Sea shelf waters and well-stratified AASW from the ACC in Drake Passage ACC (Hewes et al., 2008). In turn, the productivity at the north-east coast of the Antarctic Peninsula is sustained by sedimentary sources of iron (Wadley et al., 2014). This is consistent with the thick bottom layer of enhanced POC concentrations over the shelf and upper slope. It is possible that the iron introduced in the upper water column by the interaction of the flow with the bathymetry is advected with the flow, contributing with the higher productivity observed over the ridge and within the Hesperides Trough (De Jong et al., 2012; Annett et al., 2015).

The carbon to chlorophyll (POC:Chl) ratio was averaged in the top 100 m to restrict the calculation to the relatively uniform surface layer of enhanced POC values. The ratio follows the inverse distribution of the integrated chlorophyll *a* (Fig. 3.5). It decreases from an average value of 70 over Joinville Ridge, in the southern portion of Powell Basin, to 27.4 in Hesperides Tough. Within the Powell Basin, POC:Chl ratio in the northern portion of Powell Basin (sections 8 – 10) is lower than sections over

Joinville Ridge, associated with relatively higher chlorophyll and particularly lower POC concentrations (Figs. 3.2 and 3.5). Furthermore, there is an upper slope–off-shelf increase in the POC:Chl ratio in the Powell Basin sections. The higher POC:Chl ratios at the off-shore portion of the sections over Joinville Ridge than with on-shelf areas and the Hesperides trough area can indicate a lower contribution of phytoplankton to particulate carbon. This possibly suggests greater Fe limitation in the off-shore region due to the importance of this nutrient for the chlorophyll photosystem within phytoplankton cells. This is consistent with previous suggestion that the warmer waters within the Hesperides Trough are not iron depleted, allowing for very low POC:Chl ratios (Wadley et al., 2014).

Spatial changes in POC:Chl ratios may also indicate the dominance of distinct phytoplankton groups. In the Southern Ocean, phytoplankton blooms in regions such oceanic fronts and marginal ice zones are generally dominated by diatoms or haptophytes (e.g. *Phaeocystis Antarctica;* Prézelin et al., 2000). In regions such as the Ross Sea, lower POC:Chl ratios are generally associated with *P. antarctica* during late summer (DiTullio and Smith, 1996; Smith, Walker O. et al., 2000), which is more tolerant of a deeply mixed and low-light environment than diatoms (Arrigo, 1999; Moisan and Mitchell, 1999). In the north-western Weddell Sea, however, this flagellate has been reported in very low biomass and shallow mixed layer conditions of off-shore areas (Mendes et al., 2012). Using data from two summer cruises (2008 and 2009), Mendes et al. (2012) describe a coastal–offshore succession in the phytoplankton community composition associated with a horizontal gradient in the water stability. In more coastal areas (further onshore of our sampling area), diatoms were dominant in the well-mixed water column, associated with higher biomass. These were replaced by cryptophytes at the proximity of the upper slope area, where the stratification was intermediate and, in the off-shore strongly-stratified water, the low biomass was associated with the dominance of *P. Antarctica*. This is consistent with the upper slope–off-shore gradient in stratification, chlorophyll *a* distribution and POC:Chl observed in our study. Identification of distinct phytoplankton groups is beyond the scope of this work. However, the environmental conditions suggest that an on-shore–off-shore succession of phytoplankton community similar to that described by Mendes et al. (2012) could be present during our cruise. The possible dominance of cryptophytes over diatoms at the upper slope area may influence the trophic web as they as not as efficiently grazed by Antarctic krill (Moline et al., 2004).

As high biomass regions are considered critical feeding sites for higher trophic levels, it was expected that the location of these regions had some influence on the distribution of krill biomass. However, despite the lower chlorophyll *a* concentration, krill density is higher in the southern sampled area, over Joinville Ridge, than in the single transect across South Scotia Ridge (Fig. 3.8). The higher krill density around Joinville Ridge than at the northern section may be associated with the proximity of that area with the sea ice edge (Fig. 3.1). The local krill aggregation around the ridge could have contributed to the relatively high POC concentration observed in the region. Around Joinville Ridge, the krill distribution is patchy and does not show clear differences between onshore and offshore areas, nor a correlation with temperature or chlorophyll *a* concentration (Fig. 3.8). Krill shows, however, higher densities where the surface currents converge over shelf and slope areas. The influence of the circulation can also be the reason for the modest increase in krill density (in comparison with the surrounding regime) over a local rise in the bottom topography at the western edge of South Scotia Ridge. In this area, currents from ship current meters indicate the presence of an anticyclonic eddy (Fig. 3.9), which is a consistent feature previously reported in drifter studies (Thompson et al., 2009). The colder temperature in the centre of the eddy is coincident with lower chlorophyll *a* and a modest increase in krill density in comparison with its surrounding, which could have been trapped within its core, leading to intense grazing.

3.4.1 FINAL CONSIDERATIONS

During the almost 2 months of data collection, the ship and the gliders sampled distinct hydrographic regions, with different water masses and biomass distribution. The results show two distinct physical and biological scenarios at the western Powell Basin, onshore and offshore the front position, which are likely disassociated from each other. Over the upper slope, the weak stratification of surface waters and the nutrient input from shelf waters contribute to the shallow high chlorophyll concentrations. Offshore, the erosion of the surface chlorophyll *a* maximum and appearance of a subsurface maximum is in agreement with summer-like conditions, a stronger pycnocline and phytoplankton passive sinking. The two most on-

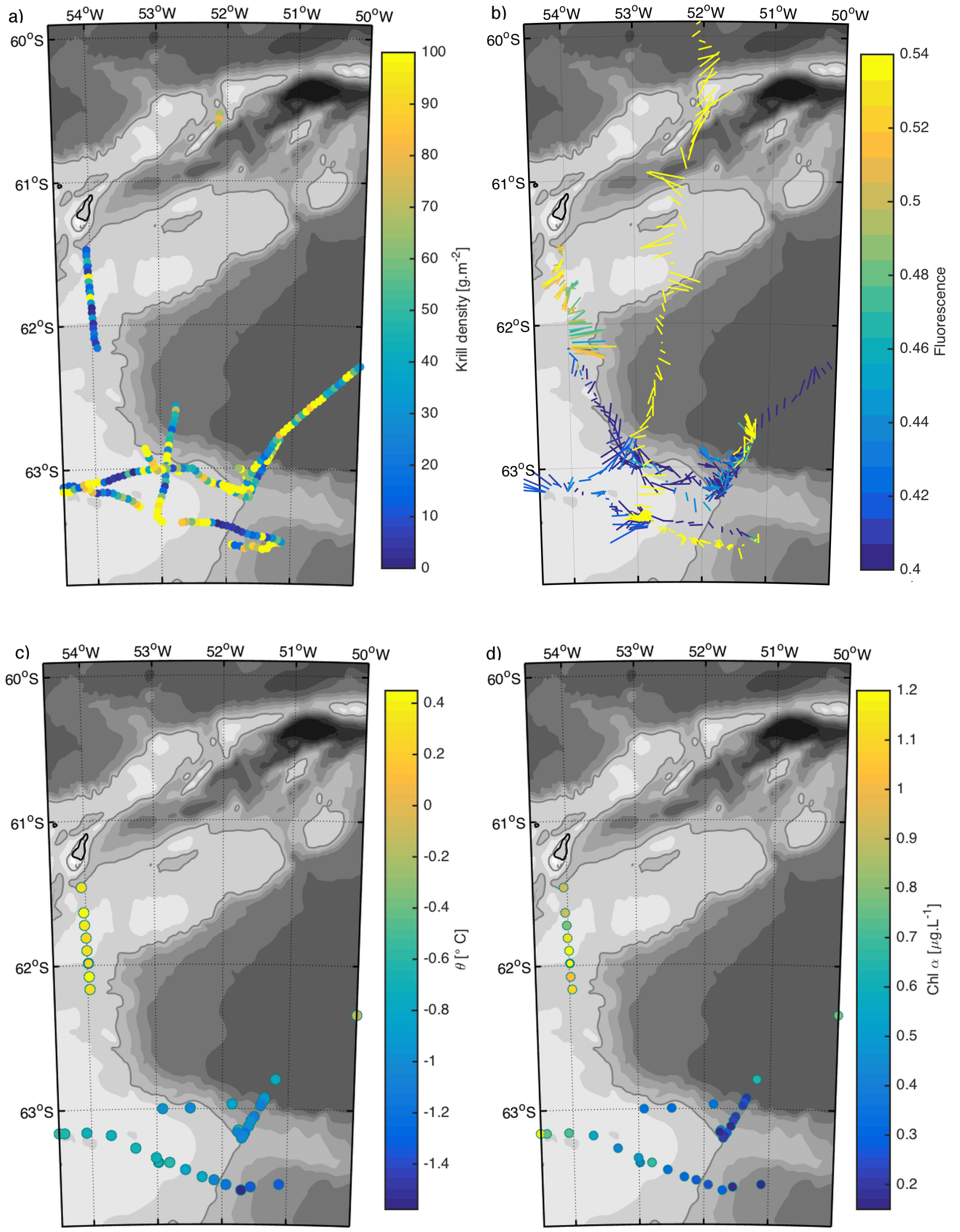

Figure 3.8: Map of (a) krill biomass (integrated 0 – 500 m) averaged in every 4 km (only data collected between 7 – 19h), (b) current direction from de-tided SADCP (averaged in depth 0 – 200 m) colored by fluorescence from thermosalinograph, (c) Potential temperature (θ; °C) and (d) chlorophyll a (Chl α; μgL^{-1}) from CTD stations (averaged in depth 0 – 200 m).

shore sections suggest that advective processes could potentially contribute to the deepening and formation of the subsurface maximum off-shelf, but there is not enough evidence to confirm this hypothesis. The results show no evidence of the frontal structure generating enhanced productivity locally. Rather, the frontal system

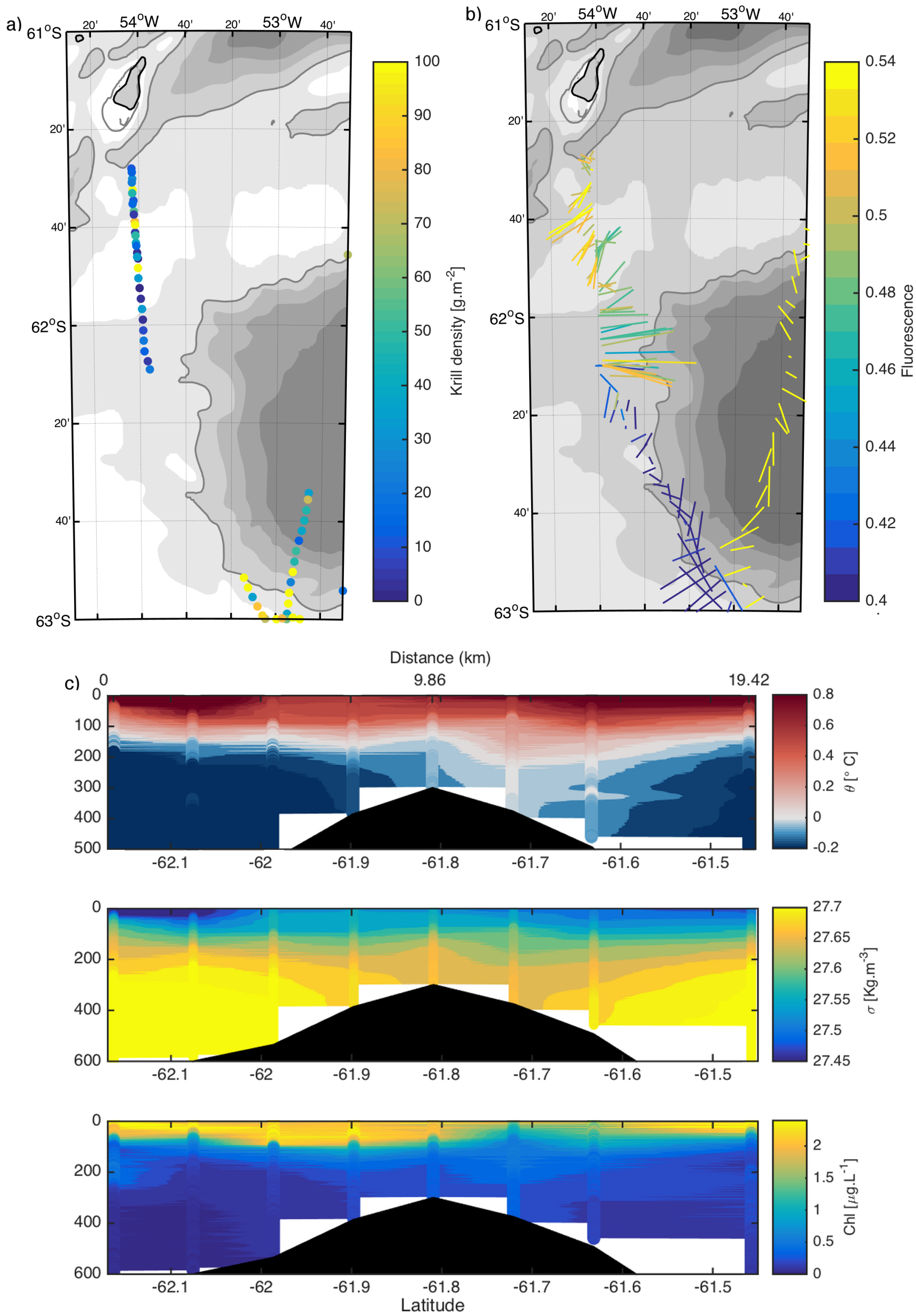

Figure 3.9: Map of (a) krill biomass (integrated 0 – 500 m) averaged in every 4 km (only data collected between 7 – 19h zoomed around the eddy over South Scotia Ridge, (b) current direction from de-tided SADCP (averaged in depth 0 – 200 m) colored by fluorescence from thermosalinograph, (c) Potential temperature (θ; °C), potential density (σ; $\text{kg}\,\text{m}^{-3}$) and (d) chlorophyll *a* (Chl a; $\mu\text{g}\,\text{L}^{-1}$) CTD section over eddy.

contributes to the formation of two hydrographic and biological distinct regions. The integrated POC content is not markedly influenced by the front. There is, however, a distinct nepheloid layer above the upper slope that becomes particularly thick (~ 300 m) above the South Scotia Ridge, which agrees with studies that suggest the sediment as an important iron source for coastal Antarctic Peninsula productivity (e.g. Ardelan et al., 2010; De Jong et al., 2012; Wadley et al., 2014). The resuspension and transport of sediments by bottom intensified currents, enhanced mixing from rough bathymetry, mixing of Weddell shelf waters and surface waters from ACC, and advection of eddies caring nutrient-rich waters may contribute to the high productivity in the Hesperides trough region, which is mostly associated with warmer waters. The POC:Chl ratio is also very distinct between Hesperides trough and western Powell Basin regions, being lower in the former. Within the Powell Basin, the POC:Chl ratio shows an upper slope–off-shore gradient that suggests a change in phytoplankton community. Despite that, krill biomass distribution does not show any clear association with temperature or chlorophyll *a* concentration, being mostly affected by the circulation and convergence of the flow. Our understanding of krill distribution and processes influencing it is limited by the low availability of simultaneous biological and physical sampling. The use of gliders equipped not only with fluorescence and backscatter sensors, but also echosounders, could have provided a more comprehensive view of the biological and physical processes influencing the local krill community.

4

INFLUENCE OF SHELF BREAK PROCESSES ON THE TEMPERATURE TRANSPORT ONTO THE EASTERN AMUNDSEN SEA CONTINENTAL SHELF

This chapter is presented as a draft paper.

Azaneu, M., Webber B., Assmann K., Abrahamsen, P., in prep.

M. V. C. Azaneu carried out the research and prepared the paper. KJH and BW provided feedback on earlier drafts.

4.1 INTRODUCTION

Ocean-induced basal melting is believed to be the main cause of the observed thinning and grounding line retreat of glaciers draining the Amundsen Sea sector during the last two decades (1992-2011; Jenkins et al., 2010; Rignot et al., 2014; Dutrieux, 2014; Paolo et al., 2015). Between 2010 and 2016, the West Antarctic Ice Sheet experienced 21.7% of its grounding line retreating, 59.4% if only the Amundsen Sea Sector is considered (Konrad et al., 2018). Pine Island and Thwaites Glaciers are two of the major ice streams flowing into the east Amundsen Sea embayment. Despite the past fast retreat, the ice discharge of Pine Island Glacier (PIG) has remained steady since 2009 (Mouginot et al., 2014), and its grounding line has stagnated recently partially due to relatively cold ocean conditions (Konrad et al., 2018). This recent cold period is also likely related to the lower melt rates estimated from recent datasets (2012,2014) in comparison with historical data (Dutrieux, 2014; Heywood et al., 2016). In contrast, Thwaites Glacier has increased its ice discharge considerably, overcompensating the stoppage of the acceleration of Pine Island Glacier (Mouginot et al., 2014).

Over the eastern Amundsen continental shelf, the depth of the permanent thermocline and the associated average temperature below the depth of the bottom of the ice shelf (350 m) are proxies for the amount of heat available within the sub-ice inner cavity for melting of the Pine Island ice shelf (Jenkins et al., 2010; Dutrieux, 2014). The onshore temperature flux is provided by Circumpolar Deep Water (CDW), which accesses the continental shelf mainly through the central (113°W) and eastern (102-108°W) troughs (Fig. 4.1), where this water mass fills the ocean layer below 400 m (Walker et al., 2007; Nakayama et al., 2013). The offshore CDW, which is characterised by a subsurface temperature maximum above 1.5°C, can be divided into upper CDW and lower CDW. The former is identified by the temperature maximum and oxygen minimum, and the latter by relatively lower temperatures and higher salinities (> 34.7)(Orsi et al., 1995; Walker et al., 2013). The depth of the central and eastern troughs is approximately 600 m (Fig. 4.1), which coincides roughly with the offshore transitional depth between the upper and lower CDW and thus allows the saltier lower CDW to be found within the central trough (Walker et al., 2013). The central and eastern troughs merge further on-shelf, allowing the inflow of both troughs to eventually mix and fill the deep Pine Island Bay (Jacobs et al., 2011; Schodlok et al., 2012; Nakayama et al., 2013). The importance of the contribution of each trough is debated. While in situ data from summer 2012 show that the warmer CDW entering through the eastern trough contributes roughly two thirds to the mixture that reaches the inner continental shelf (Nakayama et al., 2013), a modeling study suggests that a recirculation within the central trough, associated with bathymetric sills, could determine the access of the warm waters further south (Assmann et al., 2013). After intruding onto the continental shelf, CDW is modified by mixing with colder surface waters and then is referred as Modified CDW (mCDW) ($\gamma_n > 28.03$; Whitworth et al., 1998; Arneborg et al., 2012). Closer to the shelf break, Walker et al. (2013) suggest that the warm waters filling the trough likely result from the mixture of offshore lower and upper CDW, rather than mixing between lower CDW and Antarctic Surface Water (AASW) over the slope.

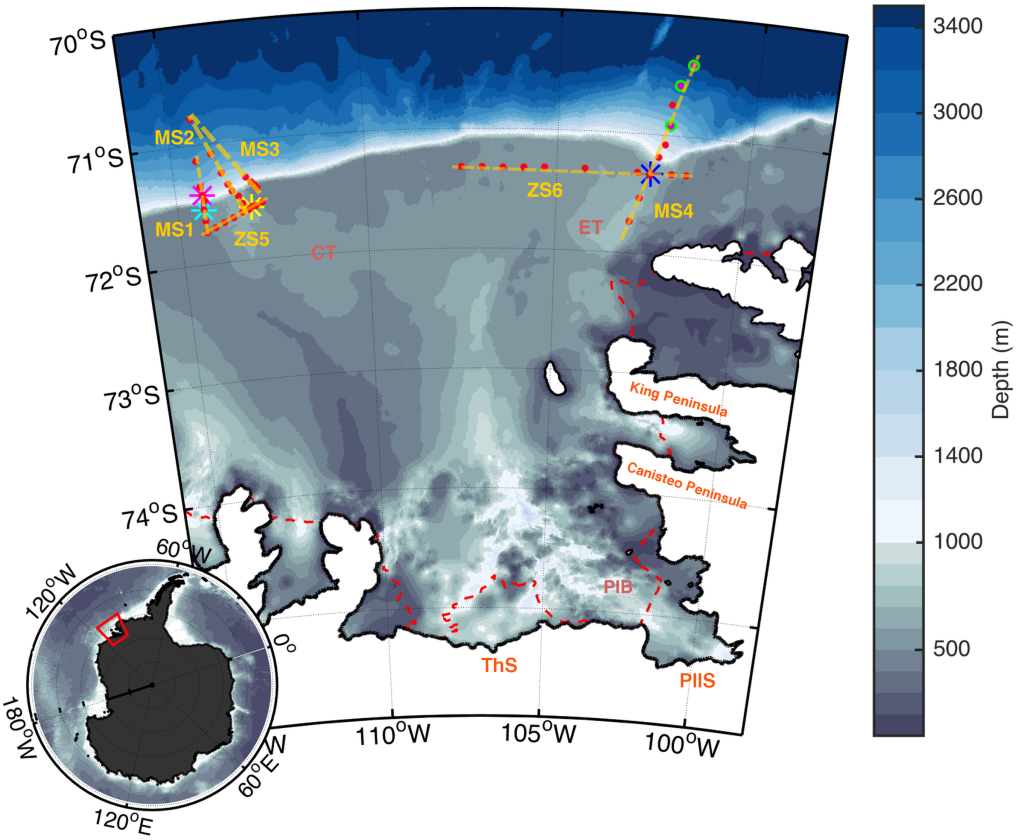

Figure 4.1: a) Map of study area; IBCSO bathymetry (shaded) and ice shelf edges from 2004 (Haran et al., 2005). Thwaites Glacier (ThS), Pine Island Ice Shelf (PIIS), Pine Island Bay (PIB), central (CT), eastern (ET) Pine Island troughs. Red dots represent CTD/LADCP stations; Yellow, light blue, magenta and dark blue stars indicate the location of moorings M1/M11/M12, M4, M5 and M20. Green dots indicate the position of stations 1, 2 and 4 (from north to south). The position of meridional sections MS1, MS2, MS3 and MS4 and zonal sections ZS5 and SZS5 are indicated by yellow dashed lines. Inserted map shows Antarctic map and the location of study area.

The along slope current system in the eastern Amundsen Sea involves a westward geostrophic flow at the surface (Antarctic Slope Current), and a strong eastward undercurrent (Heywood et al., 1998; Chavanne et al., 2010) that has been previously sampled by Walker et al. (2013) and successfully represented by modeling studies (e.g. Assmann et al., 2013; Kimura et al., 2017). Such an undercurrent may arise in a situation of a downwelling system associated with the easterlies driving the westward surface slope current, and set up initially by coastal-trapped waves (Chavanne et al., 2010). The interaction of the eastward geostrophic undercurrent with the shelf break troughs would facilitate the access of CDW to the continental shelf, providing a persistent south-eastward baroclinic flow of warm waters (St-Laurent et al., 2013; Assmann et al., 2013). Among the processes that are suggested to explain the onshore transport of warm waters through the troughs are topographic steering and the development of a dominant cyclonic flow from vortex stretching, the development and cyclonic propagation of topographic waves (St-Laurent et al., 2013), and upslope transport in the bottom Ekman layer (Wåhlin et al., 2012).

The hydrographic conditions within the Amundsen Sea vary seasonally (Thoma et al., 2008; Kim et al., 2017; Mallett et al., 2018) and interannually (Dutrieux, 2014; Jacobs et al., 2011; Steig et al., 2012; Webber et al., 2017). For example, anomalous ocean conditions were observed in the Pine Island Bay during 2012, characterized by deeper thermocline and a reduction in the available heat reaching the PIG calving front (Webber et al., 2017). Changes in the local wind forcing associated with atmospheric anomalies originating in the central tropical Pacific are suggested by some studies (Dutrieux, 2014; Jenkins et al., 2016) as the main factor that led to this cold period, and the main cause of the on-shelf variability on decadal time scales.

The pattern of winds at the continental shelf break is a result of multi-scale atmosphere-ocean interactions, both local and remotely (Steig et al., 2012; Dutrieux, 2014), and affect ocean conditions on different time scales. The winds will affect the CDW input onto the shelf, the coastal downwelling and surface buoyancy fluxes, which ultimately will determine the depth of the thermocline over the continental shelf (Thoma et al., 2008; St-Laurent et al., 2015; Kim et al., 2016; Jenkins et al., 2016). Thus, the impact of the ocean circulation and local winds at the shelf break on the ocean conditions close to the Pine Island ice shelf is not straightforward; local atmospheric forcing within the Pine Island Bay strongly modulates the ocean at depths critical for melting of the ice shelf (St-Laurent et al., 2015; Webber et al., 2017). Furthermore, changes in the temperature transport at the shelf break is likely to have an asymmetric impact on the PIG ice shelf (Kimura et al., 2017).

Despite the complex processes occurring over the continental shelf that affect the ocean conditions, the variability of the CDW flow onto the continental shelf still remains as an important factor in determining the amount of heat available within the Amundsen Sea embayment. The CDW inflow variability is also an important component connecting the non-local climate forcing with the conditions found over the continental shelf (Thoma et al., 2008) and therefore needs to be fully investigated. Besides winds, other factors, such as sea-ice coverage and its impact on the transmission of stress from the atmosphere to the ocean surface, can influence the variability of the CDW on-shelf flow (Kim et al., 2017). It is suggested that, within the western (Dotson) trough, seasonal variation in thickness and temperature of the warm layer is induced by CDW being pushed across the shelf break by ice-modulated Ekman pumping (Kim et al., 2017). A recent study shows a thicker CDW layer in winter than in summer using in situ data from 2014 (Mallett et al., 2018). In addition to surface forcing, the ocean circulation dynamics related to the direction and strength of the undercurrent may impact the on-shelf temperature transport on time scales shorter than those associated with large-scale atmospheric forcing (Assmann et al., 2013; St-Laurent et al., 2013).

In this study, we analyse observations from six moorings and from ship-based hydrographic sections at the shelf break in the Amundsen Sea to investigate shelf break processes, including the slope current system, and its influence on the variability of the temperature transport onto the eastern Amundsen Sea continental shelf. The dataset and calculations used here are presented in section 4.2. In section 4.3.1, we describe the hydrographic setting based on the Ocean2Ice cruise data. Section 4.3.2 presents a snapshot of the mass and temperature transports estimated from hydrographic sections sampled during the early 2014 research cruise. To set these values in context, section 4.3.3 presents temperature transport calculations from moored time series. The variability of the along- and across-slope flows is discussed based on mooring records of current velocity, temperature and salinity at the shelf break using wavelet analysis.

4.2 METHODOLOGY

The dataset used in this study is part of the iSTAR project (Stability of the West Antarctic Ice Sheet). The iSTAR research cruise took place in February-March 2014, during which 102 CTD stations were occupied together with current velocity from lowered acoustic Doppler current profiler (LADCP; Figs. 4.1 and 4.2). In this study we use 52 CTD/LADCP stations collected at the shelf-break and continental slope area, with which we define 6 hydrographic sections (cross-slope, quasi-meridional sections MS4, MS1, MS2 and MS3, and cross-trough, quasi-zonal sections ZS5 and ZS6; Fig. 4.1). In addition, we use data from 6 moorings deployed at the shelf-break (M5) and in the central (M1/M12, M4 and M11) and eastern (M20) troughs of the eastern Amundsen continental shelf (Fig. 4.1, table **??**). Moorings M1 and M12 are co-located, while M11 is 1.55 km distant from those; for some of the analysis we take moorings M1 and M12 as a single ~ 4 year time series, and we compare it in time with M11.

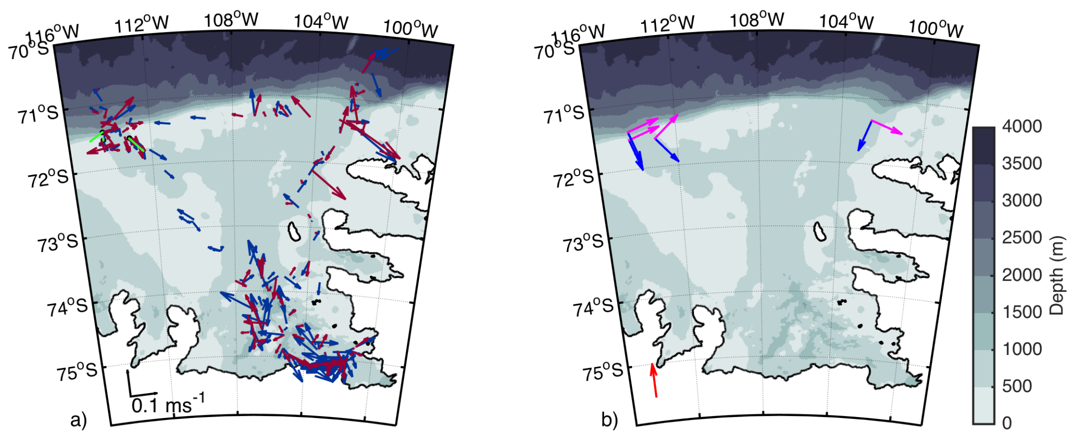

Figure 4.2: a) De-tided Current observations in the Amundsen Sea. Purple arrows show LADCP velocities (300−700 m average). Blue arrows represent velocities from SADCP (300−700 m average, sub sampled every 3.6 hours). Green arrows indicate velocity from moorings' current meters (at approximately 450 m) averaged for the cruise period (30/01/14 to 05/03/14). IBCSO bathymetry (shaded) and ice shelf edges from 2004; b) Rotated axes for moorings velocities. Blue indicates the along-trough axis and pink the along-slope axis.

Based on the harmonic analysis of the 2 years of velocity records from the moorings, we identified the semidiurnal and diurnal tides as the main tidal constituents in the region. The former is relatively more important at the offshore mooring (M5), while the latter makes a greater contribution over the continental shelf (moorings M1, M4, and N20). Using the main tidal constituents identified by the harmonic analysis, we then estimated the tidal current velocities using two independent methods: (i) extracting the velocities from the barotropic CATS model (10 km resolution; Padman et al., 2002) and (ii) empirically deriving the tidal velocities

Mooring	Sampling Period	Position	Local Depth (m)	Instrument	Depth (m)	MAB	Variables Measured
M1	06/03/12 to 02/03/14	71°S 33.7';	605	AQL	345	263	T,P
		113°W 02.7'		AQL	370	234	T,P
				AQL	400	205	T,P
				AQL	429	176	T,P
				AQL	458	146	T,P
				ADCP	490	115	T,U,V,P
				SBE-37	487	117	T,S,P
				AQL	517	88	T,P
				AQL	550	55	T,P
				AQD	581	23	T,U,V,P
				SBE-37	582	22	T,S,P
M11	12/02/09 to 07/01/11	71°S 34.2';	611	SBE-39	450	161	T,P
		113°W 02.4'		SBE-39	503	108	T,P
				AQD	555	56	T,U,V,P
				SBE-37	580	31	T,S,P
M12	02/03/14 to 07/02/16	71°S 33.7';	605	AQL	332	272	T,P
		113°W 02.7'		AQL	380	224	T,P
				AQD	423	182	T,U,V,P
				SBE-37	426	178	T,S,P
				AQL	447	127	T,P
				AQL	528	77	T,P
				AQD	554	50	T,U,V,P
				SBE-37	555	50	T,S,P
M4	05/03/12 to 28/02/14	71°S 32.7';	513	SBE-37	361	152	T,S,P
		114°W 18.2'		AQL	398	115	T,P
				AQL	435	78	T,P
				AQL	469	43	T,P
				AQD	485	27	T,U,V,P
				SBE-37	487	26	T,S,P
M5	05/03/12 to 28/02/14	71°S 25.4';	1465	AQL	309	1156	T,P
		114°W 18.9'		AQL	353	1111	T,P
				AQD	399	1066	T,U,V,P
				SBE-37	400	1064	T,S,P
				AQL	453	1011	T,P
				AQL	506	958	T,P
				AQD	558	906	T,U,V,P
				SBE-37	560	905	T,S,P
				AQL	613	852	T,P
				AQL	666	799	T,P
				AQD	718	747	T,U,V,P
				SBE-37	719	745	T,S,P
M20	04/03/14 to 04/02/16	71°S 19.7';	634	AQL	378	255	T,P
		102°W 33.0'		AQL	423	210	T,P
				AQD	467	166	T,U,V,P
				SBE-37	468	165	T,S,P
				AQL	518	115	T,P
				AQL	569	65	T,P
				AQD	595	39	T,U,V,P
				SBE-37	596	38	T,S,P

Table 4.1: Summary of instruments used in this study, their depths and sampling period at each of the moorings. MAB is meters above bottom, T is temperature, S is salinity, U is zonal velocity component (positive eastward), V is meridional velocity component (positive northward), and P is pressure. AQD stands for Nortek Aquadopp current meter, SBE for Seabird Electronics microcats, and AQL for Aquatec Aqualogger logers.

from the mooring time series using the "UTide Matlab" toolbox (Fig. 4.3). The tidal current velocities derived from moorings are typically below $0.03\,\mathrm{m\,s^{-1}}$. The model generally underestimates the tide velocities over the continental shelf, possibly because the model bathymetry overestimates the local depth, in comparison with IBCSO (Arndt et al., 2013). In some cases, the model is also out of phase with the empirically derived tides. Thus, it was opted to de-tide the SADCP and LADCP velocities using the empirically derived tides, for which M5 derived tides were used to de-tide measurements taken offshore of the 1000 m isobath; and M1 and M20 for measurements over the continental shelf within the central and eastern trough, respectively (Fig. 4.2a).

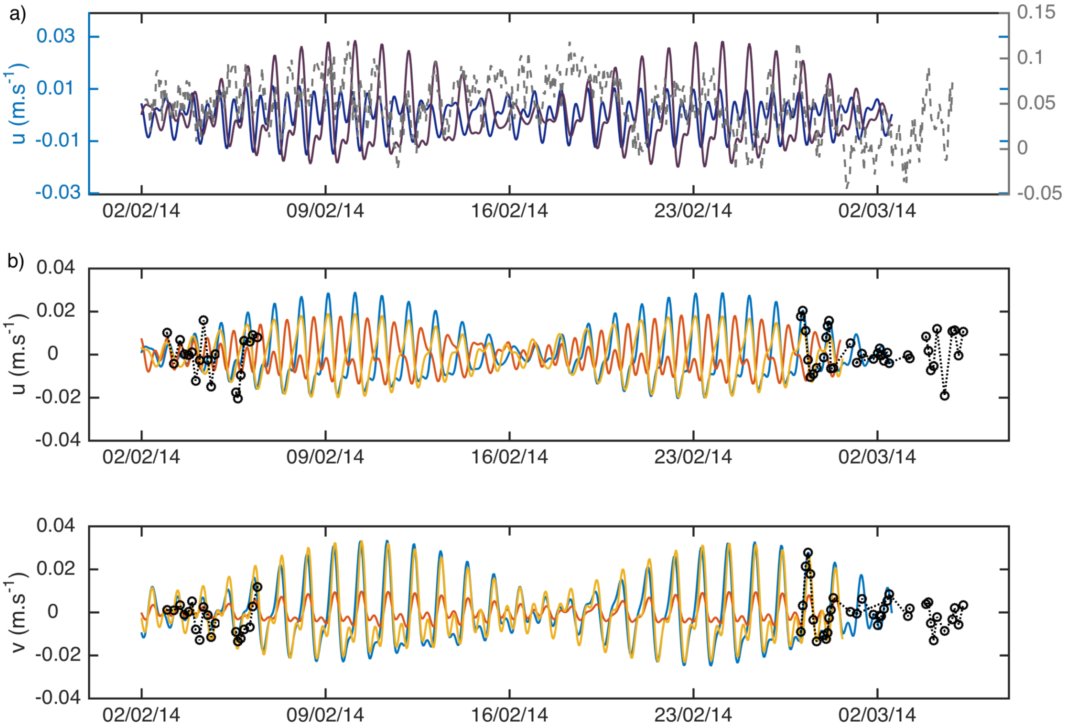

Figure 4.3: a) Zonal (u; m s^{-1}) tide velocities derived from CATS model (blue) and from current meter at mooring MS4 (purple) for the cruise period. Grey line show the original velocity data m s^{-1}) at 581 m. b) Example of zonal (u) and meridional (v) tide components (m s^{-1}) from MS4 (blue), MS3 (yellow) and M5 (red). Black circles indicate the tidal currents derived for the hydrographic sections (Fig. 4.1).

Baroclinic shear was calculated for the six hydrographic sections (Fig. 4.1). All variables were computed according to the International Thermodynamic Equation of Seawater-2010 (TEOS-10) framework (Trevor J. McDougall and Barker, 2011). In this region, for the water masses evaluated in this study, the difference between practical salinity and absolute salinity (S_A, g kg^{-1}) can be up to $\sim$ 0.2 g kg^{-1}, while potential temperature (θ) and conservative temperature (Θ, °C) are very similar. Thus we refer to θ only when comparing our results with previous studies. The referencing of the geostrophic shear was based on the average of the cross-section LADCP velocity profiles at the adjacent CTD stations. The vertical average velocity considered only the currents away 100 m from the ocean bottom and surface.

The CTD stations used in this study for calculation of geostrophic velocity were sampled when tides were weakest (Fig. 4.3). The average magnitude of the tidal currents derived for these stations is 0.01 m s^{-1}, which is small compared to the representative core velocity of the onshore flow (approximately 0.1 m s^{-1}). Thus, the de-tiding of LADCP and SADCP currents used to reference the geostrophic velocities had very little impact on the residual velocities of the sections. Despite that, de-tiding SADCP and LADCP data is advised to eliminate possible bias that the predominantly diurnal tides might induce over the short (< 12h) cross-trough sections (Assmann et al., 2013).

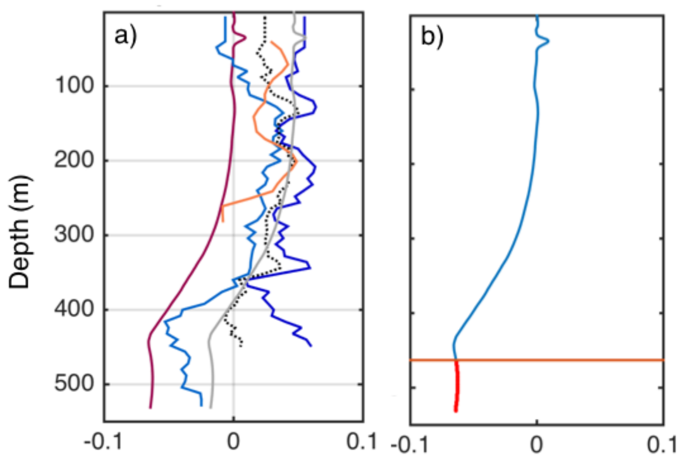

Figure 4.4: a) Example of geostrophic velocity (m s^{-1}) referenced to the average LADCP velocity (dashed black line), non-referenced geostrophic velocity (purple), SADCP velocity (orange), LADCP velocity at CTD stations (light and dark blue). The reference level was 100-430 m. b) shows the bottom triangle extrapolation (red) of geostrophic velocity (blue; m s^{-1}) shown in (a). Orange line indicates the deepest common level between the two CTD stations.

For the cross-section geostrophic transport calculations, the velocity in the bottom triangle was extrapolated (Fig. 4.4) following Thompson and Heywood (2008). The error in the transport estimates due to the choice of geostrophic referencing method is estimated to be $\pm 0.3 \cdot 10^{-3}$Sv. The absolute geostrophic velocities were also used for calculation of the cross-section temperature transport (Q_h), given by:

$$Q_h = C_p \int_{-D}^{0} \int_{x_1}^{x_n} \rho V (T - T_0)\, dz\, dx; \tag{4.1}$$

where x is the horizontal coordinate (m) from grid point x_1 to x_n, D is the water column depth (m) for which the integration is performed, Cp (JK^{-1}kg^{-1}) is the seawater specific heat capacity, ρ is the in-situ density, V (ms^{-1}) is cross-section absolute geostrophic velocity and $T - T_0$ is temperature minus a reference temperature. We use as a reference the surface freezing point of CDW, thus obtaining a temperature transport representing the amount of energy available for melting ice (Walker et al., 2007).

For each mooring, the current velocities were rotated using an angle defined based on bathymetry (Fig. 4.2b). The new coordinate system gives a rotated x axis that is along the main trough orientation (called along-trough; positive towards onshore) and an orthogonal rotated y axis (called along-slope) that is positive towards east. For mooring M5, which is at the shelf break, the angle of rotation for the new coordinate system was chosen so that the along-slope velocity component would follow the isobaths. Using the rotated velocities, for each of the current meters we quantify the i^{th} instantaneous temperature transport per unit area (TTF; hereafter referred to as total temperature flux for brevity). If we define horizontal velocity (along-trough or along-slope) as $V = \overline{V} + V'$, and temperature as $T = \overline{T} + T'$, total temperature transport (TTF) time series is calculated as:

$$TTF_{th} = C_p \cdot \rho_0(\overline{V}_{th} \cdot \overline{T}_{rth} + V'_{th} \cdot \overline{T}_{rth} + \overline{V} \cdot T'_{rth} + V'_{th} \cdot T'_{rth}); \tag{4.2}$$

where $T_r = T - T_0$, a bar indicates a time mean, and primes indicate a deviation from the time mean. The second term represents anomalous currents advecting mean temperature, whilst the third represents mean currents advecting anomalous temperature. The record-length mean TTF is then calculated as:

$$\overline{TTF} = C_p \cdot \rho_0(\overline{V} \cdot \overline{T_r} + \overline{V' \cdot T'_r}). \tag{4.3}$$

The first term is the mean temperature flux (MTF) and the second the mean eddy temperature flux (ETF). The record-length mean TTF is positive if heat is to be transported towards onshore (along-trough mean TTF component) and eastward (along-slope mean TTF component). These calculations were also performed using velocities that were rotated considering the angle of the average flow. Differences in temperature fluxes estimates due to the different choice of angle are low for most moorings (below 5%). This is not true for M20 and M5. At the position of M20, the flow rotates cyclonically to enter the narrow channel at the eastern portion of the trough (Kimura et al., 2017) and thus the mean flow does not follow the trough orientation. At M5, because of abrupt changes in the direction of the currents, the average angle for this mooring is not representative of the direction of the mean flow. We therefore opted to use the constant bathymetry-based rotation angle so there is a clear geographic reference for direction of the temperature flux and the abrupt changes in the flow direction would not affect our calculations. We also calculated the depth-integrated temperature flux by extrapolating linearly the velocity from each mooring current meter to the depths of temperature measurements available at each mooring, and then integrating vertically the temperature flux estimated at each depth. We used wavelet analysis (Morlet wavelets, according to Torrence and Compo, 1998) to illustrate the temporal variation of the temperature flux spectrum.

4.3 RESULTS

4.3.1 HYDROGRAPHY

The hydrographic setting encountered during February 2014 is presented in figures 4.5 and 4.6. The subsurface maximum temperature associated with CDW varies across the study area. The warmest and shallowest CDW subsurface temperature maximum ($\Theta \approx \theta = 1.86°$C), together with a warmer Winter Water core, is observed at stations 1 and 2 (Figs. 4.1 and 4.5). These are the northernmost and deepest stations sampled, being located at approximately the 3200 m and 2600 m isobaths along section MS4 (Fig. 4.1). Approximately 19 km south of station 2, at the 2200 m isobath, station 4 is the adjacent station on the meridional transect, and shows a temperature maximum of $\theta = 1.7$ °C. The subsurface temperature maximum of 1.8 °C can be used as an indicator of the position of the southern ACC front (SACCF; Orsi et al., 1995; Walker et al., 2013) and thus, we place the SACCF between stations 2 and 4, between the 2200 m and 2600 m isobaths. It roughly coincides with the SACCF position identified by Walker et al. (2013), who placed it at the base of the continental slope, near the 3000 m isobath. The remaining cross-slope sections do not reach this isobath and thus the upper CDW is colder than 1.74° C.

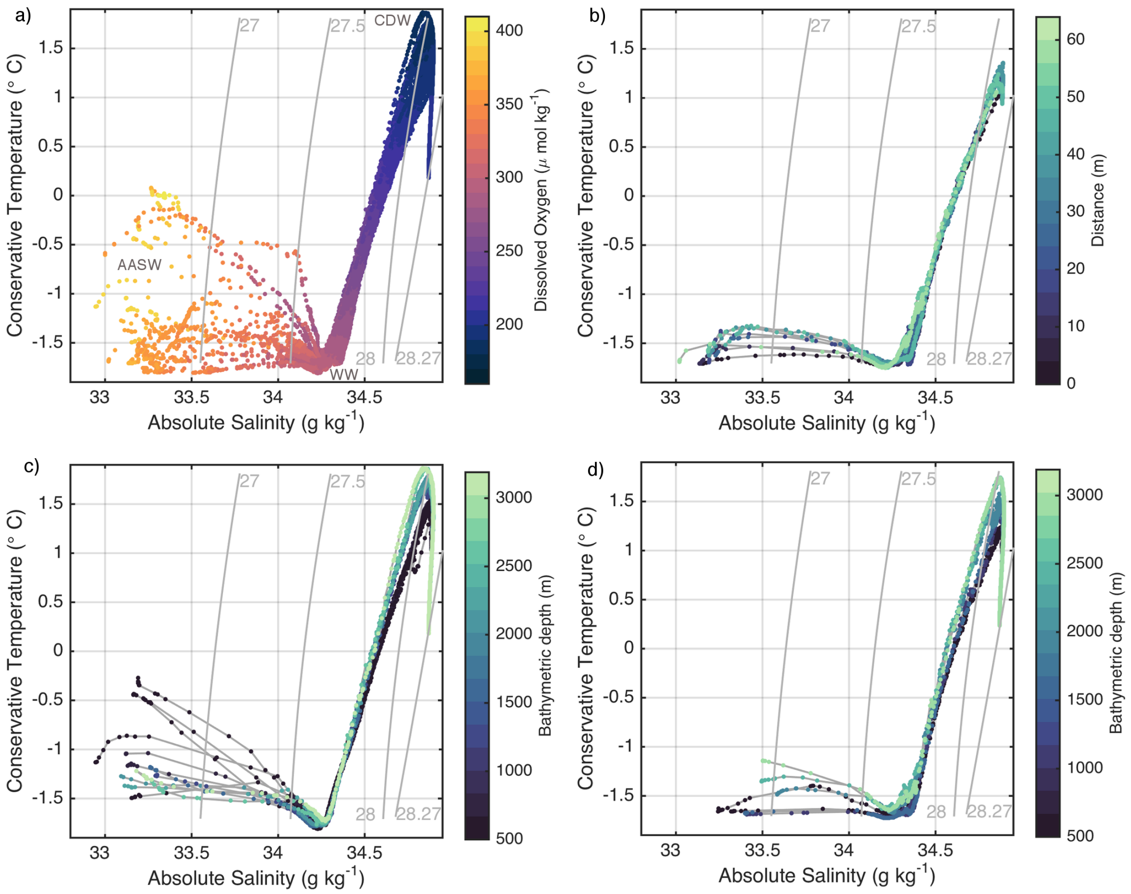

Figure 4.5: a) Conservative temperature (Θ °C) - Absolute salinity (S_A g kg^{-1}) diagram coloured by dissolved oxygen (μmol kg^{-1}) for all hydrographyc sections defined in figure 4.1. The main water masses are highlighted (Antarctic Surface water - AASW, Winter Water - WW and Circumpolar Deep Water - CDW). Panels b), c) and d) show $\Theta - S_A$ diagram coloured by distance (m; Sections ZS5) and bathymetric depth (m; Sections MS4 and MS2) at each station. Grey contours show neutral density (γ^n) surfaces.

Offshore of the shelf break, CDW fills most of the water column and shoals over the slope towards south whereas the cold ($\theta \leq 0°$) surface water deepens progressively over the continental shelf (Fig. 4.3.2) as previously described by Walker et al. (2013). Thus, there is an upwelling of isopycnals toward the continental shelf for waters below approximately 400 m and cooling of the Upper CDW temperature maximum associated with the donwelling of the Winter Water layer. This horizontal gradient over the slope marks the Antarctic Slope Front, which is an almost circumpolar feature that marks the subsurface boundary between warm and salty off shelf waters and cold and relatively fresh shelf waters (Jacobs, 1991; Heywood et al., 2004). The horizontal cross-slope gradient of hydrographic properties is evident by the decrease of the upper CDW temperature maximum from 1.7°C to 1.4 °C from areas offshore to areas onshore of the 650 m isobath at the vicinity of the eastern trough (Figs. 4.5c and 4.6). At the central trough (Fig. 4.5d), the temperature maximum of waters onshore of the 650 m isobath (approximately 1.27 °C) is colder than in the eastern trough. For all sections, the 28 $kg\,m^{-3}$ isopycnal, which defines the upper limit of the CDW, is found at approximately 400 m deep over the continental shelf (Fig. 4.6). Within the central trough, the temperature maximum is located between 400 and 500m, and the lower CDW is observed below this level with properties similar to offshore. At both the central and eastern troughs there is a cross-trough gradient in properties and distribution of water masses (zonal sections ZS5 and ZS6, respectively; Figs. 4.1 and 4.6), where the CDW is colder and found deeper in the water column (below 400 m) at the western flank of the troughs. This gradient is more evident at the eastern trough, which is also wider than the central. At the eastern trough, the warmest CDW is restricted to a narrow and deep channel, and what would be considered as lower CDW is absent at the western flank, where the temperature maximum is found above the bottom (Figs. 4.6 and 4.5).

The hydrographic sections and TS diagrams allowed us to characterize the CDW properties and distribution across the study area. These sections are then used to calculate geostrophic velocities and estimate the cross-section volume and temperature transport for both the entire water column and the CDW layer.

4.3.2 TRANSPORTS OF MASS AND HEAT FROM HYDROGRAPHIC SECTIONS

QUASI-MERIDIONAL SECTIONS

Consistent between all cross-slope sections, a surface-intensified westward flow is present at the proximity of the shelf break together with a subsurface or subsurface-intensified eastward flow (Fig. 4.6). The position and strength of these currents vary between sections. At the western flank of the central trough (section MS1) the surface westward current is observed at the shelf break, and the core of the subsurface-intensified eastward undercurrent is observed around the 1000 m isobath, weakening offshore. At the eastern flank of the central trough (section MS2), the surface westward flow is observed over the slope, offshore of the shelf break, whilst the eastward undercurrent is observed below 300 m depth. Further east, at the eastern

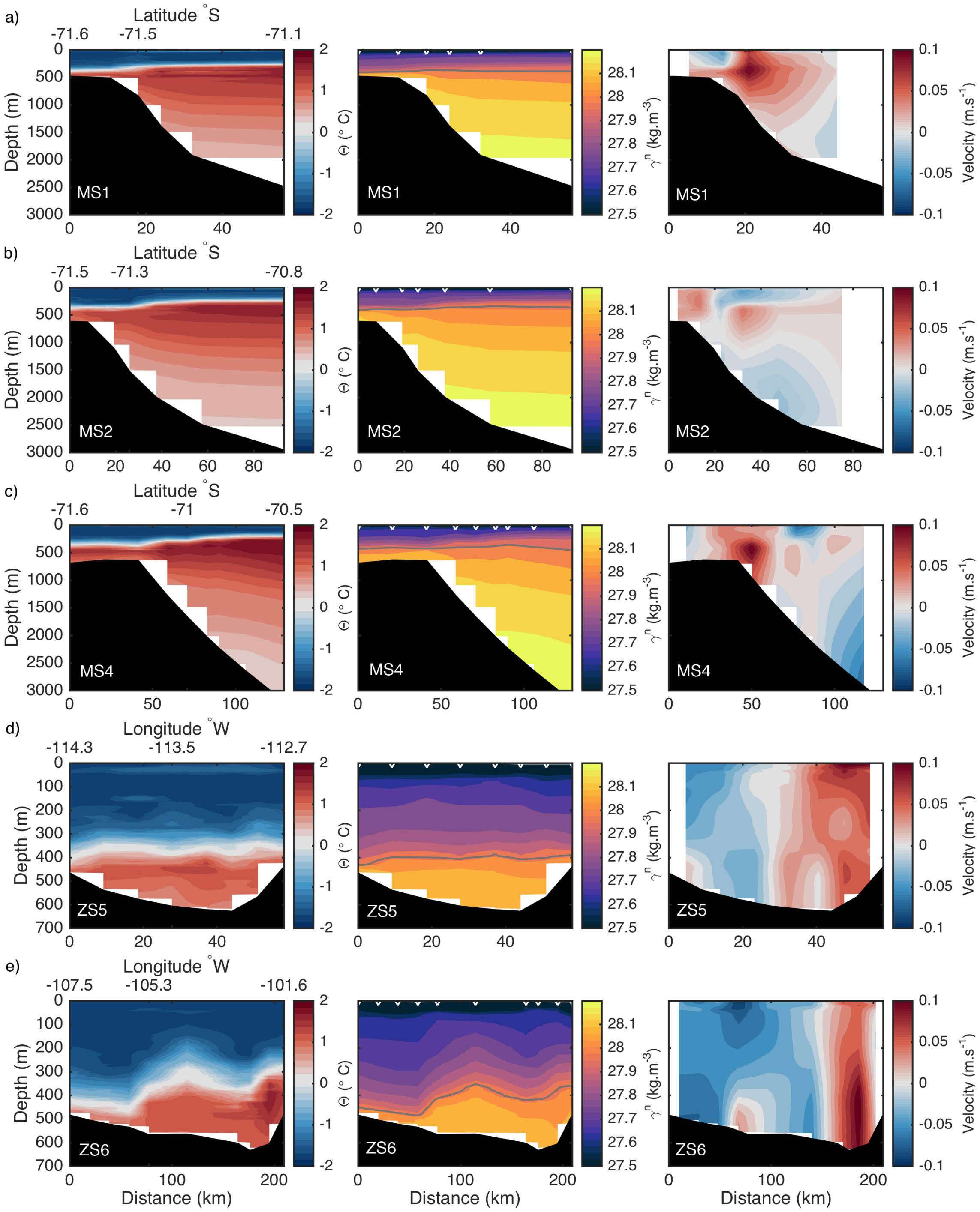

Figure 4.6: Conservative temperature (Θ°C), neutral density (γ_n Kgm^{-3}) and absolute geostrophic velocity (Velocity m s^{-1}; positive values indicate eastward/southward flow) fields for meridional sections a) MS1, b) MS2 and c) MS4, and zonal sections d) ZS5 and e) ZS6. Grey line on γ_n plots indicate the 28 kgm^{-3} isopycnal, and white triangles the position of CTD stations.

trough (section MS4), the eastward undercurrent has a similar strength and structure as observed at westernmost section MS1, occupying the entire water column and presenting a subsurface-intensified velocity core that weakens offshore.

The transport estimates show that the eastward flow prevails in the upper slope (between the shelf break and the 2000 m isobath), being consistent between all cross-slope sections (Fig. 4.7a). The transport estimates considering only the CDW layer (γ_n > 28.00 kg m^{-3}) follows the same pattern. Between the shelf break and the 2000m isobath, both the CDW volume and heat along slope transport decrease from the western to the eastern side of the central trough (MS1=0.56 Sv and 7.17 TW; MS2=0.41 Sv and 5.22 TW; MS3=0.08 Sv and 1.1 TW and enhances again further east, at the eastern trough (MS4=0.62 and 8.33 TW).

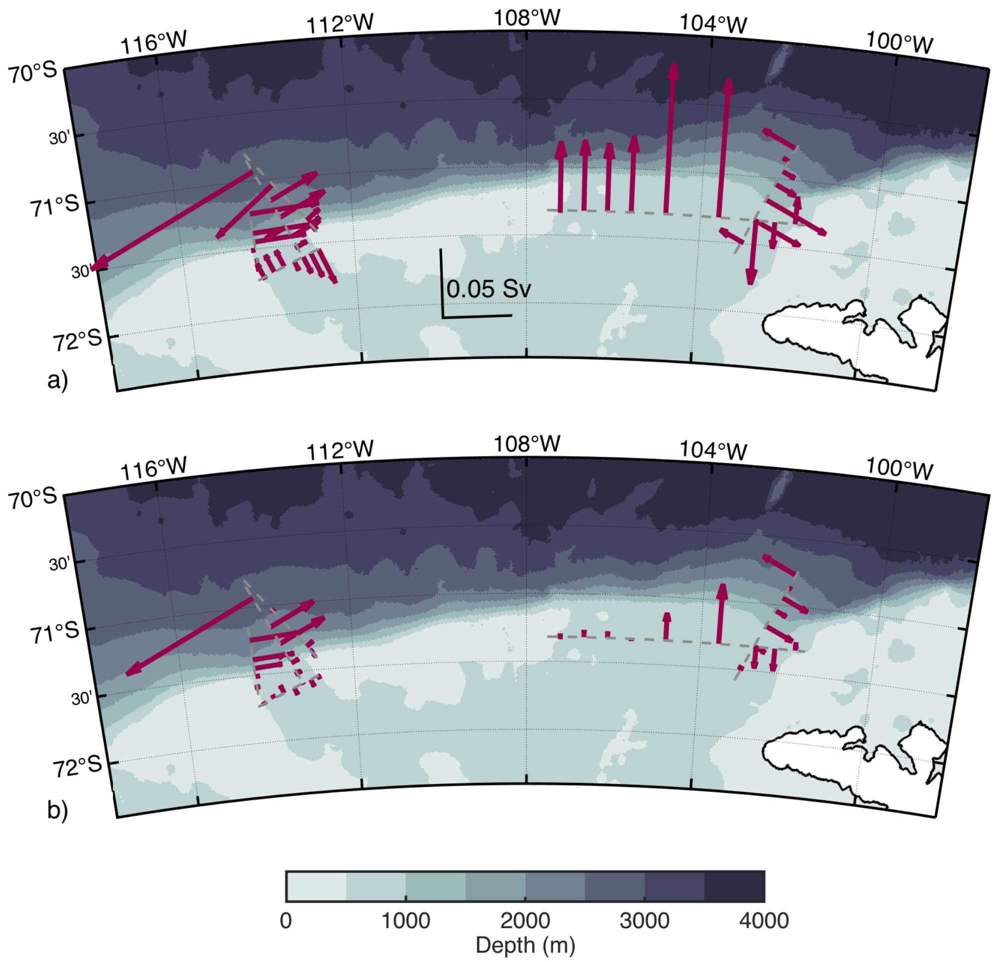

Figure 4.7: Arrows indicate cross-section transport (Sv) calculated from geostrophic velocities for a) water column and b) limited to CDW layer. Numbers indicate cross-section cumulative temperature transport (TW; 10^{-12} W) for the CDW layer. Positive numbers indicate eastward/onshore direction. IBCSO bathymetry (shaded)

Quasi-zonal sections

The inflow of warm waters onto the continental shelf occurs through the eastern portion of the channels in both central and eastern troughs (ZS5 and ZS6; Fig. 4.6). In the central trough (section ZS5), the inflow and outflow are similar in structure and velocity. The instantaneous net transport (i.e. section cumulative transport) is 0.28 Sv onto the shelf, of which 0.05 Sv is within the CDW layer (Fig. 4.7). The CDW inflow at the eastern portion of the central trough (0.13 Sv) is associated with a heat transport of 1.59 TW onto the shelf. Taking into account the CDW outflow in the western portion, the net heat transport at this trough is 0.61 TW onto the shelf. In the eastern trough (section ZS6; Fig. 4.6), the inflow occurs in a bottom-intensified narrow jet (approximately 50 km), which is coincident with the warmer temperature maximum observed in this part of the section. Similarly, the transport estimates (Fig. 4.7) show that the main inflow of CDW occurs through a narrow gap at the easternmost portion of the trough. There is a CDW inflow of 0.32 Sv (associated with a heat transport of 4.23 TW), but because a significant amount of this water mass flows north off the shelf at approximately 103.5°W possibly due to a local recirculation, the cumulative transport for CDW at this section is 0.46 Sv (5.48 TW) off the continental shelf. The main outflow across the section occurs further west, where the CDW outflow is negligible, leading to net transport of 3.73 Sv for the entire water column.

The hydrographic sections and cross-sections geostrophic transport estimates show that the along slope flow at the shelf break is dominated by the eastward undercurrent. Also, the main inflow of the CDW occurs at the eastern portion of the cross-trough sections ZS5 and ZS6 (central and eastern troughs), which is higher in terms of mass and heat transport at the later. These estimates are then put into perspective by evaluation of the variability of the coastal circulation and temperature transport estimated from the mooring time series (Section 4.3.3).

4.3.3 Mooring temperature transport and variability

The currents at the eastern (M1) and western (M4) flanks of the central trough flow mainly along the trough direction, towards onshore at its eastern side (average bearing of 158°at 460 m) and offshore at its western side (average bearing of 341°at 486 m). Offshore of the shelf break, at mooring M5, the flow is mainly eastward, with an average bearing of 97.5°at 400 m. Thus, the along-trough (along-slope) velocity is the main component of the flow at moorings M1 and M4 (M5).

The mooring time series reveal a considerable amount of intra- and interannual variability in hydrographic properties and velocity (Figs. 4.8, 4.9 and 4.10). At mooring M1/M12, there are two main periods in which there is an inflow of relatively warm (1.4-1.5 °C) and light (28.1-28.11 kgm^{-3}) waters, together with shallower (~ 350 m) isopycnals, which occur from April to June 2012 and October to November 2014. After each of these periods there is a cooling of the mCDW and a steady deepening of the thermocline (here we use the 0.5 °C as indicative of the base of the thermocline), reaching minimum temperature and maximum depths between November 2013 to April 2014 and November 2015 to February 2016. The first cold period includes the sampling of the hydrographic stations from Ocean2Ice cruise, which occurred during February 2014. There are no evident changes in salinity during these warm and cold periods. In the second cycle of warm-cold period, the fluctuations of the thermocline depth are amplified. The period of temperature minimum (after September 2015), which is the lowest in the time series, is also associated with lower salinity, higher density and a positive trend in on-shelf velocity at both 423 m and 555 m depths.

During the warm and cold periods between April 2012 and March 2014, the properties of the water masses at both 460m and 581m varied along the mixing line between Upper and Lower CDW (Fig. 4.11a). The same occurred at 555 m from March 2014 to February 2016, when the lowest temperatures of the entire time series were observed. In contrast, at 423 m depth, the properties of the water masses varied along the CDW - Winter Water (WW) mixing line from March 2014 to February 2016, showing the colder and fresher variety of mCDW by the end of the time series, when the influence of colder surface waters is stronger. This may indicate a change in the mixing through time, or can be a consequence of different depths of the shallowest instrument between periods.

Some of the features observed at the mooring time series at the eastern flank of the central trough (M1/M12; Fig. 4.8) are also present at its western side (M4; Fig. 4.9) and at the shelf-break mooring (M5; Fig. 4.10). For example, the relatively warm and salty period in the second half of 2012 (from June 2012 and January 2013). At M5, waters above 1.5° are found from 550 m to at least the depth of 300 m during this warm period and, as a consequence, the thermocline is shallowest. While during most of the time

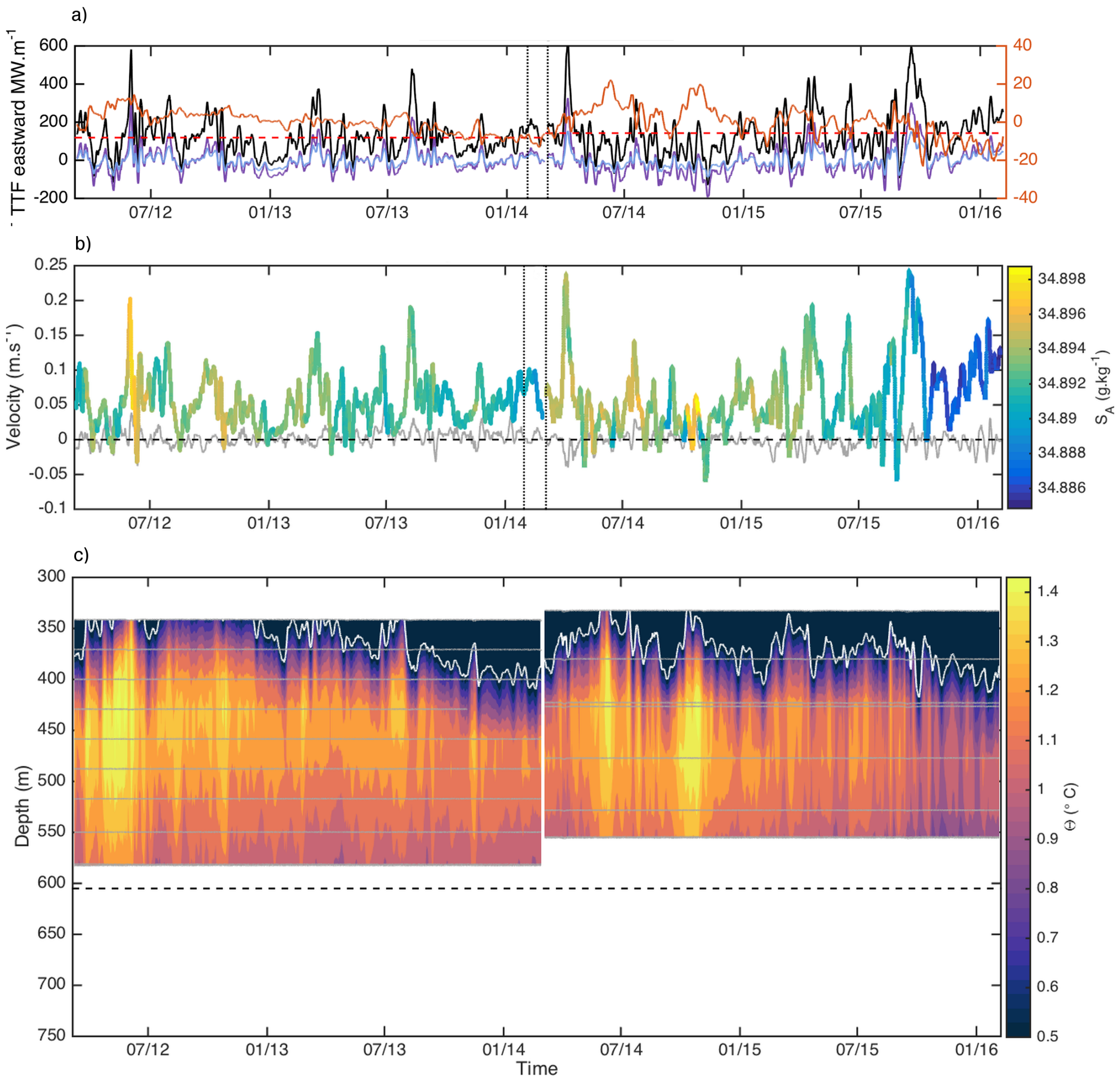

Figure 4.8: Moorings M1 and M12 a) Depth-integrated along-trough total (TTF; $\mathrm{MW\,m^{-1}}$, black) and eddy temperature flux (ETF; $\mathrm{MW\,m^{-1}}$, purple), for depths 341-581 m and 333-555 m, respectively. The temperature flux components ($V'\overline{T}$) and ($\overline{V}T'$) are represented by the blue and orange lines, respectively. Note that orange line follows the right axis and has different axis limits. Dashed red line indicates the mean depth-integrated TTF; b) Along-trough (coloured by absolute salinity) and along-slope (grey) velocity ($\mathrm{m\,s^{-1}}$) time series. Data is interpolated hourly and filtered using a 5-days running mean filter. Positive values indicate on-shore (along-slope) direction. Dashed vertical line in panels a and b indicate the cruise period; c) Conservative temperature (Θ° C) time series interpolated hourly and filtered using a 5-days running mean filter. The 0.5° C isotherm is highlighted in white. Gray lines indicate depth of original data. Black dashed lines show the local depth (m).

series the water properties measured at M4 at 487 m lie in the middle of the mixing line between CDW and WW (being lighter than 28.03 $\mathrm{kgm^{-3}}$), during the warm period of June 2012-January 2013 they are characteristic of mCDW. Similarly to M1, at M4

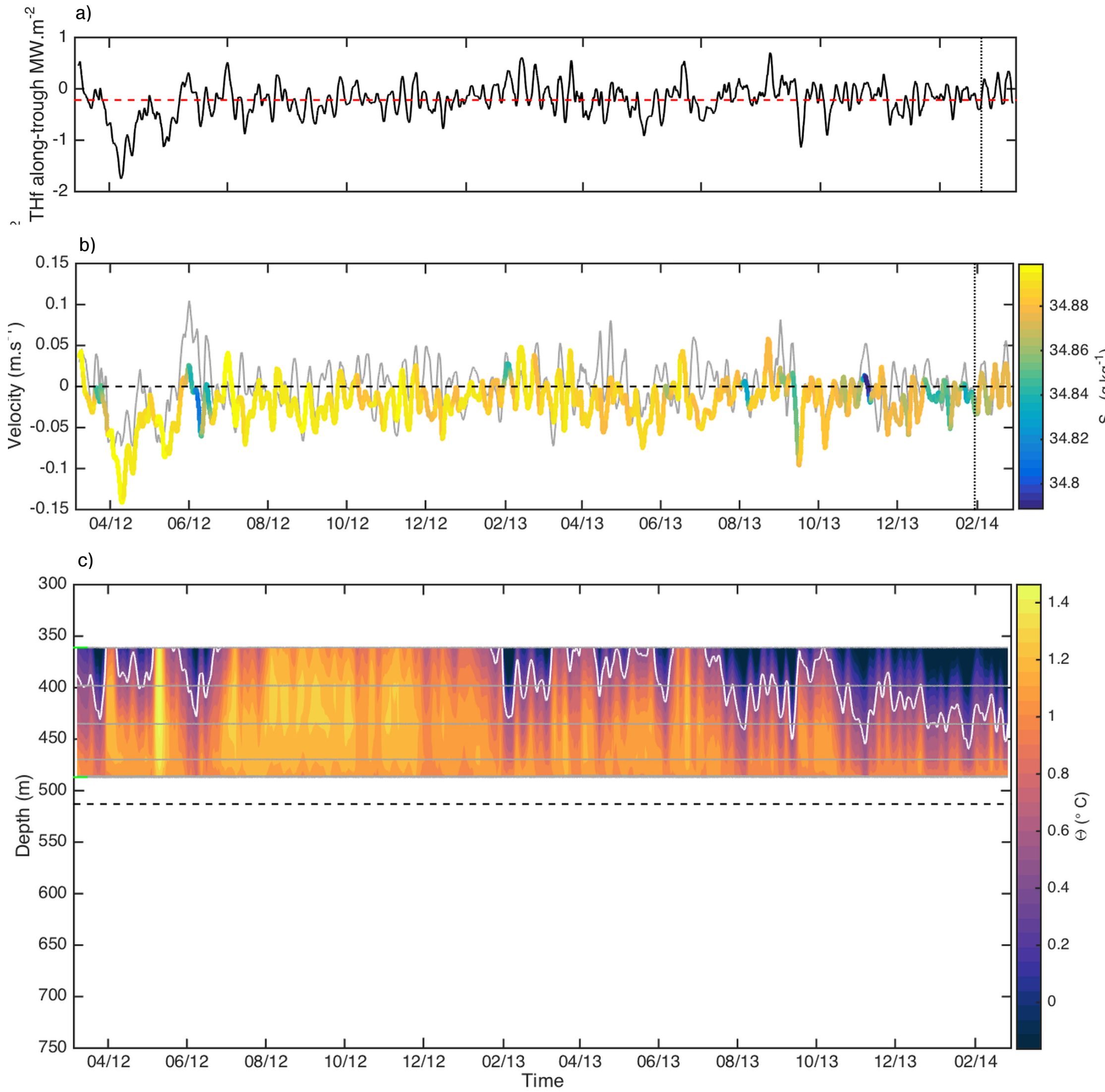

Figure 4.9: Mooring M4 a) Along-trough total temperature flux (TTF; $\mathrm{MW\,m^{-2}}$) at 486 m depth. Dashed red line indicate the mean TTF; b) Along-trough (coloured by absolute salinity) and along-slope (grey) velocity ($\mathrm{m\,s^{-1}}$) time series. Data is interpolated hourly and filtered using a 5-days running mean filter. Positive values indicate on-shore (along-slope) direction. Dashed vertical line in panels a and b indicate the cruise period; c) Conservative temperature (Θ° C) time series interpolated hourly and filtered using a 5-days running mean filter. The 0.5° C isotherm is highlighted in white. Gray lines indicate depth of original data. Black dashed lines show the local depth (m).

and M5 there is a steadily deepening of the thermocline and the decrease of overall temperature and salinity after May 2013, reaching its lowest values by March 2014. There are two periods during which no "pure CDW" ($\theta > 1.6°$) is found in the water column at M5; from March to May 2013, and from November 2013 to March 2014 (except for a very short warm water intrusion in the end of November 2013). These periods are also marked by relatively low salinity, particularly at 718 m.

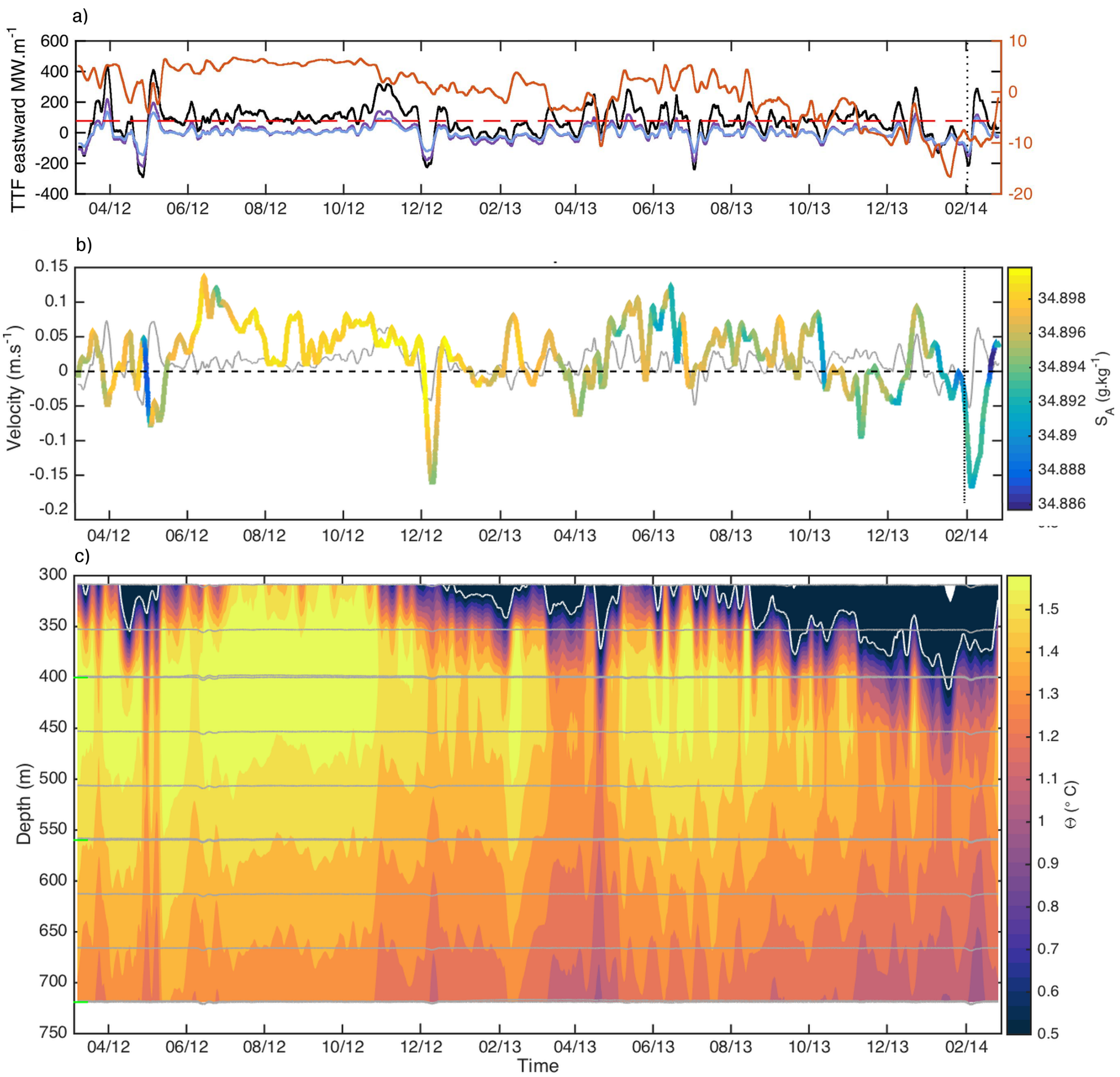

Figure 4.10: Mooring M5 a) Depth-integrated along-trough total (TTF; MW m^{-1}, black) and eddy temperature flux (ETF; MW m^{-1}, purple), for depths 309-719 m. The temperature flux components ($V'\overline{T}$) and ($\overline{V}T'$) are represented by the blue and orange lines, respectively. Note that orange line follows the right axis and has different axis limits. Dashed red line indicate the mean TTF; b) Along-slope (coloured by absolute salinity) and along-trough (grey) velocity (m s^{-1}) time series. Data is interpolated hourly and filtered using a 5-days running mean filter. Positive values indicate along-slope (on-shore) direction. Dashed vertical line in panels a and b indicate the cruise period; c) Conservative temperature (Θ° C) time series interpolated hourly and filtered using a 5-days running mean filter. The 0.5° C isotherm is highlighted in white. Gray lines indicate depth of original data.

At the shelf-break (M5), the flow is mostly south-eastward (towards onshore), but it is marked by abrupt changes in its direction from towards onshore to towards offshore (e.g. December 2013 and February 2014), associated with a rotation in flow direction that can last 15-30 days (Fig. 4.10). These episodes also coincide with the start of the main episodes of cold waters. These changes in the flow are similarly observed at all sampled depths. The longest period during which the flow direction remained constantly towards onshore occurred between June 2012 to December 2012, which coincides with the identified warm and salty period. The Ocean2Ice cruise happened during the most prominent event of change in the flow direction at M5. The cruise period was also characterized by the deepest isotherms and coldest waters during the two-year time series.

TEMPERATURE FLUXES CORRELATION

The total (TTF), mean (MTF) and eddy (ETF) temperature transport per unit area (referred as temperature flux) were estimated at each mooring, for each current meter depth (Figs. 4.8, 4.9 and 4.10), using the rotated velocities. At all moorings, most of the temperature flux variance is dominated by velocity. Off the shelf break (M5) is where temperature makes the greatest contribution to the along-slope temperature flux variance, for which the correlation coefficient between these two variables is 0.39. At M1, for example, the correlation between along-trough or along-slope temperature fluxes with temperature is below 0.1. The higher influence of the velocity variance over the total temperature heat flux in comparison with the temperature variance is confirmed by the magnitude of the $V'\overline{T}$ and $\overline{V}T'$ temperature flux components, where the later is mostly one order of magnitude smaller than the former.

Despite the common features in the mooring time series, the correlation of temperature flux time series between moorings is relatively low. We calculated lagged correlations of up to 180 days of time series averaged in windows of 1, 7 and 15 days. In all cases the highest correlations were found for the 15-days averaged time series, possibly because this window filters the variability observed in velocity (e.g. 4.10). The maximum correlation between M5 and M1 occurs between the former along-slope (at 717 m) and the latter along-trough (at 581 m) temperature flux time series (15-day average) at no lag, with a correlation coefficient r=0.27. M1 along-trough temperature flux (at 581 m) is correlated at no lag with along-trough (r=0.32) and along-slope (r=0.31) M4 temperature flux (at 486 m). Interestingly, the highest

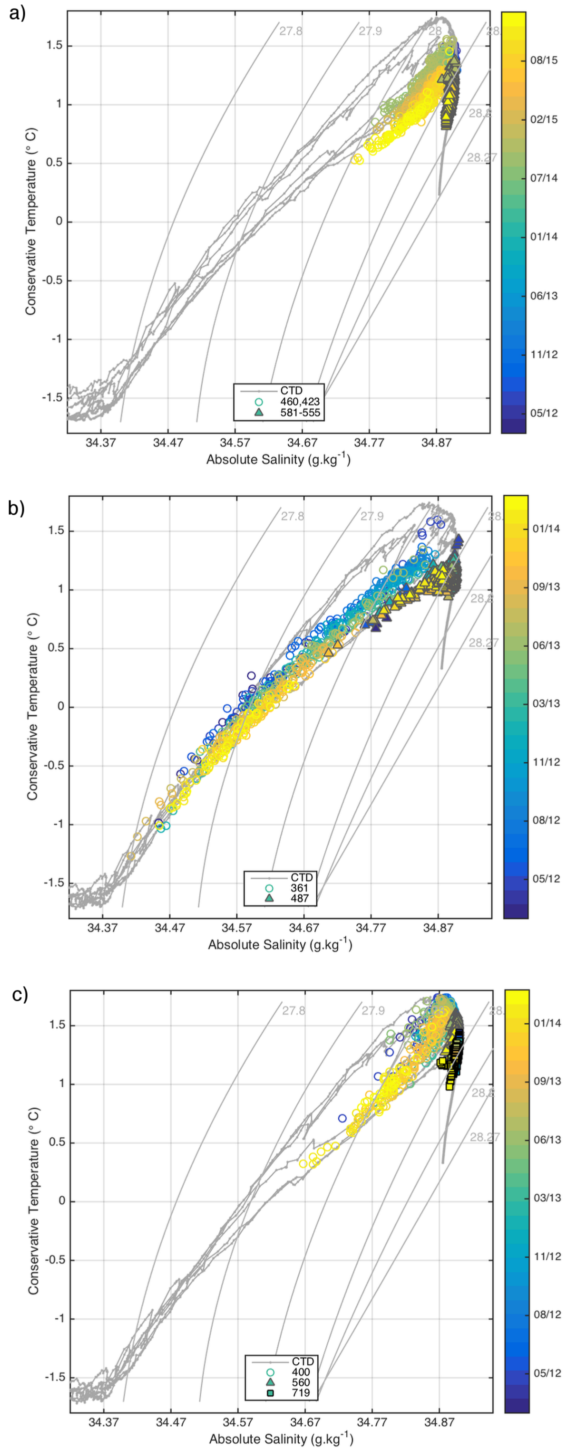

Figure 4.11: Conservative temperature (Θ) - Absolute salinity ($\Theta - S_A$) diagram coloured by time for moorings a) M1/M12, b) M4 and c) M5. Data is daily averaged. Legend indicates the depth of the instruments. CTD data in the region is shown in grey. Contours show neutral density (γ^n) surfaces.

correlation among moorings occurs between M12 (central trough) and M20 (eastern trough). The along-trough temperature flux of mooring M12 (at 555 m) is correlated at a 2 days lag (M12 leading) with M20 (at 595 m) along-trough (r=0.33) and along-slope (r=0.38). Despite being within the eastern trough, mooring M20 main flow is mostly eastward (119°bearing).All these correlations are statistically significant at 95% level.

The correlation between moorings is increased when the vertically integrated temperature flux is used in the analysis. The M5 along-slope and M1 along-trough vertically integrated temperature flux (15-day average) are correlated at no lag with r=0.38, whilst along-trough M12 is correlated with along-trough M20 with r=0.72 at no lag. The correlation between the depth-averaged temperature from the different moorings is also considered. For the moorings in the vicinity of the central trough (M5 and M1), the temperature correlation is high (r=0.8) and greater than heat flux correlations, whilst between central (M12) and eastern troughs (M20) temperature correlation (0.48) is significant but lower than the temperature flux correlations. This demonstrates that the correlation estimated between temperature fluxes between these moorings is primarily dictated by current dynamics, which is in agreement with the velocity variability leading the variability of the temperature flux.

MEAN TEMPERATURE FLUXES

The mean direction of the TTF and the MTF averaged for the whole sampling period are consistent between the different depths at all moorings (Fig. 4.12a and Table 4.2). The mean along-trough TTF and MTF at M1 is triple the values calculated at M4 when similar meters above bottom (MAB) are compared (581 m; 24 m MAB and 485 m; 27 m MAB, respectively). At M1 the TTF and MTF direction is towards onshore, in contrast with M4, which present negative (towards offshore) along-trough TTF and MTF values (Fig. 4.12a and table 4.2). At the same depth, the absolute TTF and MTF at M1 (581 m) is almost double that of M5 (558 m), which average flow is mostly along the slope. This ratio increases to approximately 3.8 when along-trough components of TTF and MTF are compared.

For the moorings inside the troughs, the mean ETF values point to the opposite direction of the mean TTF (and MTF) and across isobaths, i.e., towards offshore for M4 and onshore for M1, M11, M12 and M20 (Fig. 4.12a and Table 4.2). Offshore

			Full Period			Cruise period		
			Absolute	Along-trough	Along-slope	Absolute	Along-trough	Along-slope
M1	460 m	TTF	4.54×10^5	4.30×10^5	-1.47×10^5	7.09×10^5	6.86×10^5	-1.79×10^5
		ETF	2.46×10^3	-2.45×10^3	1.78×10^2	1.07×10^3	-3.51×10^2	-1.01×10^3
		MTF	4.56×10^5	4.32×10^5	-1.47×10^5	7.09×10^5	6.86×10^5	-1.78×10^5
	581 m	TTF	6.47×10^5	6.46×10^5	3.82×10^4	8.60×10^5	8.59×10^5	3.18×10^4
		ETF	1.97×10^3	-1.88×10^3	-5.92×10^2	7.12×10^2	1.77×10^2	-6.90×10^2
		MTF	6.49×10^5	6.48×10^5	3.88×10^4	8.60×10^5	8.59×10^5	3.25×10^4
M11	555 m	TTF	6.33×10^5	6.30×10^5	-6.57×10^4		-	
		ETF	5.44×10^3	-5.42×10^3	-4.95×10^2		-	
		MTF	6.38×10^5	6.35×10^5	-6.52×10^4		-	
M12	422 m	TTF	6.77×10^5	6.73×10^5	-7.47×10^4		-	
		ETF	1.42×10^4	-1.42×10^4	5.02×10^2		-	
		MTF	6.92×10^5	6.87×10^5	-7.52×10^4		-	
	555 m	TTF	7.27×10^5	7.27×10^5	-2.26×10^4		-	
		ETF	1.19×10^4	-1.19×10^4	-2.94×10^1		-	
		MTF	7.39×10^5	7.39×10^5	-2.26×10^4		-	
M4	485 m	TTF	2.18×10^5	-2.18×10^5	-6.02×10^3	9.43×10^4	-9.09×10^4	2.49×10^4
		ETF	1.19×10^3	8.06×10^2	-8.77×10^2	4.95×10^3	3.24×10^3	3.75×10^3
		MTF	2.19×10^5	-2.19×10^5	-5.14×10^3	9.65×10^4	-9.41×10^4	2.11×10^4
M5	399 m	TTF	5.52×10^5	2.33×10^5	5.00×10^5	2.91×10^5	1.45×10^5	-2.52×10^5
		ETF	2.37×10^4	4.37×10^3	2.33×10^4	2.28×10^4	-3.79×10^3	2.25×10^4
		MTF	5.29×10^5	2.29×10^5	4.77×10^5	3.12×10^5	1.48×10^5	-2.75×10^5
	558 m	TTF	3.65×10^5	1.67×10^5	3.25×10^5	7.27×10^5	1.51×10^5	-7.11×10^5
		ETF	8.19×10^3	-1.63×10^2	8.19×10^3	1.31×10^4	-4.16×10^3	1.25×10^4
		MTF	3.58×10^5	1.67×10^5	3.16×10^5	7.40×10^5	1.55×10^5	-7.23×10^5
	718 m	TTF	2.26×10^5	1.48×10^5	1.70×10^5	6.49×10^5	1.81×10^5	-6.23×10^5
		ETF	6.31×10^3	-2.24×10^1	6.31×10^3	1.44×10^4	-4.96×10^3	1.35×10^4
		MTF	2.21×10^5	1.48×10^5	1.64×10^5	6.63×10^5	1.86×10^5	-6.36×10^5
M20	467 m	TTF	1.27×10^6	3.92×10^5	1.20×10^6		-	
		ETF	2.14×10^4	-1.00×10^4	-1.89×10^4		-	
		MTF	1.29×10^6	4.02×10^5	1.22×10^6		-	
	595 m	TTF	1.28×10^6	2.00×10^5	1.27×10^6		-	
		ETF	8.17×10^3	-2.21×10^3	-7.87×10^3		-	
		MTF	1.29×10^6	2.02×10^5	1.27×10^6		-	

Table 4.2: Total (TTF), Eddy (ETF) and Mean (MTF) temperature flux (Wm^{-2}) at each depth, for each mooring, averaged for their entire sampling period and only the cruise period. Absolute values refer to the resultant temperature flux from along-trough (rotated x axis) and along-slope (rotated y axis) components.

of the shelf break, however, the mean ETF calculated from M5 follows the isobaths, parallel to the continental slope. Inside the troughs, the absolute mean ETF is about two orders of magnitude smaller than the mean TTF when the average is calculated for the whole sampling period (Fig. 4.12 and table 4.2). This is not true for M12 at the eastern trough, which, together with M5 at the shelf break, show higher ETF values that are only one order of magnitude smaller than the mean TTF. At similar depths, the along-slope mean ETF at M5 is about 4 times greater than the offshore mean ETF at M1.

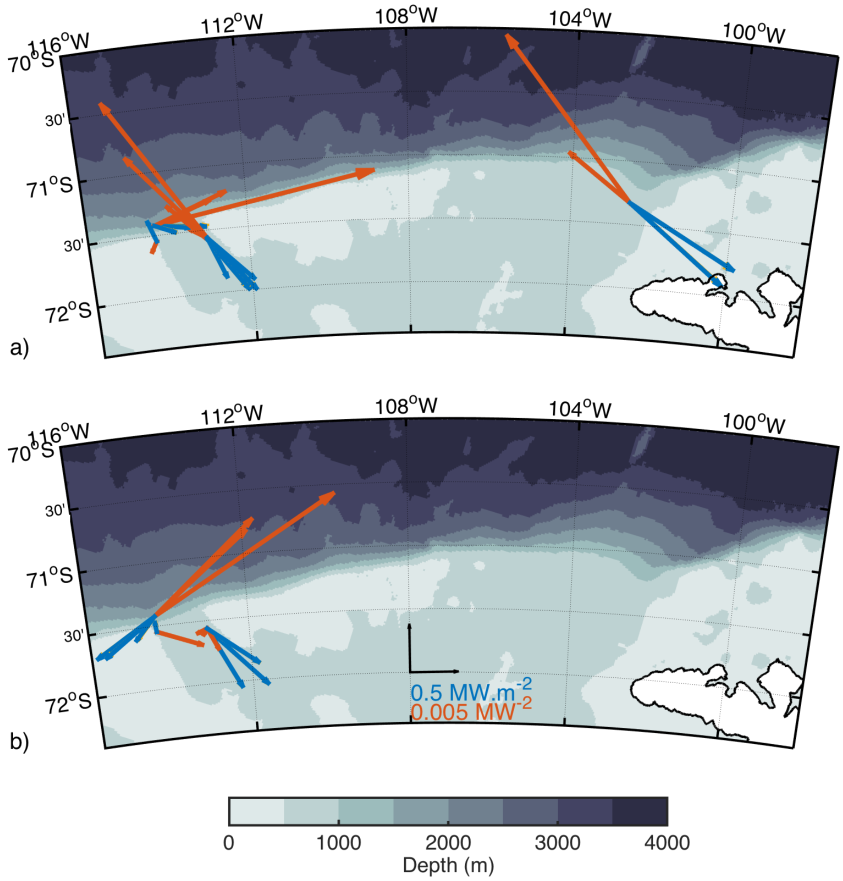

Figure 4.12: Total (TTF; orange), Eddy (ETF; red) and Mean (MTF; blue) temperature flux for each mooring, at each depth, averaged for (a) the mooring total sampling period and (b) for the cruise period (30/01/2014 to 05/03/2014). Notice that ETF and TTF have different scales on the map.

Even though the direction of the temperature fluxes at the eastern flank of the central trough are consistent through time (among moorings M11, M1 and M12), the absolute and along-trough MTF during the period of M12 (2014-2016) is 16% higher than M11 (2009-2010) and 14% higher than M1 (2012-2014; Fig. 4.12a and Table 4.2). The integrated along-trough TTF during M12 is 38% higher than in M1. For M12, the mean ETF, which is directed offshore, is also significantly higher than in previous years, being 2 times greater than the mean value for M11 and 6 times greater than M1, probably because of the very low variability during the warm period. At the position of M20 (2014-2016), the flow rotates cyclonically to enter the narrow channel at the eastern portion of the trough, as suggested by modeling work (Kimura et al., 2017). The flow is fairly constant onshore, thus we can assume that the both along-trough and along-slope components will contribute to the temperature flux onto the shelf, as well as at M12. Comparing the absolute MTF and TTF at both moorings, at the eastern trough (M20) the absolute MTF and TTF are approximately 1.8 times higher than at the central trough (M12) between March 2012 to February 2016.

The magnitude and direction of the mean temperature fluxes are considerably different when only the cruise period is considered for the average calculations (Fig. 4.12b and table 4.2). The most striking difference is observed at M5, in which the mean direction of MTF and mean TTF during the cruise point southwestward, while the mean ETF is directed towards offshore. At M1, the MTF and mean TTF are greater during the cruise period in relation to the 2 years average by 33% at 581 m, while the mean offshore ETF decreases by one order of magnitude. In contrast, at M4 the offshore mean TTF and MTF are lower during the cruise whilst the onshore mean ETF is 4 times greater.

WAVELET ANALYSIS

A wavelet analysis, with scales between 2 days and a month, was used to evaluate the high frequency variability of the temperature flux power spectrum. The temperature flux is highly correlated with the velocity time series at all moorings and therefore changes in the flow are expected to drive the variability of the temperature flux. For example, the main events of rotation in the flow direction at M5 are mostly associated with energy peaks in the wavelets of the along-trough (cross-slope) temperature flux time series (Figs. 4.13 and 4.10). The event of flow rotation that occurs during the early 2014 Ocean2Ice cruise is reflected in the along-trough TTF wavelet analysis by a statistically significant energy peak at frequencies between 8-24 days at 718m, leading to a peak of 0.2 MW^2 in the 1-30 days average variance. This signal is also present in the shallower depths, but associated with lower energy levels and shorter periods (6-10 days at 399 m). The hydrographic sampling started at the peak of this event and took around one month to complete. Therefore the transport estimates from the hydrographic sections were likely to be influenced by subinertial variability and are unlikely to be representative of the long term mean. A period of low energy levels at frequencies below 16 days is present in the along-trough TTF at M5 (559 m; from August 2012 to April 2013; Fig. 4.13c), which results from very low variance (energy) in the temperature time series and a constant onshore flow. When longer periods are evaluated (30 days to 8 months), M5 is the only mooring that shows robust energy

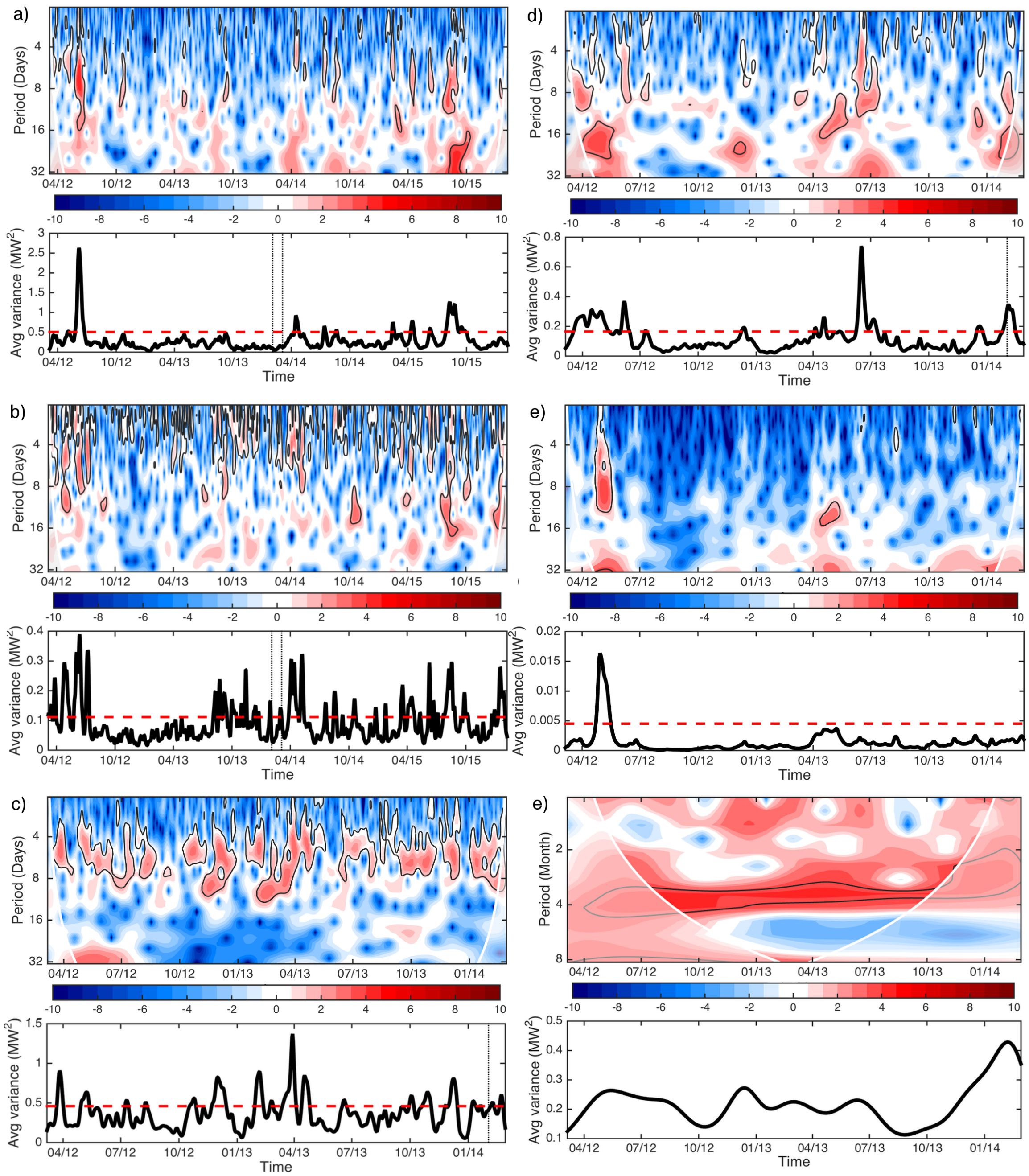

Figure 4.13: Wavelets analysis of (a) along-trough and (b) along-slope total temperature flux (TTF) at moorings M1 (581 m depth) and M12 (555 m depth); (c) M4 along-trough TTF at 486 m depth; (d) along-trough TTF, (e) temperature and (f) along-slope TTF at mooring M5 at 558 m depth; Bottom panels show scale-average time series for 1-30 days (a-e) and 1-8 months (f). Vertical dashed lines indicate the cruise period. All time series are interpolated to daily values.

peaks in the TTF wavelets (Figs. 4.13f). At all depths (but more particularly at the two deeper depths), the along-slope TTF series show an energy peak at 4 months at the beginning of the time series, which gradually shifts to a 2-3 month period at the end of the time series.

Both along-trough and along-slope (not shown) TTF at M4 (Fig. 4.13) show a clear energy peak between 4-8 days period along the entire time series. This signal is not present in the wavelets of temperature time series, and no other mooring shows such coherent signal. At the eastern flank of the central trough (M1/M12), the along-trough TTF time series show 4-16 days energy peaks, which occur annually between April and October, i.e. austral winter (Fig. 4.13a). Most of the energy (for periods lower than a month) of the along-slope TTF is concentrated in periods shorter than 8 days. After August 2014 (M12), however, there is a shift in the energy spectrum towards 8-16 days periods (Fig. 4.13b). The period of low energy levels observed in the along-trough TTF wavelets at M5 is also present in the along-slope TTF at M1 (average 1-30 days variance below 0.1 MW^2; August 2012 to August 2013). At the same time that there is a shift in the energy of along-slope TTF from lower periods to periods of 8-16 days at M12, energy peaks at these periods in the along-slope TTF at M20 (not shown) are also observed. At this mooring, however, the signal is coherent and less contaminated by higher frequency variability than at M12.

4.4 DISCUSSIONS

The eastward undercurrent dominates the transport at the upper slope, being located between the shelf break and the 2000m isobath. Our observations from early 2014 show that the undercurrent described from in situ data in 2003 (Walker et al., 2013) and from modeling studies (e.g. Assmann et al., 2013) is a persistent feature. The decrease in the eastward flow from the western side to the eastern side of the central trough and partial recovery further east observed here is also described by Walker et al. (2013) and is consistent with most of the flow turning cyclonically to enter the central trough. The inflow of CDW occurs at the eastern portion of both central and eastern troughs, while the western part is filled with the outflow of a colder and deeper mCDW.

During the cruise period, the on-shore CDW heat transport estimated for the eastern portion of the central and eastern troughs is higher in the later by 2.64 TW due to greater mass transport and temperature differences between the inflow in the two regions. Jacobs et al. (2011) argues that although the CDW supplied by the eastern trough is warmer than in the central trough, its contribution to glacial melting is primary controlled by the thermocline depth in the inner continental shelf instead of temperature of CDW core.

The cumulative onshore volume and temperature transport estimated for the CDW layer at the central trough (0.05 Sv and 0.61 TW onto the shelf) are lower than the estimates made by Walker et al. (2007) for a dataset collected in March 2003 (0.23± 0.62 Sv and 2.8 ± 0.68 TW), possibly associated with the anomalous cold temperatures found during the 2014 cruise. Assmann et al. (2013) estimated the CDW volume transport at the central trough for 2003 and 2006, which shows considerable interannual variability. If we consider the section sampled in 2006, which has a similar flow structure and velocity to our dataset, our CDW volume transport is more consistent with their estimates, particularly if we compare the same de-tiding method (0.108 ± 0.039 Sv transported onto the shelf; their table 3). At a further west trough (Dotson trough), Ha et al. (2014) estimate an average inflow of CDW of 0.34 Sv and a temperature transport of 2.82 TW during 2011 by integrating vertically (320m-bottom) the velocity measurements from the mooring's ADCPs and then multiplying by an average flow width estimated by the hydrographic sections. If we make similar assumptions, an average on-shore temperature flux of 1.77 TW is estimated for 2012-2014 and 2.45 TW for 2014-2016 in the central trough (considering a fixed inflow width of 27 km) and 1.86 TW during 2014-2016 at the eastern trough (fixed inflow width of 50 km). This could suggest that during 2014-2016 the central trough had a greater contribution to the temperature transport onto the shelf than the eastern trough. Our flow width, however, is based on a section in early 2014 and it is unlikely that it remained the same for the following two years. In a modeling study, (Kimura et al., 2017) estimates a climatological onshore temperature transport that is similar to ours at the central trough (2.5 TW).

A seasonal cycle in the thickness and temperature of the CDW layer is not evident in the moorings evaluated in this study. A seasonal cycle is also absent in all of the mooring temperature fluxes, which is in agreement with the lack of seasonality of the closely correlated velocity time series. Despite the lack of evidence of seasonal changes in the CDW thickness at the shelf break, this signal has been identified further south in the eastern Amundsen Sea continental shelf (Webber et al., 2017; Mallett et al., 2018). Seasonal variations in the warm layer thickness associated with Ekman pumping are reported at the western (Dotson) trough (Kim et al., 2017). However, the orientation of the western and central troughs are different and thus it is possible that they respond differently to surface stress (Kimura et al., 2017).

The mooring temperature time series show strong interannual variability. There are two main events of inflow of relatively warm waters in the longest time series (M1 and M12; March 2012 to February 2016), each one followed a period of cooling of the mCDW and deepening of the thermocline. It could be argued that these hydrographic variability observed by the mooring are a result of a spatial variability, due to the drift of the warmer inflow and colder outflow within the trough, rather than temporal variability. This is, however, unlikely, because the horizontal gradient (1.06 - 1.35 °C) of the CDW temperature maximum during the cruise occupation (during the cold period of 2014) is lower than the variation observed by the mooring between the warm and cold cycles (0.94 - 1.47 °C at 477 m). Moreover, the warm episode of mid-2012 and subsequent cooling are observed in both moorings within the central trough and at the upper slope. For all these moorings, during the warm event the thermocline is shallowest in the water column, and it is also characterised by a constant on-shore flow and a suppression/reduction of the temperature variability at the upper slope. The depth of the thermocline over the continental shelf is sensitive at a range of time scales to the zonal winds through its effect on the buoyancy forcing, coastal downwelling, and input of CDW onto the shelf (Thoma et al., 2008; St-Laurent et al., 2015; Kim et al., 2016; Jenkins et al., 2016). A warm period at the eastern Amundsen continental shelf break can occur in a scenario of weak easterly winds, which will promote less downwelling and enhance the undercurrent that brings CDW onto the shelf (Thoma et al., 2008; Jenkins et al., 2016). Similarly, the cold periods, particularly the anomalous event at the end of 2015, could be a consequence of stronger easterly winds increasing downwelling, suppressing the undercurrent and the limiting the access of CDW onto the shelf. This is in agreement with the temperature time series which show the warm spells associated with the shallowest thermocline and the cold periods characterised by its deepening. However, 2015-2016 was marked by a major El Niño event, which would potentially lead to weaker easterly winds, weaker Antarctic Slope current (Armitage et al., 2018) and a possible stronger undercurrent. As a consequence, a greater CDW inflow onto the continental shelf would be expected. Thus, the observed increase in velocity and temperature flux during this period is in agreement with what would be expected in an El Niño, but the hydrography diverges strongly, showing a cooling trend and deeper thermocline. Among the facts that could explain this disagreement, it is possible that the local atmospheric circulation had a configuration different than expected in El Niño years due to the interaction between the ENSO and the Southern Annual Mode (SAM) on the Amundsen Sea Low (ASL). It can also be the case that the undercurrent response to the changes in the winds are is somewhat different than expected. Also, observed cooling can be related to the core of the warm flow not being captured during the cold period due to movement of the front. The possible change in the mixing line observed during this period suggests that surface temperature fluxes nearby could have contributed to the cooling of the mCDW and the minimum temperatures.

The mid-2012 warm spell, shallow thermocline and subsequent cooling cycle coincides, but poorly correlates with the cold period, deep thermocline and subsequent warming (January 2012-January 2014) described by Webber et al. (2017) in a mooring further onshore, within Pine Island Bay. The different propagation speeds of the warm and cold anomalies, in addition to local atmospheric forcing, could explain why the signals observed at our moorings at the shelf break are not coherent with the variability observed at the Pine Island Bay (Webber et al., 2017; Kimura et al., 2017). The cold event described in the Pine Island Bay was attributed to anomalous wind conditions during 2011 due to a La Niña event development (Dutrieux, 2014), and also a result of local atmospheric forces, associated with a change in the circulation within the Pine Island Bay (Webber et al., 2017). The peak of the cooling period at the shelf (M1) coincides with the period of very low along-trough ETF magnitude at the shelf break (M5; April-October 2012), a consequence of a constant onshore flow of warm waters with low variance in the temperature and velocity. This may suggest that the strong local atmospheric forces over the shelf that led to a change in the circulation and the anomalous cold period also could have had effect on the suppression of eddy temperature flux which, in turn, could have contributed to the maintenance of the cold event. The eddy temperature flux is however one order of magnitude smaller than the TTF at the shelf break and thus it is unlikely that it would have such impact on the shelf variability.

Those warm-cold cycles, however, do not seem to strongly modulate the total temperature flux estimated for the moorings, which are strongly dictated by velocity.

Yet, interannual variability is observed in the temperature fluxes at the central trough by the increase of absolute and along-trough MTF and offshore ETF for 2009-2010; 2012-2014; 2014-2016 over time. The integrated along-trough TTF and ETF also increased in magnitude between the last two periods. These calculations do not take into account the depth of the thermocline, which would be necessary to more accurately estimate the changes in the temperature transport for the entire water column.

On top of the warm-cold cycles, at the upper slope (M5) there are a few cold spell episodes that are generally preceded by a short increase in velocities and a rotation on the flow at all depths. These events are associated mostly with energy on a 6-24 day period, which may indicate the passage of eddies. The appearance of weekly anomalies at the shelf break is consistent with the possible mechanisms that lead to the onshore flow within the trough (St-Laurent et al., 2013). The sampling of the hydrographic sections from the Ocean2Ice cruise started at the peak of a prominent cold spell, which was followed by the weakening and rotation of the velocities from westward along the slope to eastward. These abrupt changes in the currents and hydrography in time scales shorter than a month calls attention to the care that needs to be taken when using hydrographic sections for estimates of, e.g., heat and salt budgets.

The variance of the temperature fluxes is concentrated at short time scales (< 30 days). Mooring M5 is the only one in which significant energy is observed at monthly or longer time scales, with the main energy peaks of eastward temperature flux concentrated between 2-3 months. This could be related to changes in the front position and consequent changes in temperature and along slope currents. Moorings on different sides of the central trough show different short-term variability in temperature flux. The clear 4-8 days period energy peak in the offshore temperature flux at western flank of the central trough is associated with the flow velocity variability, and no other mooring shows such coherent signal. It is possible that this energy peak is associated with barotropic oscillations in the flow. Quasi-regular oscillations with period of 2.5 and 3-4 days were described at the outflow of the western (Dotson) trough, associated with resonant topographic Rossby waves (Wåhlin et al., 2016). The inflow mooring (M1) does not show a clear signal, which may be a consequence of a too slow resonant period that does not permit free waves to form (Wåhlin et al., 2016). Even though waves do not induce net transport of quantities, our calculated temperature flux is dominated by velocity which would explain why we observe these oscillations in the flux time series. Coastal-trapped waves can influence mixing and lift/drop the thermocline (Wåhlin et al., 2016) which, at the shelf-break, will influence the amount of heat that goes onshore. In Artic fjords, the exchange driven by the propagation of coastal-trapped waves steered by the topography of across-shelf troughs can exceed both tidal and estuarine exchange (Inall et al., 2015).

Both moorings M12 and M20 (located at the CDW inflow of the central and eastern troughs, respectively) show some energy concentrated at periods of 8-16 days, with the signal on the former more coherent and less contaminated than on the latter. This is consistent with the relatively high correlation between the two moorings temperature fluxes with a two day lag. The 2 day lag between these moorings that are approximately 400 km distant, may suggest that their variability could be connected by the propagation of baroclinic waves along the slope. For any of the averaging-windows chosen, the correlation between these moorings is higher than the correlation between temperature flux from moorings M5 and M1. The correlation between the temperature flux at the shelf break and the trough inflow despite being statistically significant is relatively low and thus contrasts the theoretical arguments that the undercurrent strength strongly influences the temperature flux onto the shelf (Walker et al., 2013; Thoma et al., 2008; Jenkins et al., 2016).

4.4.1 FINAL REMARKS

The hydrographic sections evaluated here show velocity structures similar to previous studies, suggesting that the location of these currents are fairly consistent through time. The time series from four moorings, of up to 4 years, show significant variability in several time scales of temperature flux estimates, with changes in the strength and direction of the flow, as well as temperature. This variability includes abrupt changes in hydrography and currents in short time scales (~ 15 days), which indicates that snapshots of the ocean condition should be interpreted with caution. Eddies are likely contributors to the variability at the shelf-break. Inside the central trough, the high frequency variability of the temperature flux may also be influenced by barotropic oscillations. At interannual time scales, the mean along-trough total and eddy temperature flux within the central trough increased between 2012-2014 to 2014-2016, while the eddy temperature flux appears to be somehow affected by the conditions that lead to warm/cold periods. Despite the consistency among moorings of anomalous periods in temperature and variation in thermocline depth, the correlation between the temperature flux at the shelf-break and inside the trough is relatively low. There is not enough evidence to confirm the influence of the slope undercurrent in the on-shelf temperature transport. Furthermore, the observed cooling and deepening of the thermocline during the last major El Niño event (2015-2016) may indicate that the undercurrent response to changes in the atmospheric forcing can differ from predictions, or that it requires a longer response time for this to be observed. In the projected scenario of increased frequency of extreme El Niño events (Cai et al., 2014; Wang et al., 2017), it is critical that the mechanism of response of the undercurrent to changes in atmospheric forcing is further investigated.

5

Synthesis and final considerations

5.1 Summary

This thesis investigats the dynamical oceanographic processes associated with the continental slope frontal system around Antarctica (more specifically in the Weddell and Amundsen Seas) that can influence the cross-slope exchange of properties. The results of this thesis show that these cross-slope processes are climatically important, firstly because they can regulate the export of dense waters from the shelf (Chapter 2), and secondly because they may influence the variability of heat that is transported onshore and that can eventually contribute to ice-shelf melting (Chapter 4). Moreover, these processes have an effect on local biological productivity by determining the physical conditions that contribute to the maintenance of distinct biological regions either side of the slope front (Chapter 3).

5.1.1 The northwestern Weddell Sea

In the Weddell Sea (Chapter 2), data from three Seagliders were used to better understand the temporal and spatial variability of the slope frontal system. Variability on short time scales (3 to 4 days) is significant, and that the along-slope transport can vary within this time scale, which means that the front itself changes. The cross-slope advection of eddies is likely to contribute to this variability. We also observed dynamical changes when the dense flow was present. The presence of the dense flow is associated with higher eddy kinetic energy and a greater susceptibility of the geostrophic flow to baroclinic instabilities that fuel the eddy field, the main mechanism by which warm waters are transported onto the shelf. In Chapter 3, we show that the front segregates two different biological regions onshore and offshore and that the different physical characteristics contribute to the different levels of biological production between these regions.

Our results reveal important aspects of the local dynamical processes, which leads to future questions. The long-term variability of the dense water properties have been discussed in many studies (e.g. Purkey and Johnson, 2013; Azaneu et al., 2013; Schmidtko et al., 2014), many of which suggest a decrease of density and/or export of this dense water in the recent decades. In addition to the consequences that this may have for the strength of the meridional overturning circulation and the transport of heat and salt across the world ocean, it may also alter the dynamical processes in the continental slope region. Because of the importance of buoyancy loss over the shelf (Stewart and Thompson, 2016) and of the presence of the dense flow for setting up the conditions for the cross-slope eddy flux, a further decrease in density or volume of the dense layer may lead to a decrease of the amount of energy that is transferred via instabilities to the eddy field and to a weakening of the heat transport onto the shelf. Conversely, the southward shift and strengthening of the westerly winds in the past decades (associated with the positive trend in the Southern Annular Mode; Thompson et al., 2011) have enhanced the Antarctic Circumpolar Current eddy kinetic energy (Böning et al., 2008). This, together with changes in the strength and position of the front arises from changes in the atmospheric circulation (Youngs et al., 2015), may affect cross-slope eddy advection (and consequent variability of the front) and the on-shelf transport of warm waters. It is uncertain how the eddy field will respond to those changes and whether it will affect ice shelves stability and consequently the dense water formation. In a scenario of greater variability of the front strength due to an increase in the eddy field, it is possible that the eddy field would affect the interaction between the two biological regions and, consequently, their productivity. In this case, the distribution of phytoplankton communities could be affected with consequences to higher trophic levels.

Many questions are raised by Chapters 2 and 3, but an important conclusion is that mesoscale processes are important for the variability of the frontal system and possibly for cross-slope heat transport. Some of these findings corroborate theoretical models studies, which is an essential step for improving current understanding of shelf-break dynamics. These results also reinforce the importance of a proper parametrisation of mesoscale and submesoscale processes in climate models for a correct representation of dynamics of the slope current system and an accurate prediction of future ocean conditions.

Due to the nature of the glider dataset, it can sometimes be challenging to identify which of the variables (space or time) is contributing to the observed variability. Some sampling strategies - for example the re-occupation of the same section by the glider in a short time period - were helpful in partially separating the influence of these two factors. Nonetheless, the gliders provided an extensive area coverage with a high spatial and temporal resolution. This allowed us to developed a new method to combine the many cross-slope sections and to calculate statistics of the average behaviour of the front by composing them by isobaths. This method proved very useful for this analysis and could be used in any other regions where the studied current is strongly steered by topography. The sampling strategy used in the field campaign (flying the glider aiming to reach the slope with similar angles and keeping sections' length roughly consistent) is important for applying this method.

5.1.2 The eastern Amundsen Sea

Chapter 4 explores the variability of the onshore heat transport close to the shelf-break and its possible link to the along-slope undercurrent. Cross-slope and cross-trough CTD sections provided a snapshot of the frontal system, its associated currents and the pattern of the onshore–offshore flow. They showed that the eastward undercurrent is a persistent feature that dominates the water column transport over the upper slope. Moreover, the estimated heat transport shows that, in early 2014, the eastern trough made a greater contribution to the onshore heat transport than the central trough. These estimates are important for assessing the ability of modelling studies to represent the structure and properties of the onshore flow. This snapshot is then put into a broader perspective by the analysis of the data from moorings deployed in 4 different locations for up to 4 years. The mooring data show a complex picture of intra- and interannual variability, for example, the CTD stations of early 2014 were occupied when the moored instruments at the shelf-break registered anomalously low temperatures and a rotation in the current's direction. This result emphases that one-off measurements should be interpreted with caution in this region.

The temperature transport per unit area estimated at each current meter depth (called temperature flux) showed higher energy concentrated at short time scales (days) than at monthly time scales. Several factors could contribute to the observed short-term variability, such as eddies and resonant waves. Studies have shown the influence of coastal-trapped waves in other areas of the Antarctic continental slope, such as their role in enhancing of diurnal tidal currents in the southern Weddell Sea (Semper and Darelius, 2017). In Artic fjords, the exchange driven by the propagation of coastal-trapped waves steered by the topography of across-shelf troughs can exceed both tidal and estuarine exchange (Inall et al., 2015). Even though the resonant waves do not induce a net oceanic temperature flux toward the shelf, they can influence mixing and lift/drop the thermocline (Wåhlin et al., 2016) which, at the shelf-break, will influence the amount of heat that moves onshore. More interestingly, the effect of these processes possibly varies locally because different sides of the troughs, and different troughs, show different variability patterns in short time scales and low correlation between temperature flux estimates. These results imply that, even though this is a relatively small study area, processes observed at one point can not be necessarily generalised to other parts of the shelf, and that a dense spatial sampling coverage is necessary to understand the region dynamics.

The role of the undercurrent in determining the onshore heat transport remains uncertain. On monthly time scales, the low correlation between the temperature flux of the eastward undercurrent and of the onshore flow in the central trough suggests that the influence of the undercurrent on the onshore heat transport may not be as strong as indicated by modelling and theoretical studies (Thoma et al., 2008; Jenkins et al., 2016). On interannual time scales, changes in the hydrographic properties are consistent between the upper slope and inside the trough, suggesting that, on longer time scales, these regions respond similarly to environmental forcing such as wind. However, the cold and warm periods observed do not necessarily match what would be expected in terms of increased/decreased undercurrent strength and temperature transport onto the shelf in response to changes in large-scale atmospheric forcing. For example, the marked El Ninõ conditions during 2015–2016 could have potentially led to weaker easterly winds, a possible stronger undercurrent (Jenkins et al., 2016) and, as a consequence, greater Circumpolar Deep Water (CDW) inflow onto the shelf. Instead, our results show a deeper thermocline and a cold period at the shelf-break area. One of the possible explanations for this is that the undercurrent has a weaker response to the local winds than previously suggested (Thoma et al., 2008; Jenkins et al., 2016). Understanding the wind-forced variability of the along-slope undercurrent is crucial in a scenario of positive trends in the Southern Annular Mode (Thompson et al., 2011) and increased frequency of extreme El Ninõ events (Wang et al., 2017).

Finally, the on-going effort to maintain year-round measurements at the shelf-break, despite a challenge, proved useful for evaluating short-term variability in the area. The deployment of more than one moored instruments per trough and sampling different troughs simultaneously, was important to show the non-homogeneity of the processes acting within and among troughs and was essential to evaluate them. It was also important to identify the coherence of the interannual signals on the upper-slope and within the central trough.

5.2 FUTURE WORK

There are a number of points that could be developed further from this thesis. For future work using these datasets, we suggest characterising more quantitatively the processes affecting the short-term variability, which would be beneficial to improving the performance of models in representing shelf-break processes. For example, in the Weddell Sea, the susceptibility of the flow to instabilities could be further investigated by performing linear instability analysis, which would provide parameters that could be incorporated in model parametrizations. In terms of the influence of the front on the local productivity, our work showed that the different physical characteristics onshore and offshore of the front maintain two distinct biological regions. To further test this hypothesis and to quantify the influence of the front on the productivity, an estimate of the front strength (e.g. the horizontal gradient of temperature) could be compared to the off-shore mean levels of productivity to test for correlation. Moreover, previous studies have suggested the importance of an advective mechanism for maintaining the offshore deep chlorophyll maximum in another region of the Southern Ocean (Erickson et al., 2016). The evaluation of the importance of this process in our region was hampered by limitations of the dataset; some sections did not reach far enough onshore as it would be necessary for this analysis. For future biological campaigns, we suggest that the gliders should be flown far enough onshore to sample the areas of surface chlorophyll maxima. Our understanding of the ways in which biological and physical factors influence the local krill community could by improved by the use, in future campaigns, of gliders equipped with fluorescence, backscatter sensors and echosounders. The use of remote sensing (ocean colour) could also be beneficial to this work by giving snapshots of the spatial distribution of the primary productivity for the entire study area.

In the Amundsen Sea, the association between the observed sub-inertial oscillations and resonant coastal trapped waves could be further explored. It could be improved by comparing the observations from each mooring with idealised numerical solutions of the properties of the wave for the local bathymetry, stratification and along-slope current. This would help characterise the oscillations and possibly be used to compare the importance of these processes in different troughs. On time scales shorter than 3 months, our work showed a very low correlation between the temperature flux of the along-slope undercurrent and of the onshore flow. It is possible that the correlation between these two flows is disguised by high-frequency variability and that a further investigation considering correlation on longer time scales (> 3 months) and different smoothing techniques may reveal a stronger dynamical link. We suggest a 2 month filtering window as a first estimate. This is because the energy peak at around 2 months found for the temperature flux of the along-slope current possibly indicates time scales for the movement of the front.

Some of the uncertainty in the analysis of the temperature flux variation comes from the small number of current meter instruments at each mooring. The estimates of temperature flux are calculated at each current meter depth, and its variability is shown to be more strongly correlated with the one-depth velocity time series than with temperature. However, the variability of total temperature transported onto the shelf (i.e., considering the whole section and the entire water column) is possibly strongly influenced by the depth of the thermocline, which could not be taken in consideration in our estimates because of the low number of current meter instruments at different depths. In this regard, the observed increase in the estimates of temperature transport per unit area during the last cold period (at the end of 2015) associated with stronger velocities might not be representative of the changes in transport for entire water column. For future work with this dataset, we suggest an extrapolation of the velocity measurements to all depths where in situ temperature was sampled, in addition to the estimation of a salinity algorithm based on local CTD data, which would provide estimates of temperature transport variability at more depths than the ones where current meters were placed. This could help improve the estimates for the heat transport integrated over the water column. As a suggestion for future hydrographic campaigns, the placement of instruments measuring currents and hydrography at more depths would allow the estimates to account for the water column structure and the depth of the thermocline, which would lead to a more complete picture of the variability of total temperature transport onto the shelf. In addition, we propose that the mooring deployed at the eastern trough in Amundsen Sea should be moved to a location where the main inflow could be better characterised (e.g. slightly further onshore). A procedure that could be implemented for future field campaigns is the analysis, in the field, of the currents measured from the ship instruments around the entire study area. This information could then be used to define the final position of the moored instruments.

To improve our understanding of the processes that drive the inter-annual variability observed in the hydrographic properties, it is necessary to evaluate components that can have a direct effect on the local ocean conditions, such as the variability in front position and the wind field. Attempts were made to define the position from satellite altimetry, using the Ssalto/Duacs gridded multimission altimeter product from Aviso; however it did not have high enough resolution to resolve the front. A recent study has shown the benefits of using gridded along-track SSH measurements from CryoSat-2 (Wingham et al., 2006) to track ocean features in coastal Antarctic waters, which could potentially be used to determine the front position. Alternatively, future campaigns could consider a moored array crossing the slope from the shelf break to offshore. This way, the variability of the front position could easily be tracked through time. A less expensive solution would be the deployment of gliders to repeatedly sample a cross-slope section. In this case, however, the sampling period would be shorter. Alongside the ocean measurements, the wind field could be analysed by remote sensing to check for correlations with the front.

Finally, the importance of eddies to the cross-slope transport of properties observed in the Weddell Sea is likely to be lower in the Amundsen Sea because of the difference in strength of the front and the absence of dense waters in the Amundsen Sea. However, the different nature of the datasets available for each region did not allow a direct comparison between them. To confirm this hypothesis, the deployment of gliders performing cross-slope sections in the Amundsen Sea would allow a comparison of the levels of Eddy kinetic energy (EKE) estimated in this thesis for the Weddell Sea. A sampling strategy similar to the one used in the Weddell Sea should be applied; however we suggest keeping one glider repeatedly sampling one cross-slope section while another glider travels along the slope performing cross-slope sections. This can possibly facilitate the separation between the contribution of spatial and temporal variability.

5.3 FINAL CONSIDERATIONS

Many previous studies have reported the presence and have described the hydrographic signature of the slope front all around Antarctica. Some studies have shown, for example, that the frontal system in the Weddell Sea varies with the wind stress forcing on inter-annual time scales (Youngs et al., 2015). However, little was known in terms of its variability on shorter time scales. This is in part because of the rough conditions found in the Southern Ocean (e.g. sea ice cover, low temperatures, etc) which make regular and long-term sampling difficult. In addition, the narrow structure of the front, of the current system associated with it and, as shown by this thesis, the degree of high-frequency variability requires a high spatial and temporal sampling resolution that cannot be achieved by traditional sampling methods. The high-frequency temporal variability shown in this thesis is an important result that needs to be taken into account for future studies that compare hydrographic surveys from different years and which may interpret changes as interannual variability. The use of newer technologies, as well as efforts to maintain high-frequency, long-term occupations, are shown in this thesis to help provide a more comprehensive view of the slope system and to be important tools to improve the understanding of dynamical processes in the shelf-break region.

The two regions evaluated in this work are particularly important for understanding of impacts of global warming on the ocean and cryosphere. They are also different hydrographically, which leads to different characteristics of the frontal system. However, what is noticeable from this study is that the short-term variability is significant in both regions, and that the advection of mesoscale eddies may play a role in this variability. While in the Weddell Sea baroclinic instabilities possibly fuel the eddy kinetic energy field, within the troughs of the eastern Amundsen Sea the time scales of variability suggest that barotropic resonant waves may influence the observed variability. Most of these processes are difficult to represent in global models and tend to be poorly parametrised.

This thesis characterises the short-term variability present in the Antarctic frontal system in two distinct hydrographic and dynamic regions around the Antarctic continental slope, and identifies the main processes that contribute to this variability. It also highlights the importance of properly representing these processes in modelling studies for the production of more accurate predictions of the Southern Ocean's response to future climatic changes. Moreover, this thesis contributes to the objectives of the Southern Ocean Observing System (SOOS) by giving insights on how to improve the design and implementation of future multi-disciplinary field campaigns in Antarctica to answer key outstanding questions on the slope frontal system dynamics.

References

Abelmann, A., Gersonde, R., Cortese, G., Kuhn, G., & Smetacek, V. (2006). Extensive phytoplankton blooms in the Atlantic sector of the glacial Southern Ocean. *Paleoceanography*, 21(1):1–9.

Annett, A. L., Skiba, M., Henley, S. F., Venables, H. J., Meredith, M. P., Statham, P. J., & Ganeshram, R. S. (2015). Comparative roles of upwelling and glacial iron sources in Ryder Bay, coastal western Antarctic Peninsula. *Marine Chemistry*, 176:21–33.

Ardelan, M. V., Holm-Hansen, O., Hewes, C. D., Reiss, C. S., Silva, N. S., Dulaiova, H., Steinnes, E., & Sakshaug, E. (2010). Natural iron enrichment around the Antarctic Peninsula in the Southern Ocean. *Biogeosciences Discussions*, 6(4):7481–7515.

Armitage, T. W. K., Kwok, R., Thompson, A. F., & Cunningham, G. (2018). Dynamic Topography and Sea Level Anomalies of the Southern Ocean: Variability and Teleconnections. *Journal of Geophysical Research: Oceans*, 123(1):613–630.

Arndt, J. E., Schenke, H. W., Jakobsson, M., Nitsche, F. O., Buys, G., Goleby, B., Rebesco, M., Bohoyo, F., Hong, J., Black, J., Greku, R., Udintsev, G., Barrios, F., Reynoso-Peralta, W., Taisei, M., & Wigley, R. (2013). The international bathymetric chart of the Southern Ocean (IBCSO) version 1.0-A new bathymetric compilation covering circum-Antarctic waters. *Geophysical Research Letters*, 40(12):3111–3117.

Arneborg, L., Wåhlin, A. K., Björk, G., Liljebladh, B., & Orsi, A. H. (2012). Persistent inflow of warm water onto the central Amundsen shelf. *Nature Geoscience*, 5(12):876–880.

Arrigo, K. R. (1999). Phytoplankton community structure and the drawdown of nutrients and CO_2 in the Southern Ocean. *Science*, 283(5400):365–367.

Arrigo, K. R., van Dijken, G., & Long, M. (2008a). Coastal Southern Ocean: A strong anthropogenic CO2 sink. *Geophysical Research Letters*, 35(21):1–6.

Arrigo, K. R., van Dijken, G. L., & Bushinsky, S. (2008b). Primary production in the Southern Ocean, 1997-2006. *Journal of Geophysical Research: Oceans*, 113(8):1997–2006.

Assmann, K. M., Jenkins, A., Shoosmith, D. R., Walker, D. P., Jacobs, S. S., & Nicholls,

K. W. (2013). Variability of Circumpolar Deep Water transport onto the Amundsen Sea Continental shelf through a shelf break trough. *Journal of Geophysical Research: Oceans*, 118(12):6603–6620.

Azaneu, M., Kerr, R., & Mata, M. M. (2014). Assessment of the representation of Antarctic Bottom Water properties in the ECCO2 reanalysis. *Ocean Science*, 10(6):923–946.

Azaneu, M., Kerr, R., Mata, M. M., & Garcia, C. A. E. (2013). Trends in the deep Southern Ocean (1958-2010): Implications for Antarctic Bottom Water properties and volume export. *Journal of Geophysical Research: Oceans*, 118(9):4213–4227.

Azaneu, M. V. C., Heywood, K. J., Queste, B. Y., & Thompson, A. F. (2017). Variability of the Antarctic slope current system in the northwestern Weddell Sea. *Journal of Physical Oceanography*, pages JPO–D–17–0030.1.

Baines, P. G. (2009). A model for the structure of the Antarctic Slope Front. *Deep-Sea Research Part II: Topical Studies in Oceanography*, 56(13-14):859–873.

Biddle, L. C., Kaiser, J., Heywood, K. J., Thompson, A. F., & Jenkins, A. (2015). Ocean glider observations of iceberg-enhanced biological production in the northwestern Weddell Sea. *Geophysical Research Letters*, 42(2):459–465.

Böning, C. W., Dispert, A., Visbeck, M., Rintoul, S. R., & Schwarzkopf, F. U. (2008). The response of the antarctic circumpolar current to recent climate change. *Nature Geoscience*, 1(12):864–869.

Boss, E. & Pegau, W. S. (2001). Relationship of light scattering at an angle in the backward direction to the backscattering coefficient. *Applied optics*, 40(30):5503–7.

Boyd, A. P. W., Jickells, T., Law, C. S., Blain, S., Boyle, E. A., Buesseler, K. O., Coale, K. H., Cullen, J. J., Baar, H. J. W. D., Follows, M., Harvey, M., Lancelot, C., Levasseur, M., Pollard, R., Rivkin, R. B., Sarmiento, J., Schoemann, V., Smetacek, V., Takeda, S., Turner, S., Watson, A. J., & Baar, H. W. D. (2007). Mesoscale Iron Enrichment Experiments 1993-205: Synthesis and Future Directions. *Science*, 315(5812):612–617.

Boyd, P. W. (2002). Environmental factors controlling phytoplankton processes in the Southern Ocean. *Journal of Phycology*, 38(5):844–861.

Cai, W., Borlace, S., Lengaigne, M., Van Rensch, P., Collins, M., Vecchi, G., Timmermann, A., Santoso, A., Mcphaden, M. J., Wu, L., England, M. H., Wang, G., Guilyardi, E., & Jin, F. F. (2014). Increasing frequency of extreme El Niño events due to greenhouse warming. *Nature Climate Change*, 4(2):111–116.

Carmack, E. C. & Foster, T. D. (1975). On the flow of water out of the Weddell Sea. *Deep Sea Research*, 22(11):711–724.

Caspel, M. V., Schröder, M., Huhn, O., & Hellmer, H. (2015). Precursors of Antarctic Bottom Water formed on the continental shelf off Larsen Ice Shelf. *Deep Sea Research Part I: Oceanographic Research Papers*, 99:1–9.

Chavanne, C. P., Heywood, K. J., Nicholls, K. W., & Fer, I. (2010). Observations of the Antarctic Slope Undercurrent in the southeastern Weddell Sea. *Geophysical Research Letters*, 37(13).

Church, J., Clark, P., Cazenave, a., Gregory, J., Jevrejeva, S., Levermann, a., Merrifield, M., Milne, G., Nerem, R., Nunn, P., a.J. Payne, Pfeffer, W., Stammer, D., & a.S. Unnikrishnan (2013). Sea level change. *Climate Change 2013: The Physical Science Basis. Contribution of Working Group I to the Fifth Assessment Report of the Intergovernmental Panel on Climate Change*, pages 1137–1216.

de Baar, H. J., Bathmannt, U., Smetacek, V., Löscher, B. M., & Veth, C. (1995). Importance of iron for plankton blooms and carbon dioxide drawdown in the Southern Ocean.

De Jong, J., Schoemann, V., Lannuzel, D., Croot, P., De Baar, H., & Tison, J.-L. (2012). Natural iron fertilization of the Atlantic sector of the Southern Ocean by continental shelf sources of the Antarctic Peninsula. *Journal of Geophysical Research*, 117(G1):25pp.

Deppeler, S. L. & Davidson, A. T. (2017). Southern Ocean Phytoplankton in a Changing Climate. *Frontiers in Marine Science*, 4(February):40.

DeVries, T., Holzer, M., & Primeau, F. (2017). Recent increase in oceanic carbon uptake driven by weaker upper-ocean overturning. *Nature*, 542(7640):215–218.

Dinniman, M. S., Klinck, J. M., & Smith, W. O. (2011). A model study of Circumpolar Deep Water on the West Antarctic Peninsula and Ross Sea continental shelves. *Deep Sea Research Part II: Topical Studies in Oceanography*, 58(13-16):1508–1523.

DiTullio, G. R. & Smith, W. O. (1996). Spatial patterns in phytoplankton biomass and pigment distributions in the Ross Sea. *Journal of Geophysical Research: Oceans*, 101(C8):18467–18477.

Dong, S., Sprintall, J., Gille, S. T., & Talley, L. (2008). Southern ocean mixed-layer depth from Argo float profiles. *Journal of Geophysical Research: Oceans*, 113(6):1–12.

Dufour, C. O., Sommer, L. L., Zika, J. D., Gehlen, M., Orr, J. C., Mathiot, P., & Barnier, B. (2012). Standing and transient eddies in the response of the Southern Ocean meridional overturning to the Southern annular mode. *Journal of Climate*, 25(20):6958–6974.

Duprat, L. P. A. M., Bigg, G. R., & Wilton, D. J. (2016). Enhanced Southern Ocean marine productivity due to fertilization by giant icebergs. *Nature Geoscience*, 9(3):219–221.

Dutrieux, P. (2014). Strong Sensitivity of Pine Island Ice-Shelf. *Science*, 174(January):174–179.

Erickson, Z. K., Thompson, A. F., Cassar, N., Sprintall, J., & Mazloff, M. R. (2016). An advective mechanism for deep chlorophyll maxima formation in southern Drake Passage. *Geophysical Research Letters*, 43(10):846–855.

Eriksen, C. C., Osse, T. J., Light, R. D., Wen, T., Lehman, T. W., Sabin, P. L., Ballard, J. W., & Chiodi, A. M. (2001). Seaglider: A long-range autonomous underwater vehicle for oceanographic research. *IEEE Journal of Oceanic Engineering*, 26(4):424–436.

Fahrbach, E., Hoppema, M., Rohardt, G., Boebel, O., Klatt, O., & Wisotzki, A. (2011). Warming of deep and abyssal water masses along the Greenwich meridian on decadal time scales: The Weddell gyre as a heat buffer. *Deep-Sea Research Part II: Topical Studies in Oceanography*, 58(25-26):2509–2523.

Farneti, R., Delworth, T. L., Rosati, A. J., Griffies, S. M., & Zeng, F. (2010). The Role of Mesoscale Eddies in the Rectification of the Southern Ocean Response to Climate Change. *Journal of Physical Oceanography*, 40(7):1539–1557.

Ferrari, R. & Nikurashin, M. (2010). Suppression of Eddy Diffusivity across Jets in the Southern Ocean. *Journal of Physical Oceanography*, 40(7):1501–1519.

Fielding, S., Cossio, A., Cox, M., Reiss, C., Skaret, G., Demer, D., Watkins, J., & Zhao, X. (2016). A condensed history and document of the method used by CCAMLR to estimate krill biomass (B0) in 2010. Technical report, Working Group on Ecosystem Monitoring and Management.

Foldvik, A., Gammelsrød, T., & Tørresen, T. (1985). Circulation and Water Masses on the Southern Weddell Sea Shelf. *Antarctic Research Series*, 43:5–20.

Foster, T. D., Foldvik, A., & Middleton, J. H. (1987). Mixing and bottom water formation in the shelf break region of the southern Weddell Sea. *Deep Sea Research Part A, Oceanographic Research Papers*, 34(11):1771–1794.

Frajka-Williams, E., Eriksen, C. C., Rhines, P. B., & Harcourt, R. R. (2011). Determining vertical water velocities from Seaglider. *Journal of Atmospheric and Oceanic Technology*, 28(12):1641–1656.

Fretwell, P., Pritchard, H. D., Vaughan, D. G., Bamber, J. L., Barrand, N. E., Bell, R., Bianchi, C., Bingham, R. G., Blankenship, D. D., Casassa, G., Catania, G., Callens, D., Conway, H., Cook, A. J., Corr, H. F., Damaske, D., Damm, V., Ferraccioli, F., Forsberg, R., Fujita, S., Gim, Y., Gogineni, P., Griggs, J. A., Hindmarsh, R. C., Holmlund, P., Holt, J. W., Jacobel, R. W., Jenkins, A., Jokat, W., Jordan, T., King, E. C., Kohler, J., Krabill, W., Riger-Kusk, M., Langley, K. A., Leitchenkov, G., Leuschen, C., Luyendyk, B. P., Matsuoka, K., Mouginot, J., Nitsche, F. O., Nogi, Y., Nost, O. A., Popov, S. V., Rignot, E., Rippin, D. M., Rivera, A., Roberts, J., Ross, N., Siegert, M. J., Smith, A. M., Steinhage, D., Studinger, M., Sun, B., Tinto, B. K., Welch, B. C., Wilson, D., Young, D. A., Xiangbin, C., & Zirizzotti, A. (2013). Bedmap2: Improved ice bed, surface and thickness datasets for Antarctica. *Cryosphere*, 7(1):375–393.

Gardner, W., Richardson, M., & Jr, W. S. (2000). Seasonal patterns of water column particulate organic carbon and fluxes in the Ross Sea, Antarctica. *Deep Sea Research II*, 47:3423–3449.

Gill, A. E. (1973). Circulation and bottom water production in the Weddell Sea. *Deep-Sea Research and Oceanographic Abstracts*, 20(2):111–140.

Gordon, A., Georgi, D., & Taylor, H. (1977). Antarctic Polar Front Zone in the Western Scotia Sea - Summer 1975. *Journal of Physical Oceanography*, 7(3):309–328.

Gordon, A. L., Huber, B., McKee, D., & Visbeck, M. (2010). A seasonal cycle in the export of bottom water from the Weddell Sea. *Nature Geoscience*, 3(8):551–556.

Graham, J. a., Heywood, K. J., Chavanne, C. P., & Holland, P. R. (2013). Seasonal variability of water masses and transport on the Antarctic continental shelf and slope in the southeastern Weddell Sea. *Journal of Geophysical Research: Oceans*, 118(4):2201–2214.

Ha, H. K., Wåhlin, A. K., Kim, T. W., Lee, S. H., Lee, J. H., Lee, H. J., Hong, C. S., Arneborg, L., Björk, G., & Kalén, O. (2014). Circulation and Modification of Warm Deep Water on the Central Amundsen Shelf. *Journal of Physical Oceanography*, 44(5):1493–1501.

Haine, T. W. N. & Marshall, J. (1998). Gravitational, Symmetric, and Baroclinic Instability of the Ocean Mixed Layer. *Journal of Physical Oceanography*, 28(4):634–

658.

Haran, T., Bohlander, J., Scambos, T. A., Painter, T., & Fahnestock, M. A. (2005). MODIS mosaic of Antarctica (MOA) image map. *Digital Media*, (Boulder, Colorado USA: National Snow and Ice Data Cente).

Hewes, C., Reiss, C., Kahru, M., Mitchell, B., & Holm-Hansen, O. (2008). Control of phytoplankton biomass by dilution and mixed layer depth in the western Weddell-Scotia Confluence. *Marine Ecology Progress Series*, 366:15–29.

Hewitt, R. P., Watkins, J., Naganobu, M., Sushin, V., Brierley, A. S., Demer, D., Kasatkina, S., Takao, Y., Goss, C., Malyshko, A., Brandon, M., Kawaguchi, S., Siegel, V., Trathan, P., Emery, J., Everson, I., & Miller, D. (2004). Biomass of Antarctic krill in the Scotia Sea in January/February 2000 and its use in revising an estimate of precautionary yield. *Deep-Sea Research Part II: Topical Studies in Oceanography*, 51(12-13 SPEC.ISS.):1215–1236.

Heywood, K., Biddle, L., Boehme, L., Dutrieux, P., Fedak, M., Jenkins, A., Jones, R., Kaiser, J., Mallett, H., Naveira Garabato, A., Renfrew, I., Stevens, D., & Webber, B. (2016). Between the Devil and the Deep Blue Sea: The Role of the Amundsen Sea Continental Shelf in Exchanges Between Ocean and Ice Shelves. *Oceanography*, 29(4):118–129.

Heywood, K. & King, B. (2002). Water masses and baroclinic transports in the South Atlantic and southern oceans. *Journal of Marine Research*, 60(5):639–676.

Heywood, K. J., Locarnini, R. A., Frew, R. D., Dennis, P. F., & King, B. A. (1998). Transport and water masses of the Antarctic Slope Front system in the eastern Weddell Sea. In: *Ocean, Ice, and Atmosphere: Interactions at the Antarctic Continental Margin, Antarctic Research Series*, S. S. Jacobs & R. F. Weiss, ed., volume 75 of *Antarctic Research Series*, pages 203–214. American Geophysical Union.

Heywood, K. J., Naveira Garabato, A. C., Stevens, D. P., & Muench, R. D. (2004). On the fate of the Antarctic Slope Front and the origin of the Weddell Front. *Journal of Geophysical Research C: Oceans*, 109(6):C06021.

Heywood, K. J., Schmidtko, S., Heuzé, C., Kaiser, J., Jickells, T., Queste, B. Y., Stevens, D. P., Wadley, M., Thompson, A. F., Fielding, S., Guihen, D., Creed, E., Ridley, J. K., & Smith, W. (2014). Ocean processes at the Antarctic continental slope. *Philosophical Transactions of the Royal Society A: Mathematical, Physical and*

Engineering Sciences, 372:1–11.

Holm-Hansen, O., Naganobu, M., Kawaguchi, S., Kameda, T., Krasovski, I., Tchernyshkov, P., Priddle, J., Korb, R., Brandon, M., Demer, D., Hewitt, R. P., Kahru, M., & Hewes, C. D. (2004). Factors influencing the distribution, biomass, and productivity of phytoplankton in the Scotia Sea and adjoining waters. *Deep-Sea Research Part II: Topical Studies in Oceanography*, 51(12-13 SPEC.ISS.):1333–1350.

Hosegood, P., Bonnin, J., & van Haren, H. (2004). Solibore-induced sediment resuspension in the Faeroe-Shetland channel. *Geophysical Research Letters*, 31(9):2–5.

Huhn, O., Hellmer, H. H., Rhein, M., Rodehacke, C., Roether, W., Schodlok, M. P., & Schröder, M. (2008). Evidence of deep- and bottom-water formation in the western Weddell Sea. *Deep-Sea Research Part II: Topical Studies in Oceanography*, 55(8-9):1098–1116.

Inall, M. E., Nilsen, F., Cottier, F. R., & Daae, R. (2015). Shelf/fjord exchange driven by coastal-trapped waves in the Arctic. *Journal of Geophysical Research: Oceans*, 120(12):8283–8303.

Isachsen, P. E. (2011). Baroclinic instability and eddy tracer transport across sloping bottom topography: How well does a modified Eady model do in primitive equation simulations? *Ocean Modelling*, 39(1-2):183–199.

Jacobs, S. S. (1991). On the nature and significance of the Antarctic Slope Front. *Marine Chemistry*, 35(1-4):9–24.

Jacobs, S. S., Jenkins, A., Giulivi, C. F., & Dutrieux, P. (2011). Stronger ocean circulation and increased melting under Pine Island Glacier ice shelf. *Nature Geoscience*, 4(8):519–523.

Jenkins, A., Dutrieux, P., Jacobs, S., Steig, E., Gudmundsson, H., Smith, J., & Heywood, K. (2016). Decadal Ocean Forcing and Antarctic Ice Sheet Response: Lessons from the Amundsen Sea. *Oceanography*, 29(4):106–117.

Jenkins, A., Dutrieux, P., Jacobs, S. S., McPhail, S. D., Perrett, J. R., Webb, A. T., & White, D. (2010). Observations beneath Pine Island Glacier in West Antarctica and implications for its retreat. *Nature Geoscience*, 3(7):468–472.

JGOFS (1996). PROTOCOLS FOR THE JOINT GLOBAL OCEAN FLUX STUDY (JGOFS) CORE MEASUREMENTS. Technical report, IOC SCOR.

Johns, W. E. (1988). One-dimensional baroclinically unstable waves on the Gulf

Stream potential vorticity gradient near Cape Hatteras. *Dynamics of Atmospheres and Oceans*, 11:323–350.

Jullion, L., Garabato, A. C. N., Bacon, S., Meredith, M. P., Brown, P. J., Torres-Valdés, S., Speer, K. G., Holland, P. R., Dong, J., Bakker, D., Hoppema, M., Loose, B., Venables, H. J., Jenkins, W. J., Messias, M. J., & Fahrbach, E. (2014). The contribution of the Weddell Gyre to the lower limb of the Global Overturning Circulation. *Journal of Geophysical Research: Oceans*, 119(6):3357–3377.

Kaufman, D. E., Friedrichs, M. A. M., Smith, W. O., Queste, B. Y., & Heywood, K. J. (2014). Biogeochemical variability in the southern Ross Sea as observed by a glider deployment. *Deep-Sea Research Part I: Oceanographic Research Papers*, 92:93–106.

Kim, C. S., Kim, T. W., Cho, K. H., Ha, H. K., Lee, S. H., Kim, H. C., & Lee, J. H. (2016). Variability of the Antarctic Coastal Current in the Amundsen Sea. *Estuarine, Coastal and Shelf Science*, 181:123–133.

Kim, T. W., Ha, H. K., Wåhlin, A. K., Lee, S. H., Kim, C. S., Lee, J. H., & Cho, Y. K. (2017). Is Ekman pumping responsible for the seasonal variation of warm circumpolar deep water in the Amundsen Sea? *Continental Shelf Research*, 132(July 2016):38–48.

Kimura, S., Jenkins, A., Regan, H., Holland, P. R., Assmann, K. M., Whitt, D., Van Wessem, M., van de Berg, W. J., Reijmer, C. H., & Dutrieux, P. (2017). Oceanographic Controls on the Variability of Ice-Shelf Basal Melting and Circulation of Glacial Meltwater in the Amundsen Sea Embayment, Antarctica. *Journal of Geophysical Research: Oceans*, page Accepted.

Konrad, H., Shepherd, A., Gilbert, L., Hogg, A. E., McMillan, M., Muir, A., & Slater, T. (2018). Net retreat of Antarctic glacier grounding lines. *Nature Geoscience*, 11(4):258–262.

Kustka, A. B., Kohut, J. T., White, A. E., Lam, P. J., Milligan, A. J., Dinniman, M. S., Mack, S., Hunter, E., Hiscock, M. R., Smith, W. O., & Measures, C. I. (2015). The roles of MCDW and deep water iron supply in sustaining a recurrent phytoplankton bloom on central Pennell Bank (Ross Sea). *Deep-Sea Research Part I: Oceanographic Research Papers*, 105:171–185.

Lee, M. M. & Coward, A. (2003). Eddy mass transport for the Southern Ocean in an eddy-permitting global ocean model. *Ocean Modelling*, 5(3):249–266.

Lumpkin, R. & Speer, K. (2007). Global Ocean Meridional Overturning. *Journal of Physical Oceanography*, 37(10):2550–2562.

Mallett, H., Boehme, L., Fedak, M., K.J., H., Stevens, D., & Roquet, F. (2018). Variation in the distribution and properties of Circumpolar Deep Water in the eastern Amundsen Sea, on seasonal timescales, using seal-borne tags. *Geophysical Research Letters*, 0(ja):1–13.

Marshall, J. & Radko, T. (2003). Residual-Mean Solutions for the Antarctic Circumpolar Current and Its Associated Overturning Circulation. *Journal of Physical Oceanography*, 33(11):2341–2354.

Martin, J. H., Gordon, R. M., & Fitzwater, S. E. (1990). Iron in Antarctic waters. *Nature*, 345(2):156–158.

Mazloff, M. R., Heimbach, P., & Wunsch, C. (2010). An Eddy-Permitting Southern Ocean State Estimate. *Journal of Physical Oceanography*, 40(5):880–899.

McGillicuddy, D. J., Sedwick, P. N., Dinniman, M. S., Arrigo, K. R., Bibby, T. S., Greenan, B. J. W., Hofmann, E. E., Klinck, J. M., Smith, W. O., Mack, S. L., Marsay, C. M., Sohst, B. M., & van Dijken, G. L. (2015). Iron supply and demand in an Antarctic shelf ecosystem. *Geophysical Research Letters*, 42(19):8088–8097.

Meijers, A. J. S., Meredith, M. P., Abrahamsen, E. P., Morales Maqueda, M. A., Jones, D. C., & Naveira Garabato, A. C. (2016). Wind-driven export of Weddell Sea slope water. *Journal of Geophysical Research: Oceans*, 121(10):7530–7546.

Mendes, C. R. B., de Souza, M. S., Garcia, V. M. T., Leal, M. C., Brotas, V., & Garcia, C. A. E. (2012). Dynamics of phytoplankton communities during late summer around the tip of the Antarctic Peninsula. *Deep Sea Research Part I: Oceanographic Research Papers*, 65:1–14.

Moisan, T. A. & Mitchell, B. G. (1999). Photophysiological acclimation of Phaeocystis antarctica Karsten under light limitation. *Limnology and Oceanography*, 44(2):247–258.

Moline, M. A., Claustre, H., Frazer, T. K., Schofield, O., & Vernet, M. (2004). Alteration of the food web along the Antarctic Peninsula in response to a regional warming trend. *Global Change Biology*, 10(12):1973–1980.

Moore, J. K. & Abbott, M. R. (2000). Phytoplankton chlorophyll distributions and primary production in the Southern Ocean. *Journal of Geophysical Research*, 105(C12):28709.

Morel, A. (1974). Optical properties of pure water and pure sea water. *Optical aspects of oceanography*, 1:1–24.

Mouginot, J., Rignot, E., & Scheuchl, B. (2014). Sustained increase in ice discharge from the Amundsen Sea Embayment, West Antarctica, from 1973 to 2013. *Geophysical Research Letters*, 41(5):1576–1584.

Muench, R. D. & Gordon, A. L. (1995). Circulation and transport of water along the western Weddell Sea margin. *Journal of Geophysical Research*, 100(C9):18503.

Müller, P. (1995). Ertel's potential vorticity theorem in physical oceanography. *Reviews of Geophysics*, 33(1):67.

Nakayama, Y., Schröder, M., & Hellmer, H. H. (2013). From circumpolar deep water to the glacial meltwater plume on the eastern Amundsen Shelf. *Deep-Sea Research Part I: Oceanographic Research Papers*, 77:50–62.

Naveira Garabato, A. C. (2012). A perspective on the future of physical oceanography. *Philosophical Transactions of the Royal Society A: Mathematical, Physical and Engineering Sciences*, 370(1980):5480–5511.

Naveira Garabato, A. C., McDonagh, E. L., Stevens, D. P., Heywood, K. J., & Sanders, R. J. (2002). On the export of Antarctic Bottom Water from the Weddell Sea. *Deep Sea Research Part II: Topical Studies in Oceanography*, 49(21):4715–4742.

Naveira Garabato, A. C., Polzin, K. L., King, B. A., Heywood, K. J., & Visbeck, M. (2004). Widespread intense turbulent mixing in the Southern Ocean. *Science (New York, N.Y.)*, 303(5655):210–3.

Nicholls, K. W., Østerhus, S., Makinson, K., Gammelsrød, T., & Fahrbach, E. (2009). Ice-ocean processes over the continental shelf of the southern Weddell Sea, Antarctica: A review. *Reviews of Geophysics*, 47(3):RG3003.

Nøst, O. A., Biuw, M., Tverberg, V., Lydersen, C., Hattermann, T., Zhou, Q., Smedsrud, L. H., & Kovacs, K. M. (2011). Eddy overturning of the Antarctic Slope Front controls glacial melting in the Eastern Weddell Sea. *Journal of Geophysical Research*, 116(C11):C11014.

Orsi, A. H., Johnson, G. C., & Bullister, J. L. (1999). Circulation, mixing, and production of Antarctic Bottom Water. *Progress in Oceanography*, 43(1):55–109.

Orsi, A. H., Nowlin, W. D., & Whitworth, T. (1993). On the circulation and stratification of the Weddell Gyre.

Orsi, A. H., Whitworth, T., & Nowlin, W. D. (1995). On the meridional extent and fronts of the Antarctic Circumpolar Current. *Deep-Sea Research Part I*, 42(5):641–673.

Padman, L., Fricker, H. A., Coleman, R., Howard, S., & Erofeeva, L. (2002). A new tide model for the Antarctic ice shelves and seas. *Annals of Glaciology*, 34(1):247–254.

Palmer, M., Gomis, D., Flexas, M. d. M., Jordà, G., Jullion, L., Tsubouchi, T., & Naveira Garabato, A. C. (2012). Water mass pathways and transports over the South Scotia Ridge west of 50W. *Deep Sea Research Part I: Oceanographic Research Papers*, 59:8–24.

Paolo, F. S., Fricker, H. A., & Padman, L. (2015). Volume loss from Antarctic ice shelves is accelerating. *Science*, 348(6232):327–331.

Pedlosky, J. (1964). The Stability of Currents in the Atmosphere and the Ocean: Part I. *Journal of Atmospheric Sciences*, 21:201–219.

Pollard, R. T., Lucas, M. I., & Read, J. F. (2002). Physical controls on biogeochemical zonation in the Southern Ocean. *Deep-Sea Research Part II: Topical Studies in Oceanography*, 49(16):3289–3305.

Porter, M., Inall, M. E., Hopkins, J., Palmer, M. R., Dale, A. C., Aleynik, D., Barth, J. A., Mahaffey, C., & Smeed, D. A. (2016). Glider observations of enhanced deep water upwelling at a shelf break canyon: A mechanism for cross-slope carbon and nutrient exchange. *Journal of Geophysical Research: Oceans*, 121(10):7575–7588.

Prézelin, B. B., Hofmann, E. E., Mengelt, C., & Klinck, J. M. (2000). The linkage between Upper Circumpolar Deep Water (UCDW) and phytoplankton assemblages on the west Antarctic Peninsula continental shelf. *Journal of Marine Research*, 58(2):165–202.

Pritchard, H. D., Ligtenberg, S. R., Fricker, H. A., Vaughan, D. G., Van Den Broeke, M. R., & Padman, L. (2012). Antarctic ice-sheet loss driven by basal melting of ice shelves. *Nature*, 484(7395):502–505.

Purkey, S. G. & Johnson, G. C. (2013). Antarctic bottom water warming and freshening: Contributions to sea level rise, ocean freshwater budgets, and global heat gain. *Journal of Climate*, 26(16):6105–6122.

Queste, B. (2013). *Hydrographic observations of oxygen and related physical variables in the North Sea and western Ross Sea Polynya*. PhD thesis, University of East Anglia.

Rahmstorf, S. (2003). Thermohaline circulation: The current climate. *Nature*, 421(6924):699.

Renner, A. H. H., Thorpe, S. E., Heywood, K. J., Murphy, E. J., Watkins, J. L., & Meredith, M. P. (2012). Advective pathways near the tip of the Antarctic Peninsula: Trends, variability and ecosystem implications. *Deep-Sea Research Part I: Oceanographic*

Research Papers, 63:91–101.

Rignot, E., Casassa, G., Gogineni, P., Krabill, W., Rivera, A., & Thomas, R. (2004). Accelerated ice discharge from the Antarctic Peninsula following the collapse of Larsen B ice shelf. *Geophysical Research Letters*, 31(18):2–5.

Rignot, E., Mouginot, J., Morlighem, M., Seroussi, H., & Scheuchl, B. (2014). Widespread, rapid grounding line retreat of Pine Island, Thwaites, Smith, and Kohler glaciers, West Antarctica, from 1992 to 2011. *Geophysical Research Letters*, 41(10):3502–3509.

Rintoul, S. R. (1998). On the origin and influence of Adélie land bottom water. *Ocean, ice, and atmosphere: interactions at the Antarctic Continental Margin, Antarctic Research Series*, 75:151–171.

Rintoul, S. R. (2018). The global influence of localized dynamics in the Southern Ocean. *Nature*, 558(7709):209–218.

Ruan, X. & Thompson, A. F. (2016). Bottom Boundary Potential Vorticity Injection from an Oscillating Flow: A PV Pump. *Journal of Physical Oceanography*, 46(11):3509–3526.

Ruddick, B. (1983). A practical indicator of the stability of the water column to double-diffusive activity. *Deep Sea Research Part A, Oceanographic Research Papers*, 30(10):1105–1107.

Rudnick, D. L. & Cole, S. T. (2011). On sampling the ocean using underwater gliders. *Journal of Geophysical Research: Oceans*, 116(8):1–12.

Schmidtko, S., Heywood, K. J., Thompson, A. F., & Aoki, S. (2014). Multidecadal warming of Antarctic waters. *Science*, 346(6214):1227–1231.

Schodlok, M. P., Menemenlis, D., Rignot, E., & Studinger, M. (2012). Sensitivity of the ice-shelf/ocean system to the sub-ice-shelf cavity shape measured by nasa icebridge in pine island glacier, west antarctica. *Annals of Glaciology*, 53(60):156–162.

Schofield, O., Glenn, S., & Moline, M. (2013). The Robot Ocean Network. *American Scientist*, 101(6):434.

Schwarz, J. N. & Schodlok, M. P. (2009). Impact of drifting icebergs on surface phytoplankton biomass in the Southern Ocean: Ocean colour remote sensing and in situ iceberg tracking. *Deep-Sea Research Part I: Oceanographic Research Papers*, 56(10):1727–1741.

Semper, S. & Darelius, E. (2017). Seasonal resonance of diurnal coastal trapped waves in the southern Weddell Sea, Antarctica. *Ocean Science*, 13(1):77–93.

Shepherd, A., Fricker, H. A., & Farrell, S. L. (2018). Trends and connections across the Antarctic cryosphere. *Nature*, 558(7709):223–232.

Shepherd, A., Wingham, D., & Rignot, E. (2004). Warm ocean is eroding West Antarctic Ice Sheet. *Geophysical Research Letters*, 31(23):1–4.

Silvano, A., Rintoul, S., & Herraiz-Borreguero, L. (2016). Ocean-Ice Shelf Interaction in East Antarctica. *Oceanography*, 29(4):130–143.

Simpson, J. H. & McCandliss, R. R. (2013). "the Ekman Drain": A conduit to the deep ocean for shelf material Topical Collection on Physics of Estuaries and Coastal Seas 2012. *Ocean Dynamics*, 63(9-10):1063–1072.

Smetacek, V. & Nicol, S. (2005). Polar ocean ecosystems in a changing world.

Smith, K. S. (2007). The geography of linear baroclinic instability in Earth's oceans. *Journal of Marine Research*, 65(5):655–683.

Smith, W. O. J., Ainley, D. G., & Arrigo, K. R. (2014). The Oceanography and Ecology of the Ross Sea. *Annual Review of Marine Science*, 6(August):469–87.

Smith, Walker O., J., Marra, J., Hiscock, M. R., & Barber, R. T. (2000). The seasonal cycle of phytoplankton biomass and primary productivity in the Ross Sea, Antarctica. *Deep Sea Research Part II: Topical Studies in Oceanography*, 47(15–16):3119–3140.

Sokolov, S. & Rintoul, S. R. (2007). On the relationship between fronts of the Antarctic Circumpolar Current and surface chlorophyll concentrations in the Southern Ocean. *Journal of Geophysical Research: Oceans*, 112(7):1–17.

St-Laurent, P., Klinck, J. M., & Dinniman, M. S. (2013). On the Role of Coastal Troughs in the Circulation of Warm Circumpolar Deep Water on Antarctic Shelves. *Journal of Physical Oceanography*, 43(1):51–64.

St-Laurent, P., Klinck, J. M., & Dinniman, M. S. (2015). Impact of local winter cooling on the melt of Pine Island Glacier, Antarctica. *Journal of Geophysical Research: Oceans*, 120(10):6718–6732.

Steig, E. J., Ding, Q., Battisti, D. S., & Jenkins, A. (2012). Tropical forcing of circumpolar deep water inflow and outlet glacier thinning in the amundsen sea embayment, west antarctica. *Annals of Glaciology*, 53(60):19–28.

Stern, A., Nadeau, L.-P., & Holland, D. (2015). Instability and Mixing of Zonal Jets along an Idealized Continental Shelf Break. *Journal of Physical Oceanography*, 45(9):2315–2338.

Stewart, A. L. & Thompson, A. F. (2013). Connecting Antarctic Cross-Slope Exchange with Southern Ocean Overturning. *Journal of Physical Oceanography*, 43(7):1453–1471.

Stewart, A. L. & Thompson, A. F. (2015). Eddy-mediated transport of warm Circumpolar Deep Water across the Antarctic Shelf Break. *Geophysical Research Letters*, 42(2):432–440.

Stewart, A. L. & Thompson, A. F. (2016). Eddy Generation and Jet Formation via Dense Water Outflows across the Antarctic Continental Slope. *Journal of Physical Oceanography*, 46(12):3729–3750.

Su, Z., Stewart, A. L., & Thompson, A. F. (2014). An Idealized Model of Weddell Gyre Export Variability. *Journal of Physical Oceanography*, 44(6):1671–1688.

Sutterley, T. C., Velicogna, I., Rignot, E., Mouginot, J., Flament, T., Van Den Broeke, M. R., Van Wessem, J. M., & Reijmer, C. H. (2014). Mass loss of the Amundsen Sea Embayment of West Antarctica from four independent techniques. *Geophysical Research Letters*, 41(23):8421–8428.

Talley, L. (2013). Closure of the Global Overturning Circulation Through the Indian, Pacific, and Southern Oceans: Schematics and Transports. *Oceanography*, 26(1):80–97.

Tanaka, K. & Akitomo, K. (2001). Baroclinic instability of density current along a sloping bottom and the associated transport process. *Journal of Geophysical Research: Oceans*, 106(C2):2621–2638.

Thoma, M., Jenkins, A., Holland, D., & Jacobs, S. (2008). Modelling Circumpolar Deep Water intrusions on the Amundsen Sea continental shelf, Antarctica. *Geophysical Research Letters*, 35(18):2–7.

Thomas, L. N., Taylor, J. R., Ferrari, R., & Joyce, T. M. (2013). Symmetric instability in the Gulf Stream. *Deep Sea Research Part II: Topical Studies in Oceanography*, 91:96–110.

Thompson, A. F. (2008). The atmospheric ocean: Eddies and jets in the Antarctic Circumpolar Current. *Philosophical Transactions of the Royal Society A: Mathematical, Physical and Engineering Sciences*, 366(1885):4529–4541.

Thompson, A. F. & Heywood, K. J. (2008). Frontal structure and transport in the northwestern Weddell Sea. *Deep Sea Research Part I: Oceanographic Research*

Papers, 55(10):1229–1251.

Thompson, A. F., Heywood, K. J., Schmidtko, S., & Stewart, A. L. (2014). Eddy transport as a key component of the Antarctic overturning circulation. *Nature Geoscience*, 7(12):879–884.

Thompson, A. F., Heywood, K. J., Thorpe, S. E., Renner, A. H. H., & Trasviña, A. (2009). Surface Circulation at the Tip of the Antarctic Peninsula from Drifters. *Journal of Physical Oceanography*, 39(1):3–26.

Thompson, A. F. & Youngs, M. K. (2013). Surface exchange between the Weddell and Scotia Seas. *Geophysical Research Letters*, 40(22):5920–5925.

Thompson, D. W. J., Solomon, S., Kushner, P. J., England, M. H., Grise, K. M., & Karoly, D. J. (2011). Signatures of the Antarctic ozone hole in Southern Hemisphere surface climate change. *Nature Geoscience*, 4(11):741–749.

Thorpe, S. E., Heywood, K. J., Stevens, D. P., & Brandon, M. A. (2004). Tracking passive drifters in a high resolution ocean model: Implications for interannual variability of larval krill transport to South Georgia. *Deep-Sea Research Part I: Oceanographic Research Papers*, 51(7):909–920.

Todd, R. E., Owens, W. B., & Rudnick, D. L. (2016). Potential Vorticity Structure in the North Atlantic Western Boundary Current from Underwater Glider Observations. *Journal of Physical Oceanography*, 46(1):327–348.

Torrence, C. & Compo, G. P. (1998). A Practical Guide to Wavelet Analysis. *Bulletin of the American Meteorological Society*, 79(1):61–78.

Trevor J. McDougall & Barker, P. M. (2011). *Getting started with TEOS-10 and the Gibbs Seawater (GSW) Oceanographic Toolbox*. SCOR/IAPSO WG127.

Vallis, G. K. & Maltrud, M. E. (1993). Generation of Mean Flows and Jets on a Beta Plane and over Topography.

Wadley, M. R., Jickells, T. D., & Heywood, K. J. (2014). The role of iron sources and transport for Southern Ocean productivity. *Deep-Sea Research Part I: Oceanographic Research Papers*, 87:82–94.

Wåhlin, A. K., Kalén, O., Assmann, K. M., Darelius, E., Ha, H. K., Kim, T. W., & Lee, S. H. (2016). Subinertial Oscillations on the Amundsen Sea Shelf, Antarctica. *Journal of Physical Oceanography*, 46(9):2573–2582.

Wåhlin, A. K., Muench, R. D., Arneborg, L., Björk, G., Ha, H. K., Lee, S. H., & Alsén, H. (2012). Some Implications of Ekman Layer Dynamics for Cross-Shelf Exchange in the Amundsen Sea. *Journal of Physical Oceanography*, 42(9):1461–1474.

Walker, D. P., Brandon, M. A., Jenkins, A., Allen, J. T., Dowdeswell, J. A., & Evans, J. (2007). Oceanic heat transport onto the Amundsen Sea shelf through a submarine glacial trough. *Geophysical Research Letters*, 34(2):2–5.

Walker, D. P., Jenkins, A., Assmann, K. M., Shoosmith, D. R., & Brandon, M. a. (2013). Oceanographic observations at the shelf break of the Amundsen Sea, Antarctica. *Journal of Geophysical Research: Oceans*, 118(6):2906–2918.

Wang, G., Cai, W., Gan, B., Wu, L., Santoso, A., Lin, X., Chen, Z., & McPhaden, M. J. (2017). Continued increase of extreme El Ninõ frequency long after 1.5 C warming stabilization. *Nature Climate Change*, 7(8):568–572.

Weatherall, P., Marks, K. M., Jakobsson, M., Schmitt, T., Tani, S., Arndt, J. E., Rovere, M., Chayes, D., Ferrini, V., & Wigley, R. (2015). A new digital bathymetric model of the world's oceans. *Earth and Space Science*, 2(8):331–345.

Webber, B. G. M., Heywood, K. J., Stevens, D. P., Dutrieux, P., Abrahamsen, E. P., Jenkins, A., Jacobs, S. S., Ha, H. K., Lee, S. H., & Kim, T. W. (2017). Mechanisms driving variability in the ocean forcing of Pine Island Glacier. *Nature Communications*, 8:14507.

Westerlund, S. & Öhman, P. (1991). Iron in the water column of the Weddell Sea. *Marine Chemistry*, 35(1-4):199–217.

Whitworth, T., Nowlin, W. D., Orsi, A. H., Locarnini, R. A., & Smith, S. G. (1994). Weddell Sea shelf water in the Bransfield Strait and Weddell-Scotia Confluence. *Deep-Sea Research Part I*, 41(4):629–641.

Whitworth, T., Orsi, A. H., Kim, S.-J., Nowlin, W. D., & Locarnini, R. A. (1998). Water masses and mixing near the Antarctic Slope Front. In: *Ocean, Ice, and Atmosphere: Interactions at the Antarctic Continental Margin, Antarctic Research Series*, S. S. Jacobs & R. F. Weiss, ed., volume 75 of *Antarctic Research Series*, pages 1–27. American Geophysical Union.

Williams, R. G., Wilson, C., & Hughes, C. W. (2007). Ocean and Atmosphere Storm Tracks: The Role of Eddy Vorticity Forcing. *Journal of Physical Oceanography*, 37(9):2267–2289.

Wingham, D. J., Francis, C. R., Baker, S., Bouzinac, C., Brockley, D., Cullen, R., de Chateau-Thierry, P., Laxon, S. W., Mallow, U., Mavrocordatos, C., Phalippou, L., Ratier, G., Rey, L., Rostan, F., Viau, P., & Wallis, D. W. (2006). CryoSat: A mission to determine the fluctuations in Earth's land and marine ice fields. *Advances in Space Research*, 37(4):841–871.

Wingham, D. J., Shepherd, A., Muir, A., & Marshall, G. J. (2018). Mass balance of the Antarctic Ice Sheet from 1992 to 2017. *Nature*, 558(7709):219–222.

Youngs, M. K., Thompson, A. F., Flexas, M. M., & Heywood, K. J. (2015). Weddell Sea Export Pathways from Surface Drifters. *Journal of Physical Oceanography*, 45(4):1068–1085.